A NEW ANALYTICAL FOURIER-TRANSFORMATION MODEL FOR X-RAY TIME LAGS IN AGN

by

David C. Baughman
A Dissertation
Submitted to the
Graduate Faculty
of
George Mason University
in Partial Fulfillment of
The Requirements for the Degree
of
Doctor of Philosophy
Physics

Committee:

Dr. Peter A. Becker, Committee Chair

Dr. Jeng-Eng Lin, Committee Member

Dr. Jessica Rosenberg, Committee Member

Dr. Paul So, Department Chairperson

Dr. Donna M. Fox, Associate Dean,
Office of Student Affairs & Special
Programs, College of Science

Dr. Fernando R. Miralles-Wilhelm, Dean,
College of Science

Date: 22 November 2021

Fall Semester 2021
George Mason University
Fairfax, VA

A New Analytical Fourier-Transformation Model for X-ray Time Lags in AGN

A dissertation submitted in partial fulfillment of the requirements for the degree of Doctor of Philosophy at George Mason University

By

David C. Baughman
Master of Science
Naval Postgraduate School, 2011
Bachelor of Science
United States Naval Academy, 2000

Director: Dr. Peter A. Becker, Professor
Department of Physics and Astronomy

Fall Semester 2021
George Mason University
Fairfax, VA

Dedication

To those who persevere despite any and all obstacles.

Acknowledgments

First and foremost, I would like to thank the following people: my parents, Stephen and Kathryn; my adviser, Dr. Peter Becker; and my few true friends. Your unwavering support throughout this long journey made this possible.

I would also like to thank my committee members, Dr. Jeng-Eng Lin and Dr. Jessica Rosenberg, for continuing to provide such positive support and patience with me through such a long journey.

Finally, I would like to thank the numerous other people at George Mason University and throughout my life who have also helped make this possible in many ways, some of which I am sure are unknown to me.

Table of Contents

List of Tables

List of Figures

Abstract

A NEW ANALYTICAL FOURIER-TRANSFORMATION MODEL FOR X-RAY TIME LAGS IN AGN

David C. Baughman, PhD

George Mason University, 2021

Dissertation Director: Dr. Peter A. Becker

The variability of the X-ray emission from black holes is often characterized in terms of the time lags observed between the soft and hard energy bands in the detector. The time lags are usually computed using the complex cross spectrum, which is based on the Fourier transform of the data in the two energy bands. For over a decade, it has been noted that some active galactic nuclei display soft Fourier X-ray time lags, in addition to the more ubiquitous hard lags. In the case of a soft lag, the X-rays in the low-energy channel are received after the corresponding signal is detected in the hard channel. The physical origin of the soft lags is a topic of ongoing research and discussion. In this dissertation I explore the possibility that the soft X-ray time lags result from the thermal and bulk Comptonization of photons injected into the relatively hot, quasi-spherical coronal region surrounding the cooler accretion disk near the central black hole. I develop a time-dependent analytical model for this process based on a Fourier-transformed radiation transport equation, and demonstrate that the model successfully reproduces both the hard and soft time lags observed in the narrow-line Seyfert 1 galaxy 1H0707-495, based on a unified physical mechanism operating in a single region. I then develop the quiescent solution and test whether a coronal photonic source is able to generate components of the observed X-ray spectrum.

Chapter 1: Introduction

The study of the physics of accreting black holes is an active area of research continually filled with new theories and observations. Much of the current research in this area is focused on matching observational data with software models in an effort to explain and understand the observations. My research presents a new theoretical model based off of explicit known physical processes. I compare these results to previous publication's observational data and in doing so, am able to more fully explore the fundamental aspects of the underlying physics.

This dissertation is organized as follows. In Chapter 1, I provide a history and brief overview of the current state of knowledge and research regarding black hole sources. In Chapter 2, I present the physical model and derivation of the time-dependent photon distribution function based on an analytical modeling of the corona around a black hole source with a non-relativistic, time-dependent transport model for photons scattered in an advecting, isothermal, inhomogeneous, spherically symmetric cloud that experiences an injection of monochromatic seed photons at a given radius at a specific point in time. In Chapter 3, I demonstrate the applicability of this model to a black hole source, namely the active galactic nucleus 1H0707-495. In Chapter 4, I derive the quiescent (time-independent or steady-state) photon distribution function and explore both monochromatic and bremsstrahlung injection sources. In Chapter 5, I review the applicability of the quiescent spectrum to the same source, 1H0707-495. In Chapter 6, I discuss and summarize my results of this dissertation and discuss future research opportunities.

1.1 A Brief History of Astrophysical Black Holes

1.1.1 Origins

Although the first "image" of an astrophysical black hole was just recently attained in the 21st century (see Figure 1.1), within the scientific community the concept of black holes extends over 200 years. As one of the most mystifying natural phenomenon that humans have ever discovered, black holes continue to capture both scientist's and laymen's interest alike. Ironically, the concept of black holes, something that appears to be undetectable, did not gain popularity until observational techniques arose that allowed the inferred detection of black holes based on theory. My research similarly requires the merger of theory and observation, and focuses on the still debated topic of understanding the physical processes that occur in the area surrounding black holes. I theorize, by comparison with observations, a black hole coronal model that successfully replicates observed X-ray phenomenon.

Figure 1.1: The first "image" of a black hole in the center of the galaxy M87 captured using radio waves and attained by the Event Horizon Telescope collaboration. Credit: Event Horizon Telescope Collaboration.

The first scientific idea of an astrophysical object being so massive that light could not escape it is ascribed to John Michell. In 1784 he published a letter for the Philosophical Transactions of the Royal Society of London where he postulated that, based on Newton's corpuscular theory of light, "dark stars" could exist with an equivalent density to our sun, but 500 times larger due to the inability of light to escape the star's own gravity (Michell 1784). In this paper Michell also made an initial attempt at describing potential observational techniques to discover black holes by noting that the existence of the star could be inferred by other luminous bodies revolving around it. Unfortunately, Michell's concepts were forgotten until the late 20th century.

The next foray into the theoretical concept of black holes, and still the foundation of current understanding, came in the early 20th century thanks to Albert Einstein's General Theory of Relativity. The formalism found in General Relativity (GR) allowed Karl Schwarzschild and Subrahmanyan Chandrasekhar to discover the foundation of modern day black holes as we know it. In 1915, prior to Einstein's final publication of his theory, Schwarzschild solved GR's field equations for the gravitational field of a non-rotating, spherically symmetric body with mass M (now known as the Schwarzschild metric). In this metric, at a specific radius now known as the Schwarzschild radius, r_s, the solution becomes singular (in addition to the other singularity solution where the radius is $r = 0$). Although, at the time the significance of r_s was debated since a coordinate change would cause the singularity to disappear, the mathematical foundation of the modern day black hole was discovered (albeit without the name). The influence of black holes in the scientific community was still very small until almost 20 years later when, using Einstein's theories, Chandrasekhar discovered a limit for a white dwarf star's mass beyond which it would gravitationally collapse, potentially into a black hole. This limit is now known as the Chandrasekhar limit and was the first such scientific work that implied the possibility of the formation of black holes beyond just a mathematical description. However, the community was still slow to garner interest in black holes until the 1960s when observational capabilities advanced enough to allow possible correlation with theoretical work.

The first observational evidence of black holes occurred in 1963 when the first quasar (and still the brightest), 3C273, was discovered using an optical spectrum from an earth-based telescope that demonstrated an unimaginably energetic source that was 10^{12} times more luminous than our sun, yet emerging from a region of space that was the size of our solar system. This was followed shortly after by the advent of space-based X-ray astronomy. It was at this time that giants of the theoretical physics community including John Wheeler, who coined the term black hole, in conjunction with advancements from the observational community, pioneered current modern day black hole physics research. Thanks to modern observational capabilities, it is now known that there are well over one-hundred thousand X-ray sources in the sky, and black hole research, in both the theory and observation domains, is one of the most active areas of physics today (see Figure 1.2).

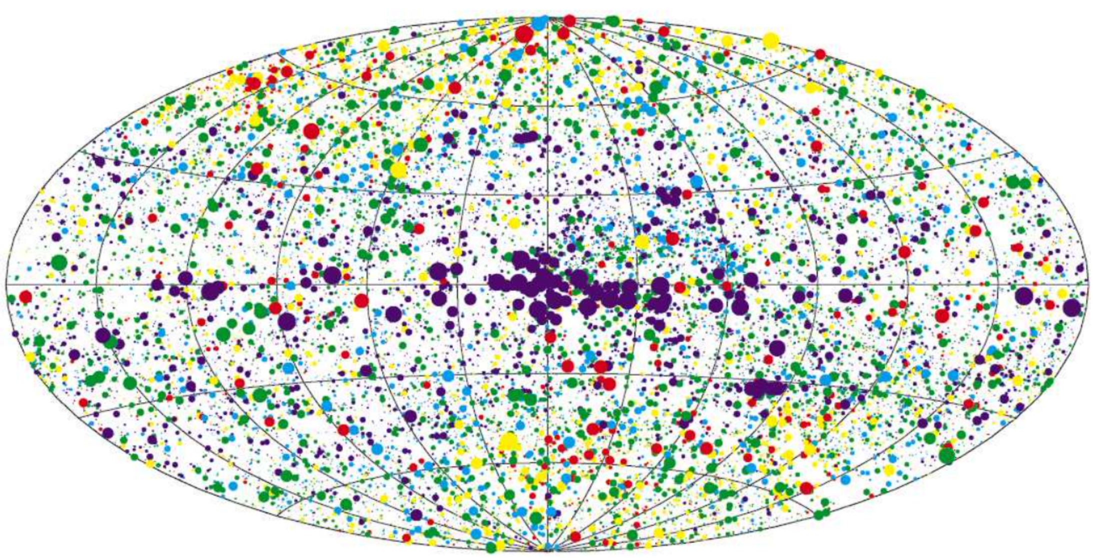

Figure 1.2: Aitoff projection of ROSAT All-Sky Survey observations in galactic coordinates. The size of the dot scales with the log of the count-rate and the colors represent different hardness ratios. Credit: Voges et al. (1999).

1.1.2 Models of Accreting Black Holes

Much of the current theoretical modeling of black holes today is focused not on the physical modeling of the black hole itself, but on the modeling of the accreting matter surrounding black holes. This modeling impacts our understanding of the physics of the black hole since the accretion disks are expected to be highly influenced by the black hole's strong gravity regime. The two black hole values that impact the surrounding accreting matter are its mass and its spin (a third value, its charge is expected to equal zero for accreting disks). The mass and spin dictate different aspects of accreting matter such as the minimum gravitationally stable radius, $r_{\rm ISCO}$, and the minimum angular momentum of stable orbiting material near the black hole.

The theoretical efforts to understand and model the accreting matter around black holes actually began before the first observational evidence for black holes. One of the most important initial efforts was Hermann Bondi's pioneering paper "On Spherically Symmetrical Accretion" (Bondi 1952). The model assumptions and results are now colloquially referred to as "Bondi accretion" and include a non-rotating, spherically symmetric, gas cloud accreting onto a star (defined as a point mass). The model only considers the forces of gravity and outward pressure, but the derived solutions on sonic radii and accretion rates are still used as valid comparative benchmarks for today's theoretical models.

The first true accreting models were developed in the 1970s, shortly after the first observational evidence of black holes. To date, there are still only a handful of general solutions that are typically invoked, with other solutions being variants of these. The primary individual stable solutions are: thin disk (Shakura-Sunyaev), slim disk, advection-dominated accretion flow (ADAF), and thick disk (ion torus or Polish doughnut). Equally important to these individual models are various composite models, which primarily take into account coronas surrounding the accretion disk. All of these models have been used to successfully recreate observations in both Galactic black hole (GBH) sources as well as active galactic nuclei (AGN). Note that the first three solutions (thin disk, slim disk, and ADAF) are all solved using the same system of equations that consider conservation of mass, radial and angular momentum, and energy, but with different assumptions and initial values. I will briefly review all of these models below, but for a more thorough review, publications such as "Foundations of Black Hole Accretion Disk Theory" by Abramowicz & Fragile (2013) are recommended.

The physics of all of these models incorporates a complicated, semi-analytic combination of non-linear processes that includes gravity, hydrodynamics, viscosity, radiation, and magnetic fields. The general physics of the accretion process is as follows. The angular momentum of infalling matter is removed by undefined viscous forces and transported outwards which in turn allows the matter to spiral inward toward the black hole. The matter's gravitational energy is converted to heat, a fraction of which is converted into radiation. Some of the radiation escapes and cools the accretion disk. It is assumed that, in general, these processes occur in different dynamical, thermal, and viscous time-scales with their relative relationship given by $t_{\mathrm{dyn}} < t_{\mathrm{th}} < t_{\mathrm{vis}}$. Dynamical processes account for pressure, gravity, and centrifugal forces; thermal processes account for dissipative heating and cooling processes such as advection; and viscous processes account for torque changes caused by undefined dissipative stresses, identified as potentially being due to magnetic rotational instability (Balbus 2005).

Thin Disks

The thin disk model (Shakura & Sunyaev 1973) was the first accretion disk model developed and is still one of the most commonly utilized models today. This system assumes that undefined viscous stresses convert gravitational energy into heat, which is then radiated. The system of equations are then solved neglecting advection and winds. The identifying aspects of this solution are as follows. First, for a stable solution, the mass accretion rate, $\dot{M}$, is constant with radius and is much less than the Eddington limit, $\dot{M}_{\mathrm{E}}$ (e.g., Done et al. 2007). This value is given as $\dot{m} = \dot{M}/\dot{M}_{\mathrm{E}} \leq 0.2$ for thin disks. Note that the Eddington limit defines the limit where radiation pressure on electrons is balanced by gravitational attraction on protons. The Eddington limit for the luminosity, L_{E}, is given by,

$$L_{\mathrm{E}} = \dot{M}_{\mathrm{E}}\, c^2 = \frac{4\pi G M m_p c}{\sigma_{\mathrm{T}}}\ . \tag{1.1}$$

Second, the accreting matter forms a thin disk such that its height is smaller than its radius. Third, the disk temperature is relatively cool and most likely on the order of tens to hundreds of electron volts. And fourth, the disk is optically thick, producing a quasi-blackbody spectrum that has been fitted to numerous observed spectra as shown in Figure 1.3 (see Sections 1.2 and 1.3 for discussions on radiation and states).

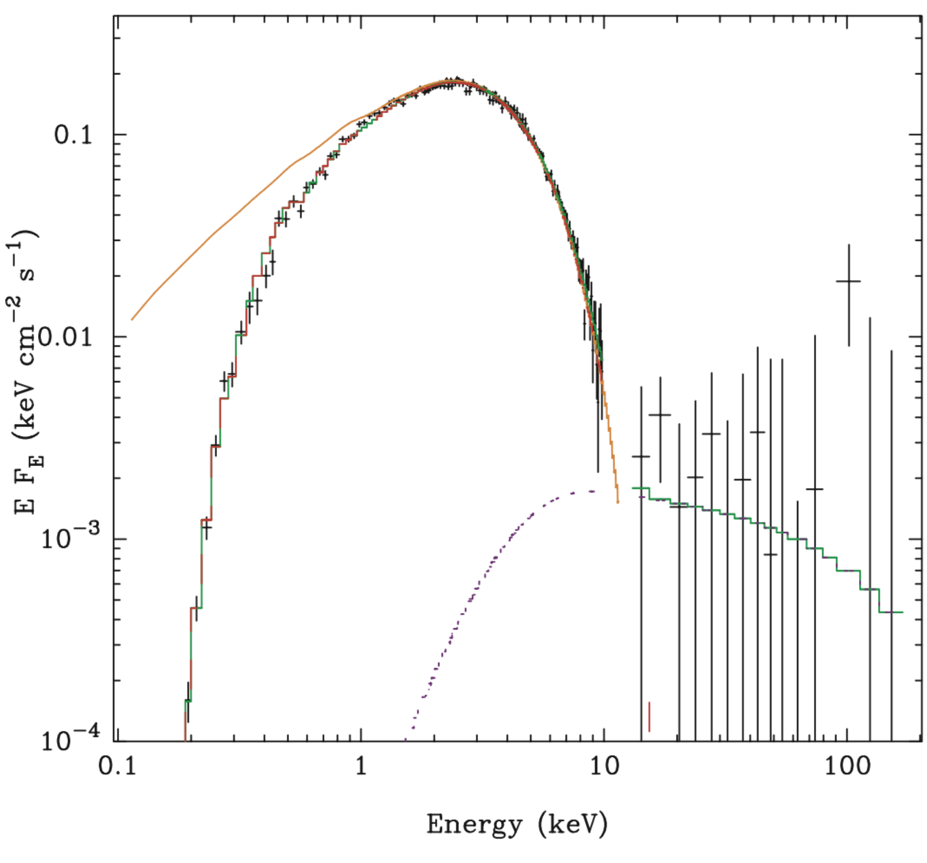

Figure 1.3: Thin disk modeled spectrum (BHSPEC) shown in red as compared to the unfolded BeppoSAX spectrum of LMC X-3. The purple is a non-thermal component (COMPTT) and the green is the composite spectrum. See Sections 1.2 and 1.3 for discussions on radiation and states. Credit: Davis et al. (2006).

Slim Disks

Following the solution of the thin disk model, in the late 1970s and 1980s the slim disk model was developed due to the fact that when accounting for the same optically thick accreting matter, as the accretion rate and luminosity increases, the assumption of cooling solely by radiation is no longer valid (e.g., Abramowicz et al. 1988). In many aspects, the slim disk solution is much more physical than the thin disk solution. The increasing accretion rate creates a larger radial velocity, a temperature that increases and becomes nearly independent of accretion rate, and a "thicker" disk, which requires advection in the physical solutions (note that some authors identify this as a second category of ADAFs below). In the slim disk solutions, geometrically, the accretion disk's height can rise to nearly the same value as its radius, which is why the solution set is identified as a "slim disk" (e.g., Narayan et al. 1998).

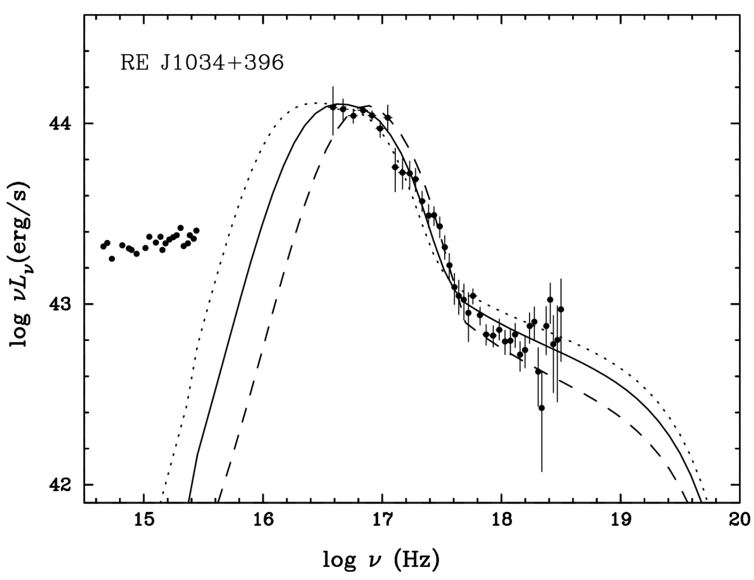

Figure 1.4: Slim disk modeled X-ray spectrum of RE J1034+396 with Compontization in a hot corona included. The dashed, solid and dotted lines represent ESD models with $\dot{m} = 5, 10,$ and 20 respectively. See Sections 1.2 and 1.3 for discussions on radiation and states. Credit: Wang & Netzer (2003).

A benefit of the slim disk model is that it encompasses a wide range of accretion rates for $\dot{m} > 0.2$. For accretion rates much larger than the Eddington limit, the model becomes known as an extreme slim disk (ESD). Spectrum predictions for this model include a "flattening" of the soft blackbody X-ray energies, a total luminosity that is saturated and so no longer proportional to the accretion rate, and a high energy cutoff that is independent of the accretion rate. An example of a slim disk model fitted AGN spectrum is shown in Figure 1.4.

An Unstable Solution: SLE

Shortly after the implementation of the thin disk model, it was noted that the model was unable to explain the non-thermal component of X-ray sources in the hard state (see Sections 1.2 and 1.3 for further discussions on radiation and states), and specifically Cygnus X-1 in the hard state. Building off of the work of Thorne & Price (1975); Shapiro, Lightman, and Eardley (Shapiro et al. 1975), hereafter SLE, discovered a much hotter solution that successfully reproduced the observed non-thermal behavior of Cygnus X-1. This solution, known as the "SLE model", requires a two-temperature system where the ions are much hotter than the electrons, is optically thin, has a high accretion rate and luminosity, and is geometrically big, similar to the slim disk described above. Unfortunately, shortly after it was discovered it was proven to be thermally unstable and so it is no longer normally invoked as a potential physical model. However, the SLE solution was important in that it was one of the first efforts to model non-thermal spectra and it also demonstrated the ability to utilize a two-temperature model to achieve a much hotter, almost virial, solution. This in turn helped create a foundation for later models that, as will be shown next, provide a stable solution.

ADAF

Originally developed in the late 1970s and early 1980s, and fully adopted in the 1990s, a separate advection dominated solution from the slim disk model was developed for disks with a low optical depth. In this model, similar to the thin disk the gas is accreting at a low rate ($\dot{M} < \dot{M}_{\rm E}$) and so is unable to cool by radiation within the accretion time-scale. Therefore, due to the combination of low optical depth and low accretion rate, the viscous energy is advected inward instead of being radiated outward. These solutions are known as advection-dominated accretion flows or ADAF solutions. For a thorough review of ADAFs, see Narayan et al. (1998).

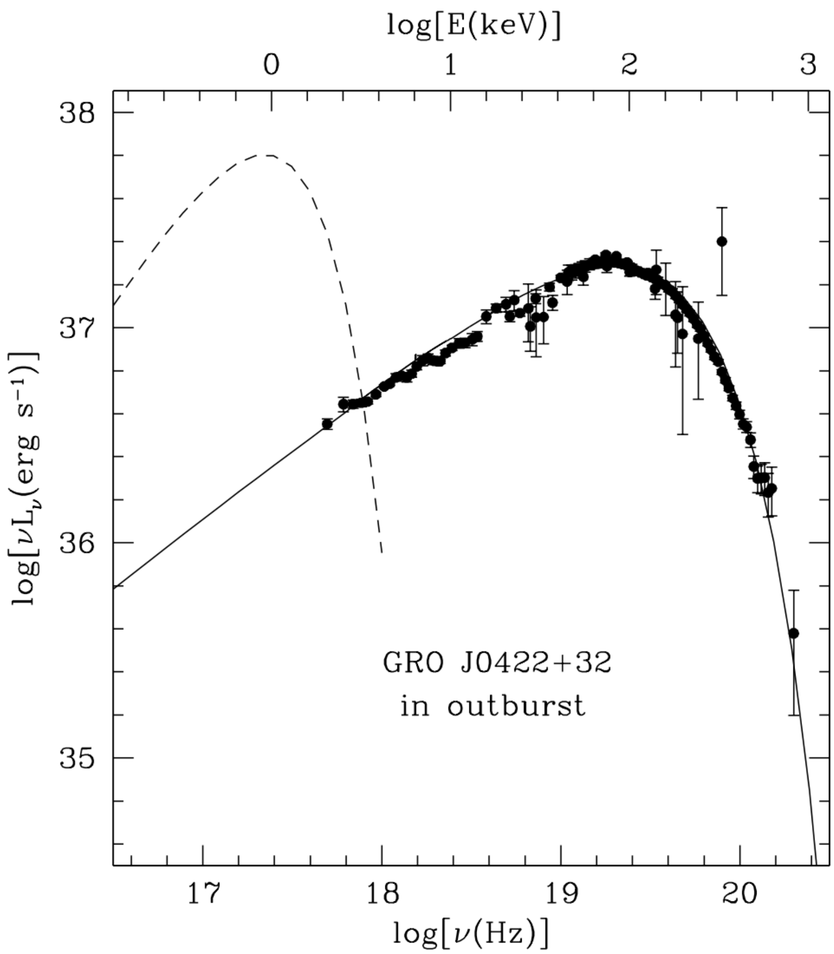

Figure 1.5: ADAF model of J0442+32 (solid line) in the low/hard state, compared with the observational data (dots and error bars). The dashed line shows a thin disk model at the same accretion rate, $\dot{m} = 0.1$. See Sections 1.2 and 1.3 for discussions on radiation and states. Credit: Narayan et al. (1998).

Similar to the SLE model, the ADAF model is very hot, nearly virial, and requires a two-temperature (ions and electrons) solution in order to be stable. Geometrically, ADAFs are quasi-spherical and become quite large, similar to the unstable SLE model and the simplistic Bondi spherical solutions. It should also be noted that ADAFs are expected to usually have large, sub-Keplerian, rotational velocities and radial velocities that are a sizable percentage of free fall. Observationally, the ADAF solutions produce a low luminosity, non-thermal spectra, often appearing as a Comptonizing power-law, that has been successfully applied to black hole sources in the low/hard state as shown in Figure 1.5 (see Sections 1.2 and 1.3 for discussions on radiation and states).

Thick Disks

The fourth model category utilized to describe accreting matter around black holes is called thick disks. I combine two separate solutions known as ion torus and Polish doughnut into this category which both have similar geometries that resemble large spheres with empty funnels along the rotation axis, but it must be emphasized that they each have very different underlying physical models. The first thick disk solution, ion tori (e.g., Rees 1984), is created due to ion pressure in the inner regions of the accretion flow and has a hot, two-temperature ion-electron profile similar to ADAFs. Also similar to ADAFs, they have low accretion rates and produce little radiation with the exception of radio jets which are powered by the Blandford-Znajek mechanism. As can be seen graphically in Figure 1.6, there is overlap between the ion torus and ADAF models. The second thick disk solution is known as the Polish doughnut (e.g., Abramowicz 2005). This solution was originally discovered in the 1980s by Paczynski & Wiita (1980) while researching high accretion rates near the black hole. Similar to the SLE solutions, these systems have high luminosities in excess of the Eddington limit and are optically thick. These systems also have lower angular momentum and radial velocities. Both of these thick disk models have faced instability challenges in the past; however, it has been shown that the Roche lobe overflow that occurs stabilizes the instabilities and so these solutions are in fact feasible (e.g., Straub et al. 2012). That being said, there have not been many successful published spectra fittings utilizing one of these two thick disk models.

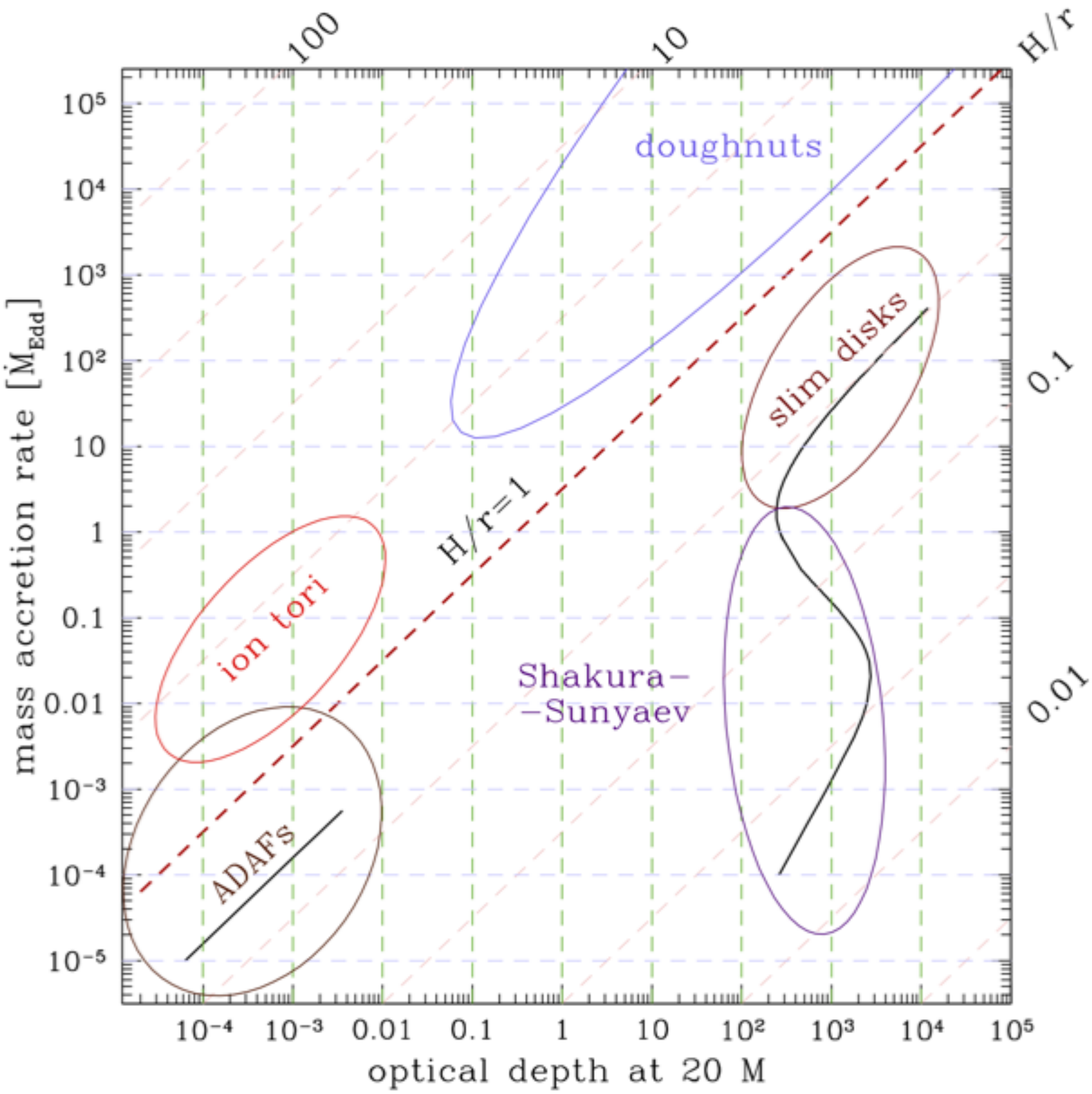

Figure 1.6: Major accretion models shown for different accretion rates, optical depths, and height to radius geometries. Here $M = R_g$. Credit: Abramowicz et al. (2010).

Coronal Composite Models

Since the first comparisons of observation and theory, it has almost always been noted that the accretion models above are not able to individually completely describe the observed spectra of black hole sources. This is also clearly evident in the spectral fitting figures shown above. Because of this, in addition to the accretion models described above, composite models, many of which describe the addition of a corona region around the black hole, have been developed. For instance, Esin et al. (1997) and Narayan & McClintock (2008) explored various thin disk composite geometries as shown in Figure 1.7 to account for different observations of black holes.

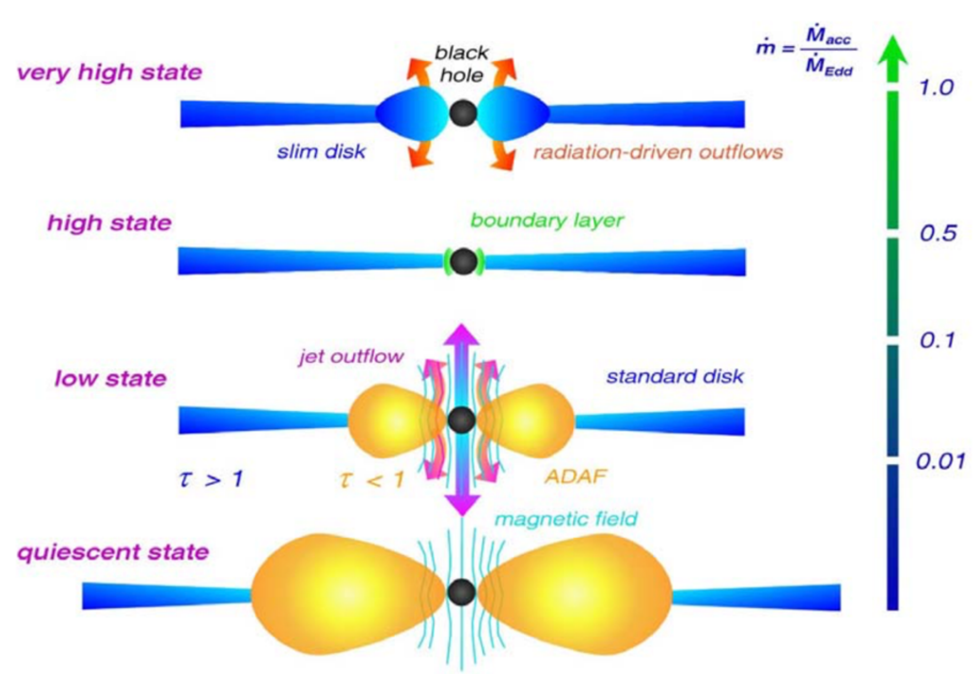

Figure 1.7: Theoretical composite configurations of the accretion flow as the accretion rate changes.

As another example, Narayan et al. (1998), proposed a transitional composite model. This model incorporates a transition radius, r_t, where inside r_t, the model is described by an ADAF solution while outside r_t, the model is described by a thin disk surrounded by a hot corona (which itself is modeled as an ADAF). As a third example, Poutanen (1998) identified the following different coronal composite geometries: sandwich, where a hot corona covers a cold disk; magnetic flares, where a patchy corona exists above a cold disk; cloudlets, where the cold disk dissipates into optically thick clouds inside the corona; and sombrero, where the cold disk only penetrates partially into the coronal region (Poutanen states this is similar to an ADAF). He reviewed different black holes along with their common states (see Section 1.3) and explored the spectral fits of these various composite geometries where the corona was defined as an "electron (-positron) plasma cloud in energy and pair equilibria without assuming any specific geometry of the accretion flow". Other authors predict composite models where a slim disk exists toward the inner radius of high accreting black holes in conjunction with a thin disk that is located in a slowly accreting outer radius region. These are only a few examples of authors using composite models, but they demonstrate how commonplace and important this aspect is to modeling the accretion flow around black holes.

1.2 X-ray Radiative Processes in Black Hole Sources

All black hole sources are modeled (and observed) to radiate in energies across the electromagnetic spectrum. Physics predicts that some of the highest energies in the universe are released due to the highly energetic processes and events occurring around accreting black holes. These high energy processes in turn produce X-rays that are generated by both thermal radiation processes consisting of blackbody, thermal bremsstrahlung, and thermal Comptonization as well as non-thermal radiation process to include inverse Compton scattering and synchrotron processes.

1.2.1 Thermal Radiation

Thermal radiation is an important component of black hole radiation and is seen in almost all spectral data observed of these sources. It is generated by blackbody radiation for optically thick sources and thermal bremsstrahlung radiation for optically thin ionized plasmas. An additional production process known as thermal Comptonization consists of the repetitive scattering of seed photons off of energetic electrons in a region where the electrons are assumed to have a Maxwellian velocity distribution.

Blackbody

A Blackbody is theoretically defined as an object that absorbs and emits all radiation frequencies. In the X-ray spectrum, this radiation is generated by electrons transitioning between their inner atomic shells. For an optically thick gas in isothermal equilibrium, blackbody radiation has a specific spectrum that depends only on the body's temperature. In the case of black holes, the radiating body is assumed to be the surrounding area of the black hole which may consist of an accretion disk or some other optically thick body of gas or material. Blackbody radiation spectra are defined by Planck's law, which is given by,

$$I(\nu, T) = \frac{2h\nu^3}{c^2} \frac{1}{e^{\frac{h\nu}{k_B T}} - 1} \ , \tag{1.2}$$

where h is Planck's constant, ν is the photon frequency, c is the speed of light, k_B is Boltzmann's constant, T is the temperature of the body, and I is the spectral radiance. Examples of these spectra can be seen in panel a) of Figure 1.8. As noted in panel a) of Figure 1.8, the peak of the spectrum has a clear correlation to a specific temperature given by Wien's displacement law,

$$\nu_{\text{peak}} \approx \frac{2.821}{h} k_B T \ . \tag{1.3}$$

Hence, by observing black hole sources that contain a blackbody radiation component, one can begin to understand the temperature of the areas surrounding the black hole and therefore what physical processes could be occuring. This spectral component nearly always comprises some portion of observed black hole spectra. Panel b) of Figure 1.8 shows an example of a black hole source that is radiating thermal X-ray radiation as evidenced by the good fit between the theory line in red and the observed data in black.

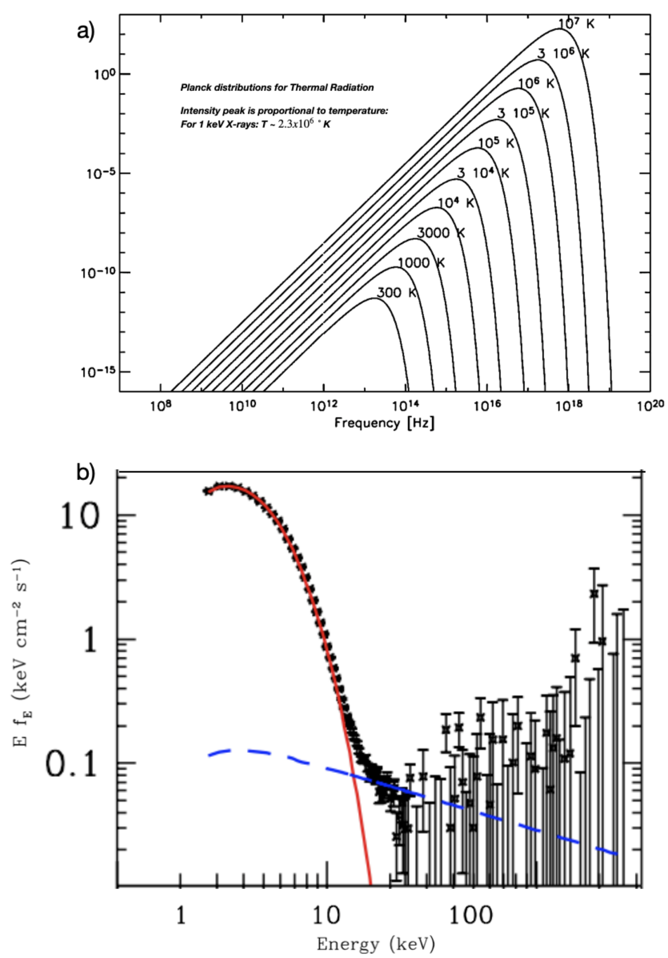

Figure 1.8: a) Theoretical plots of thermal blackbody radiation at different temperatures. b) Sample spectra of black hole binary GRO J1655-40 in the thermal state. The black plot is data and the red line is the decomposed thermal component. Credit: Remillard & McClintock (2006).

Thermal bremsstrahlung

Thermal bremsstrahlung or "braking" radiation arises due to energetic free electrons interacting with ions in an isothermal gas which is assumed to have a Maxwellian velocity distribution. As the electrons are accelerated, or more accurately decelerated, by the ions and lose kinetic energy, they emit high energy radiation in the form of X-rays. Due to the wide range of accelerating events that are possible, the range of energies produced is wide ranging and so a large number of electrons will produce a broadband continuous spectrum. For black holes this radiation is assumed to occur in an optically thin ionized gas with at least a local thermal equilibrium. The generated electron energies are dictated by the temperature of the gas and therefore the spectra follow well defined functions, similar to Planck spectra, as shown in Figure 1.9. The energy emission in CGS units for thermal bremsstrahlung in an optically thin, ionized plasma of hydrogen is shown to be, from Rybicki & Lightman (1979),

$$\varepsilon_{\nu}^{ff}(\nu, T_e) = 6.8 \times 10^{-38} Z^2 n_e^2 T_e^{-1/2} e^{-(h\nu)/(k_B T_e)} \bar{g}_{ff} \tag{1.4}$$

where Z is the charge number, n_e is the electron density, T_e is the electron temperature, and $\bar{g}_{ff}$ is a velocity-averaged Gaunt factor, or quantum correction, which in the regime of $hf = k_B T_e$, is approximately unity.

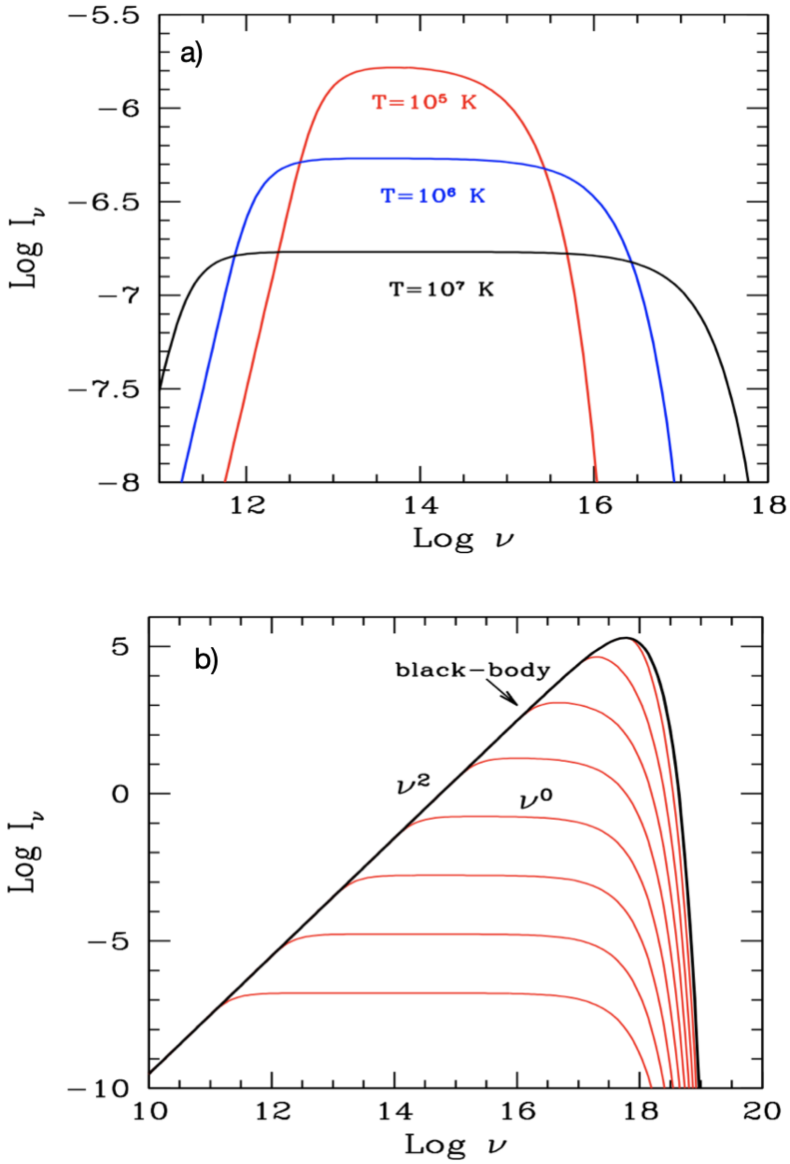

Figure 1.9: a) Theoretical plots of thermal bremsstrahlung radiation at different temperatures. b) Theoretical plots of increasing density of thermal bremsstrahlung radiation as it approaches optically thick blackbody radiation. Credit: Ghisellini (2012).

Thermal Comptonization

Whereas blackbody and thermal bremsstrahlung radiative processes generate photons, thermal Comptonization consists of multiple inverse Compton scatterings or scatterings of photons off of a Maxwellian distribution of electrons in thermal equilibrium where the photons gain energy. For black holes, this radiative process is important at high accretion rates (Maraschi & Molendi 1990). Generally speaking, this process and its relative impact to the black hole's spectrum can be inferred by the Compton y parameter which for non-relativistic electrons is given by (Rybicki & Lightman 1979)

$$y = \frac{4k_BT_e}{m_ec^2}\mathrm{Max}(\tau_{es}, \tau_{es}^2) \ , \tag{1.5}$$

where τ_{es} is the electron scattering optical depth and m_e is the mass of an electron. The thermal Comptonization radiative process becomes significant when $y \gtrsim 1$. The spectrum for non-relativistic thermal Comptonization requires solving the Kompaneets equation, which describes the evolution of the photon distribution function, given by (Rybicki & Lightman 1979)

$$\frac{\partial n}{\partial t_c} = \left(\frac{k_BT_e}{m_ec^2}\right)\frac{1}{x^2}\frac{\partial}{\partial x}[x^4(n' + n + n^2)] \ , \tag{1.6}$$

where n is the photon phase space density, $x \equiv h\nu/kT$, and t_c is the time measured in units of mean time between scatterings. If one defines the Thomson scattering optical depth as $\tau_{\mathrm{T}} = \sigma_{\mathrm{T}}n_eR$ where R is the size of the source, and following Ghisellini (2012), rewrites the Compton y parameter as

$$y = \mathrm{Max}(\tau_{\mathrm{T}}, \tau_{\mathrm{T}}^2) \times [16\Theta^2 + 4\Theta - x] \ , \tag{1.7}$$

where $\Theta = k_BT_e/m_ec^2$, then the following thermal Comptonization radiation spectrum regimes exist. It should be noted that for all regimes, as the photon energy approaches the electron temperature the spectrum falls to zero since further scatterings leave the photon frequency unchanged. For $\tau_{\mathrm{T}} < 1$, the flux is a power law given by

$$F_{\nu} \propto x^{-\Gamma} \ , \tag{1.8}$$

where Γ is the photon index. For the case where $\tau_{\mathrm{T}} \gtrsim 1$ the result is still a power law, but the photon index is found to be:

$$\Gamma \approx -3/2 + \sqrt{(9/4 + 4/y)} \ . \tag{1.9}$$

When $\tau_{\mathrm{T}} > 1$ a Wien shape is produced and for $\tau_{\mathrm{T}} \gg 1$ a more complicated spectrum with a "Wien bump" is produced as shown in Figure 1.10. The Wien spectrum has radiation intensity given by

$$I(x) \propto x^{3} e^{-x/\Theta} \ . \tag{1.10}$$

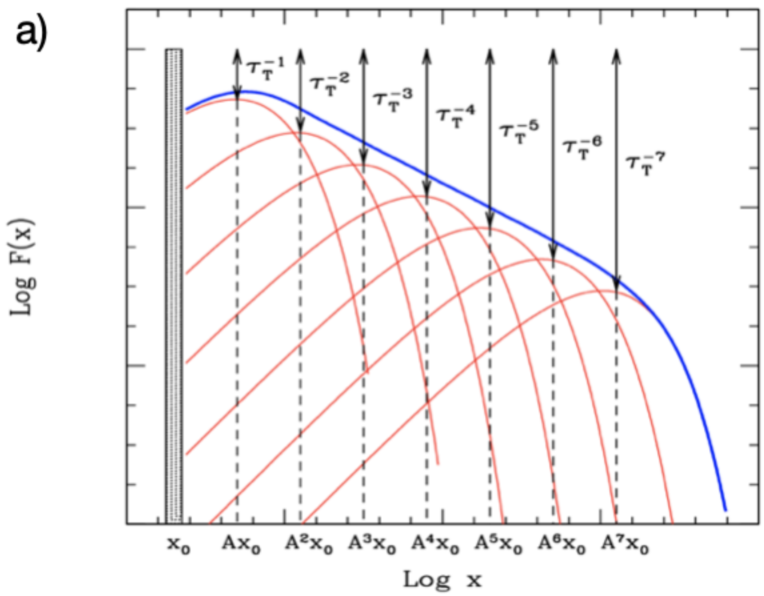

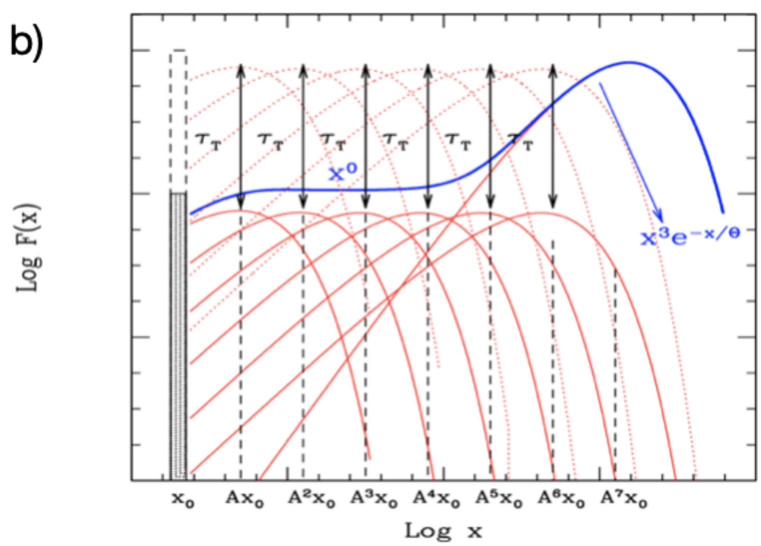

Figure 1.10: a) Theoretical plot of thermal Comptonization for $\tau_T < 1$. Multiple Compton scatterings where a fraction of the photons of the previous scattering order undergoes another scattering, and amplifying the frequency by the gain factor A. b) Theoretical plot of thermal Comptonization for $\tau_T > 1$ and $y >> 1$. The Wien bump can be seen on the right side of the plot. Credit: Ghisellini (2012).

1.2.2 Non-Thermal Radiation: Inverse Compton and Synchrotron

A large portion of the X-ray radiation received by black hole sources is not clearly fitted by the thermal radiative processes outlined above and instead is characterized by non-thermal processes. The two most common processes noted are inverse Compton scattering and synchrotron radiation. Similar to thermal Comptonization, inverse Compton scattering entails a transfer of energy from the electron to the photon as they interact with each other. Unlike thermal Comptonization, non-thermal inverse Compton scattering assumes a different energy distribution of the electrons such as a power-law energy distribution. Synchrotron radiation occurs when relativistic particles are moving in a magnetic field. The gyration of the particles around the magnetic field lines generates high energy radiation that is related to the frequency of gyration. Figure 1.11 shows how synchrotron radiation is composed of the superposition of many individual spectra.

In both cases, relativistic factors are considered and the radiation spectrum produced is of the form of a power law and is also related to the electron distribution power law. Given the Lorentz factor, $\gamma = E_e/m_e c^2$, where E_e is the total electron energy, for an electron distribution given by

$$n_e(\gamma) \propto \gamma^{-p} \ , \tag{1.11}$$

the flux in both types of non-thermal radiation is found to be

$$F \propto E^{-\alpha}; \quad \text{where } \alpha = (p-1)/2. \tag{1.12}$$

For both inverse Compton scattering and synchrotron radiation, the frequency of the scattered photons is found to be approximately $\nu \approx \gamma^2 \nu_0$.

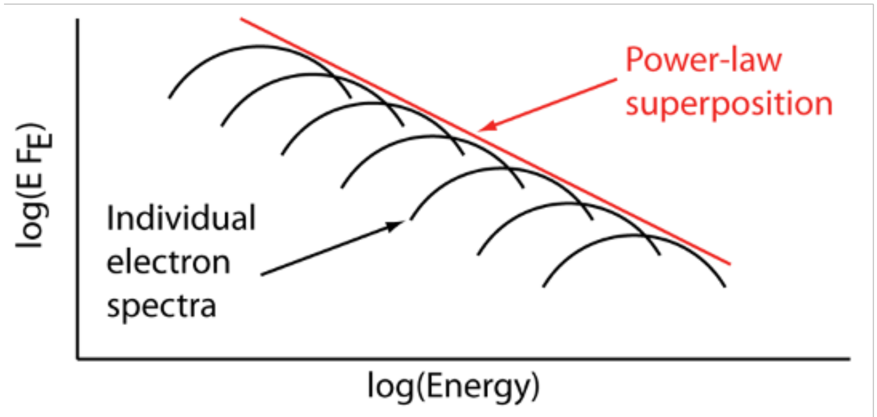

Figure 1.11: Plot of individual synchrotron electron spectra and the superposition of many spectra. Credit: Shu (2009).

1.3 Investigative Techniques of Black Holes Sources

In general, black hole candidates are identified in one of two ways: observations of gravitational anomalies and observations of highly energetic electromagnetic waves. Both of these methods require highly advanced technology as gravitational anomalies are difficult to detect and the earth's atmosphere blocks out almost all high energy electromagnetic waves. Hence, it wasn't until the advent of space-based X-ray astronomy in the 1960s that the observational field of black hole astrophysics truly became possible. Since the 1960s dozens of space-based X-ray telescopes have been launched. In addition to being utilized to detect black holes, these spacecraft have been key in the study of understanding the physical processes surrounding black holes. The method of X-ray investigations is broadly broken into the following three groups: light curves, spectral data, and timing data.

1.3.1 Light curves

The first observations in the 1960s of X-ray data used light curves, which are still useful in the study of X-ray sources. Light curves provide brightness information for a set of wavelengths (energies) over a period of time for the object observed (see Figure 1.12). This then provides an understanding of general phenomenological processes at work. For instance, for stellar sized black hole binaries' X-ray light curves, similarities arise that allow comparisons to be made of different sources that demonstrate a "classic" light curve characterized by an outburst profile with a fast rise and an exponential decay over a time period on the order of weeks (McClintock & Remillard 2006).

Light curves are often broken into different energy groupings to provide more detailed information. By observing similarities and differences in these smaller groupings, further discrimination and understanding can be achieved. For instance, with X-ray emission emanating from black holes, historically there are two broad groupings where certain X-rays below an energy threshold are noted as soft X-rays (<2 keV) and those larger than a threshold (> 10 keV) are known as hard X-rays. Note that the definition of soft and hard is relative and varies depending on the research being conducted. Having knowledge of the total brightness as well as the relative flux factor of the X-ray bands allows for further classifications. The first example of this occurred with the first observed black hole source, Cygnus X-1, where it was noted that when it was brighter, the soft X-ray flux (usually an emission value around 1 keV) was observed to be higher than the hard flux. This common observation was defined as a "state" of the black hole and was termed the "high/soft state" (Remillard & McClintock 2006). A variety of different combinations of states, whose classification depends on more detailed spectral data and will be discussed later, have been observed both in stellar sized black holes as well as AGN.

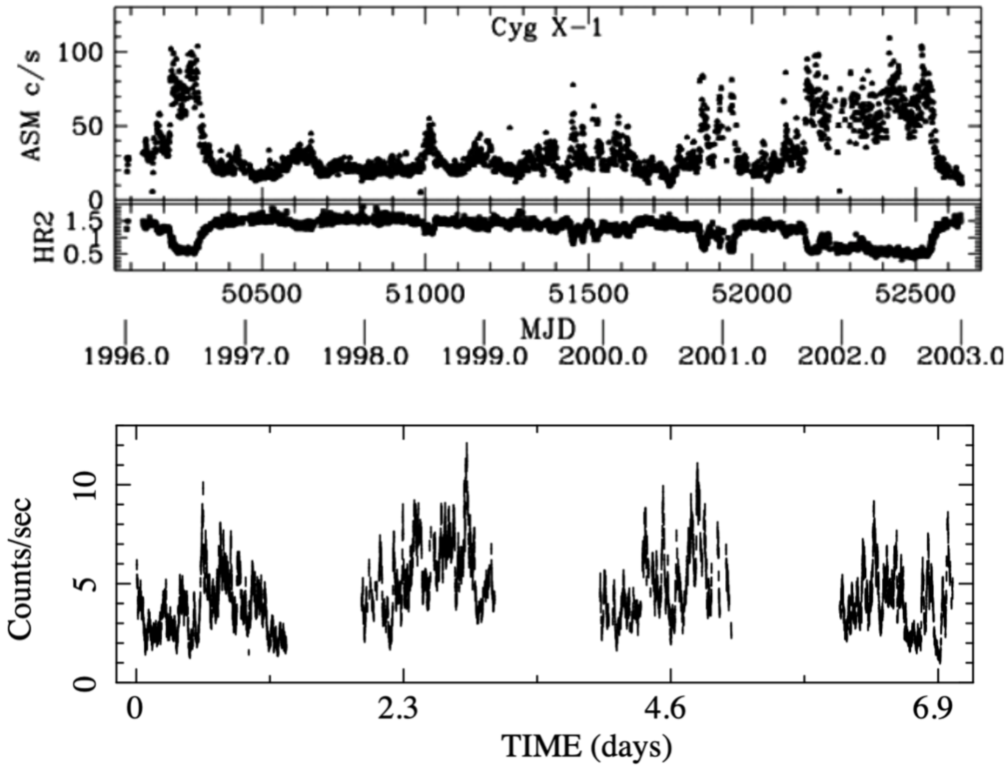

Figure 1.12: Two example light curves. The top is of a seven-year Rossi X-ray Timing Explorer (RXTE) All-Sky Monitor light curve from 1996 to 2003 of the stellar mass black hole binary Cygnus X-1. Credit: McClintock and Remillard (2006). The bottom is of a one week XMM-Newton observation in 2008 of the active galactic nuclei 1H0707-495. Credit: Fabian et al. (2009).

Light curve investigations are not limited to X-ray data alone. For instance, with AGN, optical light curves can also be utilized. In AGN, the optical continuum, which is primarily produced by the accreting matter itself (Smith et al. 2018), consists of light curves that have relatively fast time-scales (on the order of hours to days to months). Hence, exploration of the light curve variability in this data allows one to research the area near the black hole since the entire accretion disk extends to scales on the order of hundreds or thousands of astronomical units (Pica & Smith 1983).

1.3.2 Spectral Data

The second key method of X-ray investigations involves detailed exploration of the spectral data. This data is explored using both broad-band spectra as well as high-resolution, narrow-band, atomic line spectra. The broadband spectra has provided the ability to validate theoretical physical models that attempt to explain the observations. Additionally, the high-resolution spectra has helped to investigate properties such as black hole mass and spin by reviewing relative strengths and widths of the lines as well as relativistic broadening and gravitational redshifts (Fabian et al. 1989).

Broad-band spectra investigations have yielded various commonplace spectral continuum. For instance, a thermal continuum indicative of blackbody radiation is routinely seen. Another common continuum displays an exponential or very steep decrease toward high X-ray energies and yet another continuum type exhibits a broad power-law behavior. In addition to attempting to produce these results with physical models, these broad-band spectral investigations have led to standardized classifications of the aforementioned "states" of black hole sources. The definition and classification of the states has matured over the last 50 years and in general both spectral and timing data (ironically the original concept of luminosity has since been abandoned) are used to determine the state.

McClintock & Remillard (2006) define four canonical states for black hole binaries that have been widely adopted (see Figure 1.13). To first order, these states can be spectrally understood as comprised of the following: a) Quiescent: BHBs spend most their time in this state and it is characterized by exceptionally low luminosity and a hard, non-thermal spectrum ($\Gamma = 1.5 - 2.1$); b) Hard: sometimes called the "low/hard state", with increasing luminosity BHBs usually transition from quiescent to this state which is characterized by a power law ($\Gamma \sim 1.7$) with either a non-existent or at least much cooler thermal component as well as persistent radio jets; c) Thermal: sometimes referred to as the "high/soft state", this is the original state identified for Cyg X-1 and is dominated by a thermal component with a $\sim$ 1 keV thermal emission from a multi-temperature accretion disk as predicted by the Shakura-Sunyaev (thin) disk model (Shakura & Sunyaev 1973); d) Steep Power

Law: sometimes referred to as the "very high state", this state contains a disk component and a steep ($\Gamma \sim 2.5$) power law component as well as intermittent jets. There also exist intermediate states that do not fit into the four states above. For a detailed review of information on the composition of these states see McClintock & Remillard (2006).

Note that although these spectral states are identified for BHBs, they are expected to similarly be seen in AGN. However, since time-scales scale inversely with black hole mass, the transition time between states is expected to exceed 10^5 years and so population studies of AGN are needed for further evaluations. Type 1 AGN appear to correspond to a spectral state similar to the BHB soft state and low-ionization nuclear emission-line region (LINER) galaxies appear to correspond to the BHB hard state (Sobolewska et al. 2011).

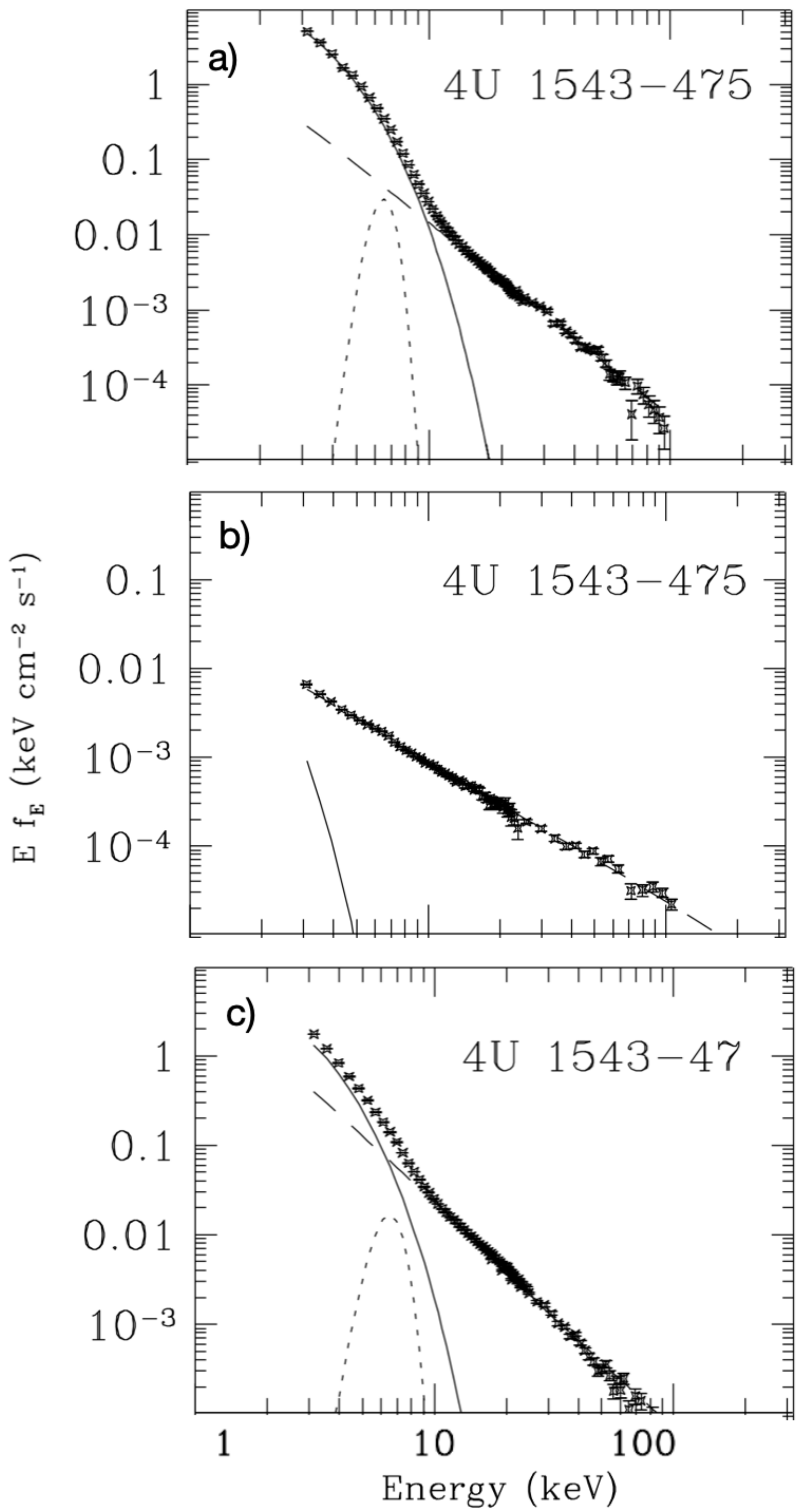

Figure 1.13: Three spectral states of BHB 4U 1543-475. The components are decomposed as: thermal (solid line), power-law (dashed), Fe line (dotted). a) Thermal state b) Hard state c) Steep Power Law state. Credit: McClintock and Remillard (2006).

1.3.3 Timing Data

Timing investigations, also referred to as X-ray variability, have been noted as the most important resource for examining the area near a black hole due to the rapid variations that are often observed (Remillard & McClintock 2006). The variability is most commonly investigated in the frequency domain by investigating the power spectral density (PSD or PDS), quasi-periodic oscillations (QPOs), and Fourier time lags. This research has helped to further the study of black hole sources as well as demonstrate that the accretion process is the same for all black holes regardless of mass when taking into accretion rates and time-scales. Confirmation of the universality of physical processes provides confidence in our understanding of the underlying physics and also the ability to gain insight into all black holes by only investigating one mass scale.

Power Spectral Density

The power spectral density (PSD or PDS) explores the variability of the power, given by the square of the amplitude of typical sinusoidal variations of frequency ν, versus a plot of the frequencies in the signal (see Figure 1.14). The amplitude of typical sinusoidal variations is found by the Fourier transform of the observed count-rate spectrum, denoted by $\tilde{\mathscr{F}}_\epsilon(\epsilon,\omega)$, and is given by

$$\tilde{\mathscr{F}}_\epsilon(\epsilon,\omega) = \int_{-\infty}^{+\infty} \mathscr{F}_\epsilon(\epsilon,t)\, e^{i\omega t}\, dt \ , \tag{1.13}$$

where $\mathscr{F}_\epsilon(\epsilon,t)$ denotes the count-rate flux at the detector. The PSD then is explicitly given by,

$$\mathrm{PSD} = |\tilde{\mathscr{F}}_\epsilon(\epsilon,\omega)|^2 \ . \tag{1.14}$$

In particular, the PSD is useful for both its shape and integrated amplitude. For example, although the first observations of AGN X-rays showed scale-invariant behavior on all time-scales up to days, subsequent observations showed characteristic time-scales derived from PSDs (McHardy et al. 2006). To first order, the results of black hole PSDs can be broken into categories correlating with the hard and soft states. In the hard state, a majority of the X-ray flux is highly variable and so although the PSD is complex, it is usually easy to quantify. Additionally, in the hard state the PSD is often described by a sum of two or more Lorentzian distributions which is given by $P_\nu \propto \lambda/[(\nu - \nu_0)^2 + (\lambda/2)^2]$ with FWHM equal to λ or sometimes it can be described by a doubly-broken power-law given by $P_\nu \propto \nu^{-\alpha}$. Conversely, in the soft state a majority of the X-ray flux arises from a non-variable quiescent component which makes it more difficult to quantify the PSDs. In general, the integrated amplitude of the PSD is much smaller in the soft state versus the hard state. When the soft state PSD for galactic black holes and AGN is quantifiable, it is often described by an $\alpha \approx 1$ power-law with a break to a steeper $\alpha \gtrsim 2$ power-law. An important result of PSD studies to date is that a characteristic time-scale associated with the break (as well as the line-widths) have been shown to scale as black hole mass divided by accretion rate across all black hole mass regimes thereby helping to confirm the universality of physical processes (Arevalo et al. 2008).

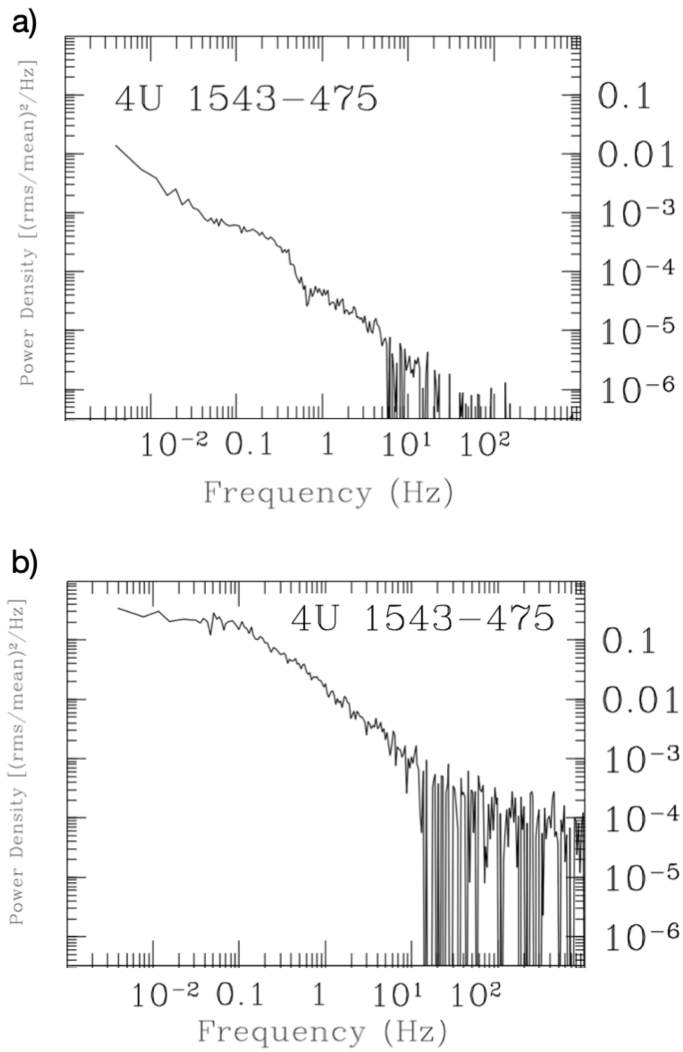

Figure 1.14: Two example PSD plots of BHB 4U 1543-475. The notably larger amplitude is noted in panel b). a) Thermal state b) Hard state. Credit: McClintock and Remillard (2006).

Quasi-Periodic Oscillations

Quasi-periodic oscillations (QPOs) are transient features found within the PSDs of BHB in non-thermal states and especially the SPL state (see Figure 1.15). For BHBs, they range in frequency from 0.01 to 450 Hz and are usually modeled with a single Lorentzian profile with quality factor, $Q \equiv \nu_0/\lambda > 2$. They are further identified by utilizing a coherence parameter given by $Q = \nu/FWHM \gtrsim 2$ (van der Klis 2006). BHB QPOs have been broadly broken into high frequency (HFQPOs) with QPOs $\nu > 100$ Hz and low frequency (LFQPOs) with QPOs 0.1 Hz $< \nu <$ 100 Hz. LFQPOs are often seen in the SPL state and sometimes in the hard state with their amplitude generally peaking at photon energies greater than 10 keV and sometimes above 60 keV. The origins of LFQPOs is an ongoing area of research that utilizes correlation studies with spectral parameters as well as phase lags, but their consistent and episodic nature implies that they must occur as a holistic outcome of the physics surrounding black holes. HFQPOs are relatively elusive and only detected at high count rate within the SPL state. Due to their high frequency they potentially imply the ability to explore the inner regions around BHBs and so have garnered interest. This potential for new knowledge has made their discovery highly sought after and although their detections are quite difficult with AGN, research efforts have persisted. Relatively recently they were reported as discovered in AGN with an ~ 1 hour periodicity (Alston et al. 2015).

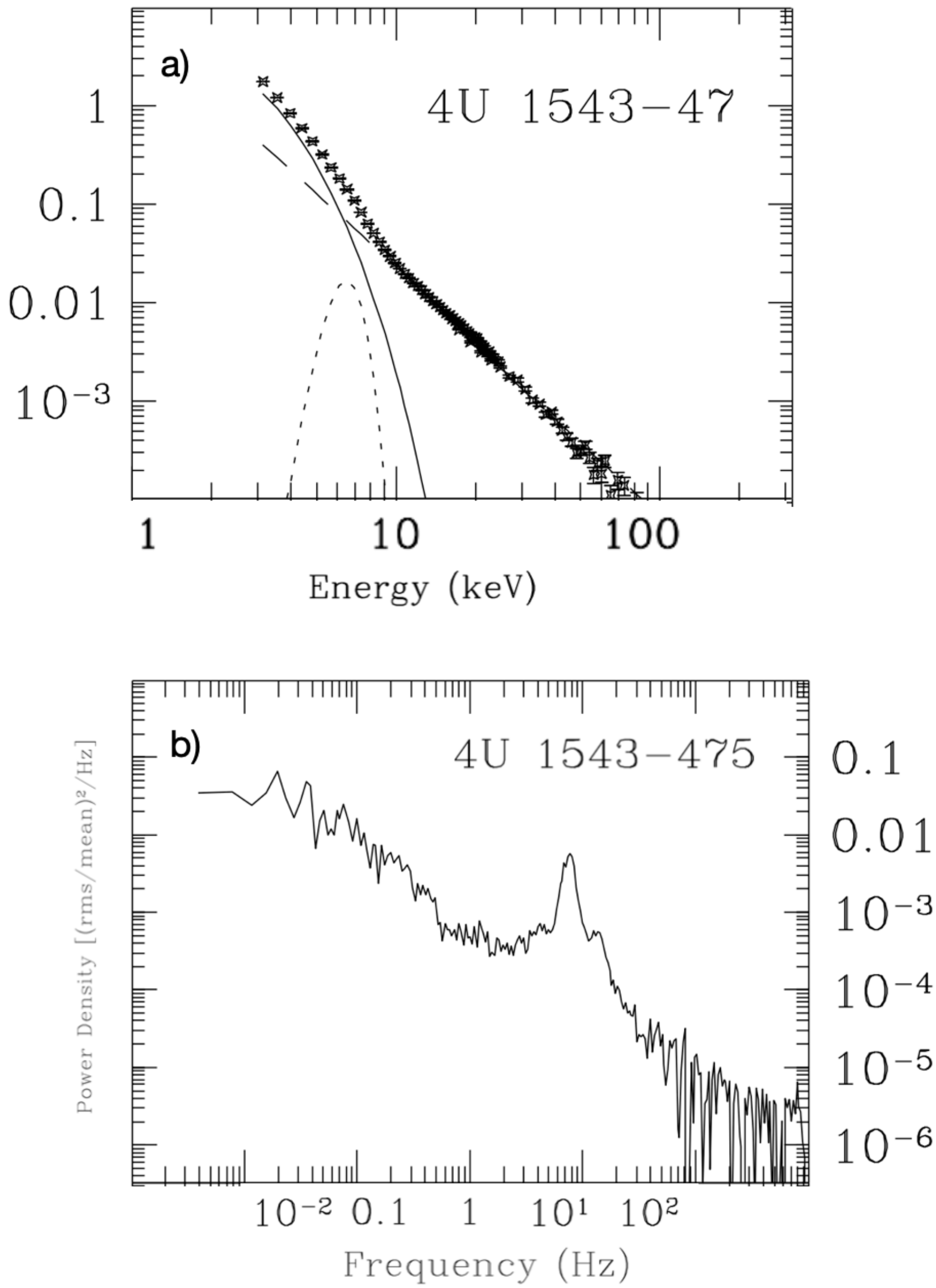

Figure 1.15: An example of a QPO at approximately 10 Hz for BHB 4U 1543-475 which can be described by a Lorentzian is noted in panel b). a) SPL State Spectra Plot b) PSD with QPO observed at 10 Hz Plot. Credit: McClintock and Remillard (2006).

Fourier Time Lags

Oftentimes, spectral analysis requires utilizing individual, short time-scale data and high-energy astrophysical phenomena is no exception. As an example, for black hole sources, the typical minimum variability is equal to the light crossing time for one gravitational radius given by $R_g = GM/c^2$. The timescale is given by,

$$\Delta t = \frac{GM}{c^3} = 4.94 \times 10^{-6}\text{sec}\left(\frac{M}{M_\odot}\right) \ , \tag{1.15}$$

where $M_\odot$ is in units of solar masses. If I use the observed value for the mass of AGN 1H0707-495 as an example, $M = 2 \times 10^6 M_\odot$, then the time scale is approximately 10 seconds. At these timescales with these distances to the sources in question, these data sets have poor photon statistics. The signal-to-noise ratio is nominally too low to investigate variability with short snapshots of the spectrum and analysis becomes very difficult in the time domain. An example of a highly variable, multi-channel, X-ray spectrum from a Seyfert galaxy is depicted in Figure 1.16.

In order to fully explore the underlying physics, innovative approaches are needed such as Fourier analysis. Fourier analysis makes use of all of the data in the observation window and is therefore an ideal tool to analyze short time-scale, high-variability data. As a subset of Fourier analysis, time lags are a key tool and are highly useful when investigating sources with broadband energies being generated that also are incurring variability. The study of time lags has proven invaluable to advance our understanding of accretion processes as it enables the ability to correlate and validate proposed physical models by being able to compare theory with observational data.

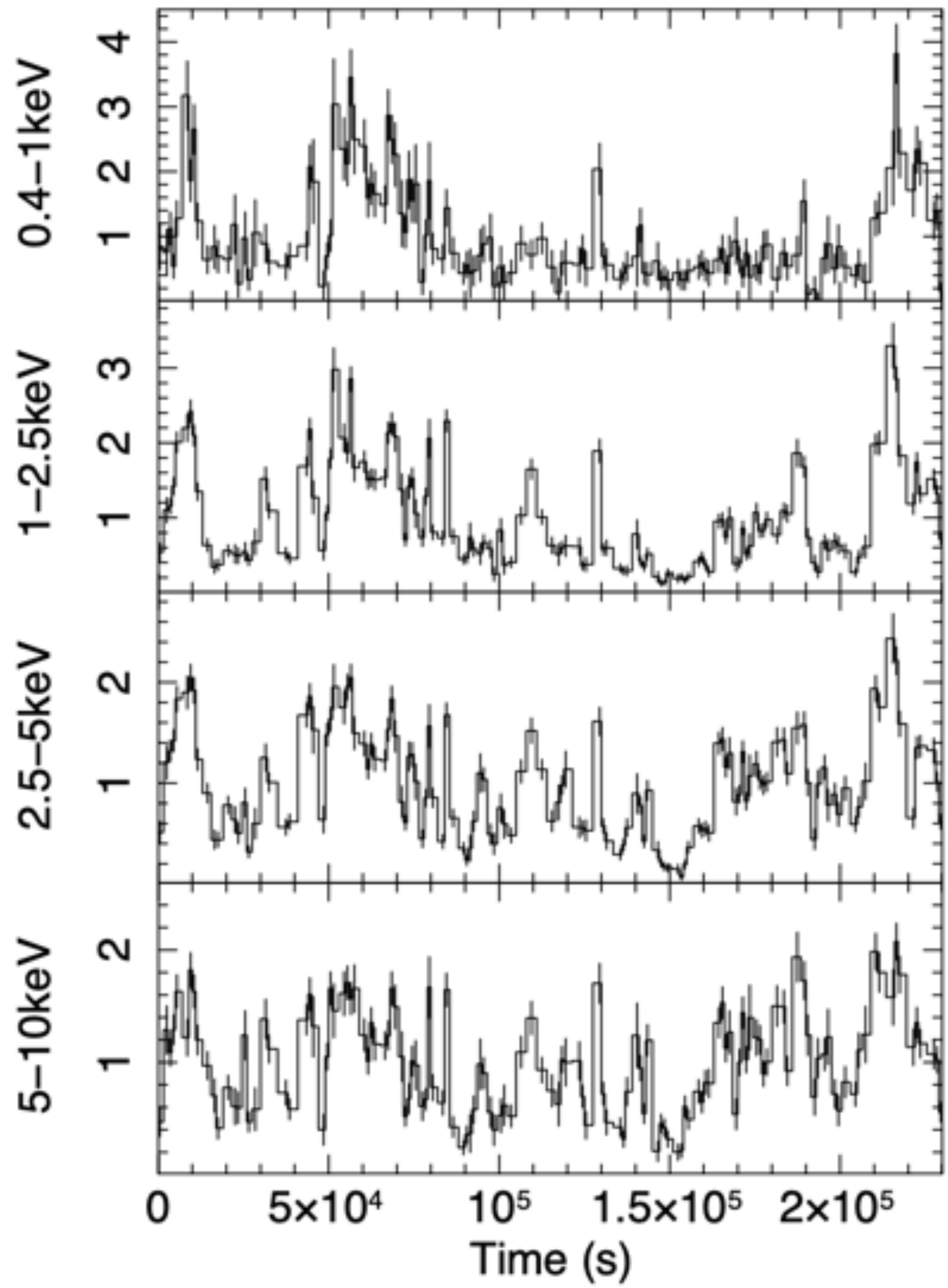

Figure 1.16: X-ray light curve variability shown in four energy bands normalized to the mean count rate with time resolution at 1 ks. Credit: Iwasawa et al. (2010).

Fourier time lags occur when one grouping of X-rays (for instance hard X-rays) associated with a given Fourier component arrives before or after another grouping of X-rays (for instance soft X-rays) that are associated with the same Fourier component (see Figure 1.17). Hard Fourier time lags are those in which the hard X-rays lag behind the soft X-rays and soft Fourier time lags occur in the opposite sense. Hard Fourier time lags have been seen in the X-ray emission from many black hole sources for more than three decades as discussed by van der Klis et al. (1987), Böttcher & Liang (1999), Crary et al. (1998), Arevalo & Uttley (2006), and Kroon & Becker (2016). However, soft lags are a relatively new field of investigation.

Whereas most black hole observations are first discovered in GBH sized sources, soft lags were first discovered in the AGN 1H0707-495 and hereafter referred to as H707 (Fabian et al. 2009). Since this discovery, broader studies have revealed that soft lags are quite common and are found in all AGN mass scales ranging from low-mass (Mallick et al. 2021) to high-mass (De Marco et al. 2013). Some of the main results from De Marco et al. (2013) are depicted in Figure 1.18. Soft Fourier time lags have also been discovered in stellar-mass sources (De Marco et al. 2015), however there is a great deal of difficulty in using these sources to study the underlying physical processes due to the extremely small time scales. Conversely, the time scales of the observed AGN soft lags is on the order of $\sim 10 - 100$ seconds (Fabian et al. 2009; Emmanoulopoulos et al. 2011; De Marco et al. 2013; Cackett et al. 2013), making them extremely useful probes in understanding the inner regions of the associated accretion processes that include temperature, density, and accretion configuration. The De Marco et al. (2013) and Mallick et al. (2021) studies have also confirmed a proportional scaling relationship between AGN black hole mass and Fourier lag magnitude, reconfirming other X-ray variability investigations, which show that the same underlying physics are occurring in the accretion process of all black hole sources.

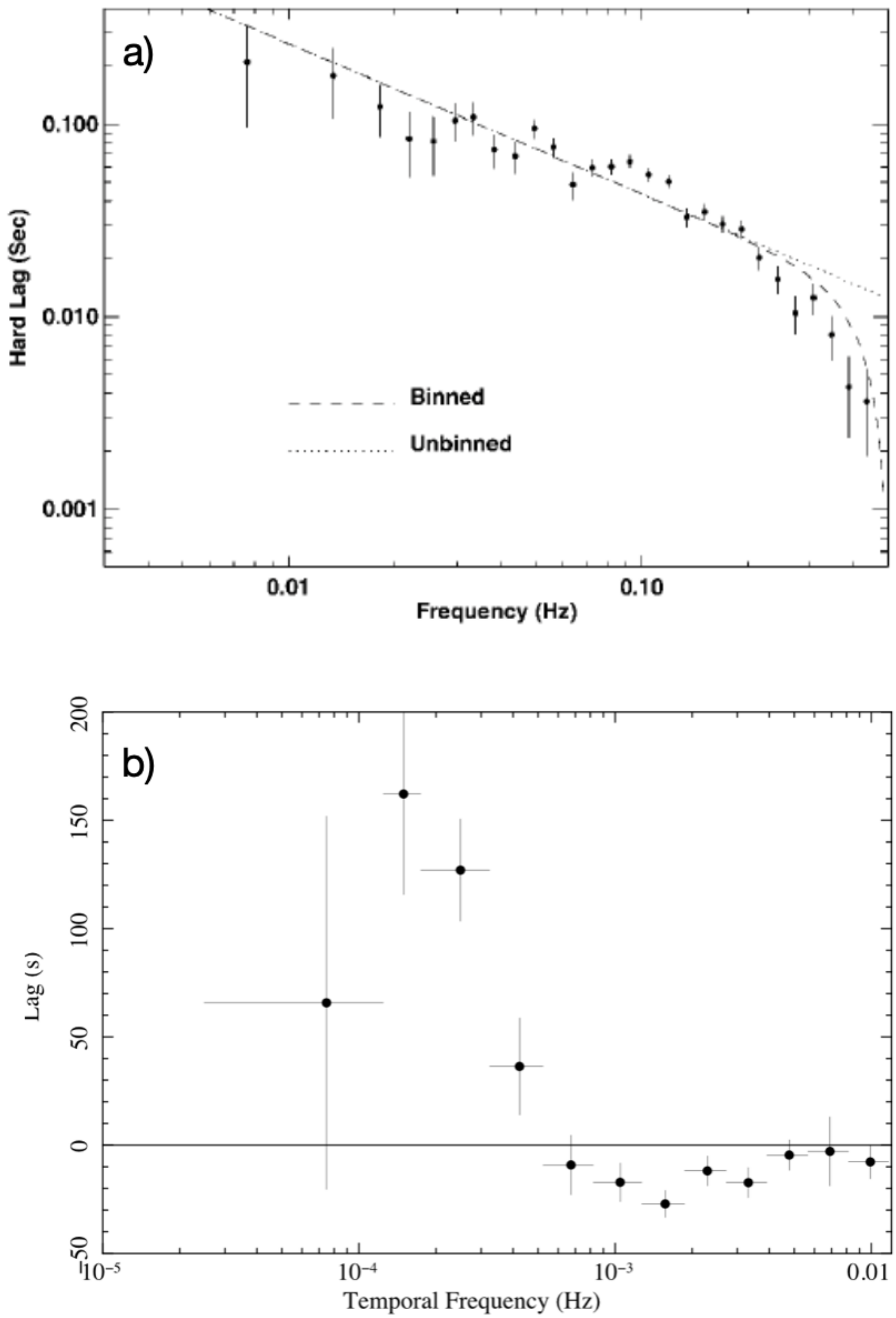

Figure 1.17: Hard and soft time lags as a function of frequency for a) Cygnus X-1 and b) H707. Hard lags are positive and soft lags are negative. a) The dashed line is the time lag obtained from a fit to the lag model. Credit: Crary et al. (1998). b) Frequency-dependent time lags between the 0.3-1 keV and 1-4 keV bands in H707. Credit: Fabian et al. (2009).

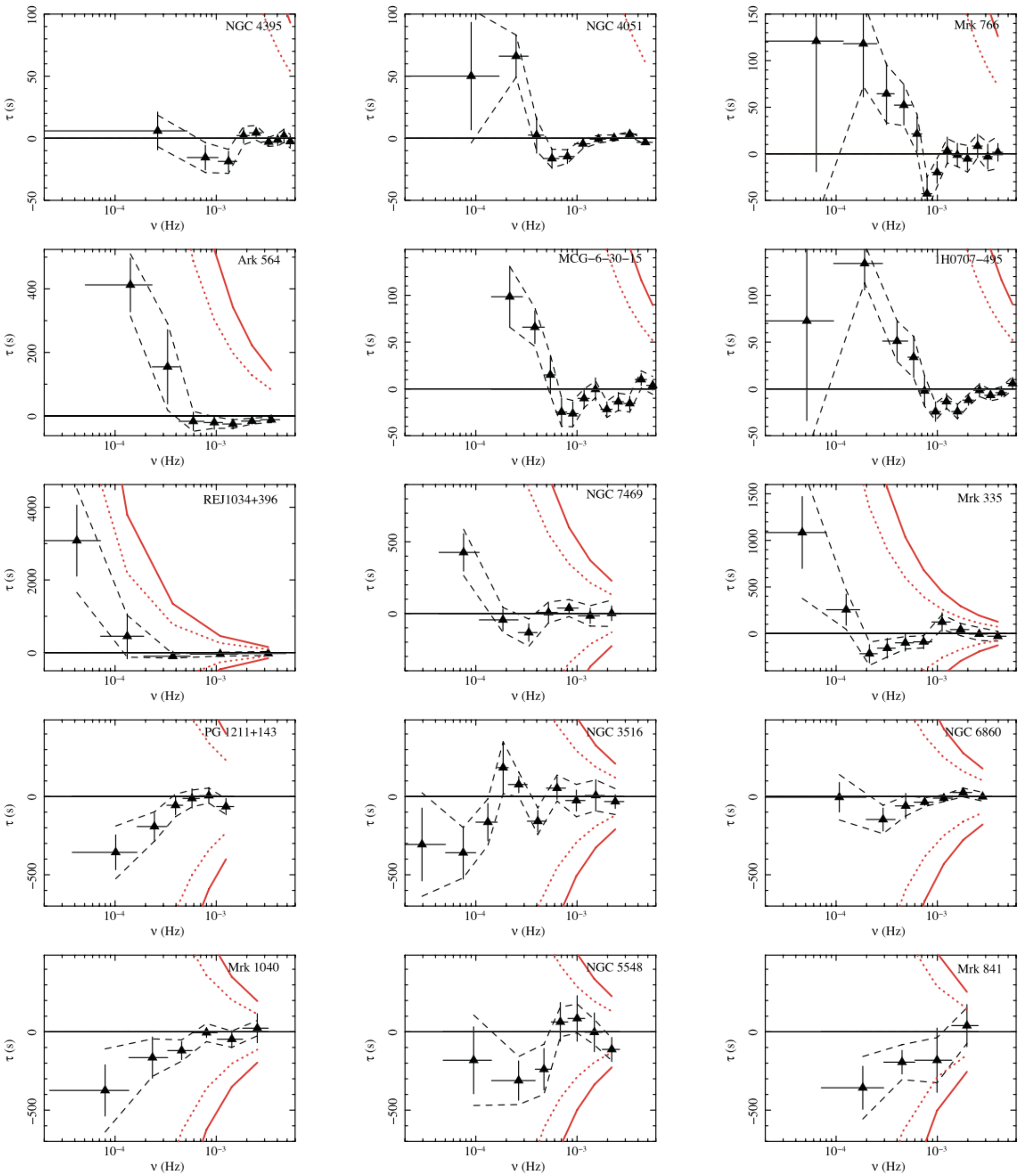

Figure 1.18: AGN with soft lags detected at $> 2\sigma$ confidence level. Credit: De Marco et al. (2013).

1.4 An Introduction to X-ray Fourier Time Lags

1.4.1 Computation of X-ray Fourier Time Lags

The idea of computing the time lags between two photon energy bands using Fourier analysis was first suggested by van der Klis (1987), with subsequent development and application by Nowak et al. (1999). The calculation of the time lags is based on the development of the complex cross spectrum, C, defined by

$$C(\omega) = S^*(\omega)H(\omega) \ , \tag{1.16}$$

where

$$\omega = 2\pi\nu_F \ , \tag{1.17}$$

denotes the circular Fourier frequency, ν_F is the Fourier frequency in Hz, and $S(\omega)$ and $H(\omega)$ represent the Fourier transforms of the soft and hard photon energy light curves, corresponding to photon energies ϵ_s and ϵ_h, respectively. The asterisk in Equation (1.16) represents the complex conjugate.

The Fourier transforms $S(\omega)$ and $H(\omega)$ appearing in Equation (1.16) are computed using the integrals

$$\begin{aligned} S(\omega) &= \int_{-\infty}^{+\infty} s(t)\, e^{i\omega t} dt \ , \\ H(\omega) &= \int_{-\infty}^{+\infty} h(t)\, e^{i\omega t} dt \ , \end{aligned} \tag{1.18}$$

where the soft and hard photon energy light curves are denoted by $s(t)$ and $h(t)$, respectively. The two light curves are related to the time-dependent X-ray photon count-rate spectrum observed at the detector, $\mathscr{F}_\epsilon(\epsilon, t)$, via

$$
\begin{aligned}
s(t) &= \mathscr{F}_\epsilon(\epsilon_s, t) \ , \\
h(t) &= \mathscr{F}_\epsilon(\epsilon_h, t) \ .
\end{aligned}
\tag{1.19}
$$

The corresponding Fourier time lag, δt, is then evaluated using the relation

$$
\delta t(\omega) = \frac{\phi(\omega)}{\omega} \ , \tag{1.20}
$$

where the phase lag, ϕ, is given by

$$
\phi(\omega) = \mathrm{Arg}[\mathrm{S}^*(\omega)\mathrm{H}(\omega)] \ . \tag{1.21}
$$

According to the sign convention adopted here, a positive time lag, $\delta t > 0$, corresponds to a hard lag, in which the hard channel signal lags the soft channel signal for a given Fourier frequency (or inverse variability period).

Simple Example of Time Lags

As an instructional example of this, consider two light curves, hard=$h(t)$ and soft=$s(t)$, where the Fourier transform of the light curves are given by:

$$
H(\omega) = \int_{-\infty}^{+\infty} h(t)e^{i\omega t}dt = H(\omega)e^{i\varphi_{\mathrm{h}}} \tag{1.22}
$$

$$
S(\omega) = \int_{-\infty}^{+\infty} s(t)e^{i\omega t}dt = S(\omega)e^{i\varphi_{\mathrm{s}}} \tag{1.23}
$$

The Fourier transformed light curves have respective phases given by φ_{h} and φ_{s} where $\varphi = \omega t$ is the respective frequency component's phase angle as expected. If the light curves have a perfect time lag between them, where t is the time for the hard curve, and $t - \Delta t$ is the time for the soft curve, then the hard time lag is given by $h(t) = s(t - \Delta t)$. Making the substitution, $t' = t - \Delta t$, the hard curve Fourier transform can now also be written as:

$$H(\omega) = \int_{-\infty}^{+\infty} h(t)e^{i\omega t}dt = \int_{-\infty}^{+\infty} s(t')e^{i\omega(t'+\Delta t)}dt' = S(\omega)e^{i\omega\Delta t} \tag{1.24}$$

Using Equation (1.13), $C(\omega)$ is now given by:

$$C(\omega) = S^*(\omega)H(\omega) = S^*(\omega)S(\omega)e^{i\omega\Delta t} = |S(\omega)|^2 e^{i\omega\Delta t} \tag{1.25}$$

It can now clearly be seen that the phase lag is given by both $\phi(\omega) = \varphi_{\mathrm{h}} - \varphi_{\mathrm{s}}$ (the argument of the cross-spectrum) and also $\omega\Delta t$. Hence, $\phi(\omega) = \omega\Delta t$. Dividing this phase lag by ω as shown in Equation (1.17), it can plainly be seen that the lag solution is now a time lag given in seconds and $\tau = \Delta t$ as expected.

It can also be easily deduced that the existence of time lags necessarily implies time variability in the source, since steady-state light curves would generate no phase lag, and therefore no time lag. Hence the detection of time lags from a given source necessarily implies the existence of variability in the X-ray signal from the source. This implies that the emission from a given source can be viewed as a superposition of continual steady-state emission, combined with episodic bursts or flashes, which produce time-dependent phenomenon such as the time lags.

1.4.2 Physical Models for X-ray Fourier Time Lags

Different physical models to explain X-ray Fourier hard time lags exist and at least three models have been presented in peer reviewed literature. One model utilizes accretion rate fluctuations over a wide range of radii and time-scales propagating inwards to modulate a radially extended X-ray emission region with an energy-dependent profile (Lyubarskii 1997; Kotov et al. 2001; Arevalo et al. 2006). A second concept incorporates waves that propagate cylindrically and symmetrically in a transition disk with a uniform propagation speed (Misra 2000). A third theory of the hard lags involves the recent, successful reconsideration of thermal Comptonization of a source radiation. The successful modeling was achieved within the constraints of the broadband bremsstrahlung injection of photons into a spherical, homogenous, static coronal cloud (Kroon & Becker 2014).

A key benefit to the Comptonization theory for hard lags, and any physical theory for that matter, is that it does not require the kludging of different concepts to generate the observations. Qualitatively, the cause of hard lags by Comptonization is a straightforward matter of noting that the photons that have a higher energy will take longer to reach that energy in the cloud. Assuming that the source energy of the photons, $h\nu$, are much less than the electron temperature of the cloud, T_e, the process of Comptonization in the gas means that the energy of the photons will continue to increase over time as they continue to interact with the higher energy electrons in the cloud. The typical fractional change in photon energy per scattering is $\sim 4kT_e/m_ec^2$. For a given variability in Fourier frequency, the lower energy photons will escape the cloud first and the higher energy will escape later since they have taken longer to reach higher energies. Additionally, the lower Fourier frequency variability will have an associated longer time lag scale between two energy levels than will the higher Fourier frequency. Similar to hard lags, no universally agreed upon theory exists for the recently discovered soft time lags. Furthermore, the previous models are complicated and utilize a patchwork of kludged mechanisms with different thermal zones and geometrical constraints to explain the soft lags.

The first explanation for potentially occurring soft lags was given in 2000, when using a non-linear Monte-Carlo code, Malzac & Jourdain (2000) explored scenarios of an accretion disk corona system consisting of thermal Comptonization of flares arising from either the corona or the disk. They predicted that if the flares arise from the corona, lags should invert from hard to soft at some frequency related to the size of the emitting region on time scales between 10 H/c for soft lags and 100 H/c for quasi-steady-state. These authors presented illustrative numerical simulations, but made no attempt to fit the data for any source. Two other leading theories have emerged since the first discovery of soft lags in 2009, centering either on the reflection of hard emission off a cool electron population, causing down-scattering (Zoghbi et al. 2010) or on the reprocessing of radiation in a zone in which the electrons cool on a timescale comparable to the lag time (Miller et al. 2010). Zoghbi proposed that the lags are the result of spatial reverberation. In their model, the soft emission is generated when hard photons originating near the event horizon in the corona are reflected off the surrounding accretion disk, which extends from an inner radius of $\sim 1.3\,R_g$ to an outer radius $\sim 400\,R_g$, where $R_g = GM/c^2$ is the gravitational radius for the central black hole. They state that this type of reflection scenario naturally produces soft time lags with a magnitude comparable to the light travel time between the corona and the reflecting region of the optically thick disk. A time lag (or equivalently in their model the light travel time between the corona and the reflector) of $\sim 30\,\mathrm{s}$ therefore correlates with a black hole mass of $M \sim 2 \times 10^6\,M_\odot$, which is consistent with the uncertain mass of the H707 black hole (e.g., Zhou & Wang 2005). As an alternative model, Miller et al. (2010) proposed that the soft lags in H707 are caused by a partially opaque reverberating region with a lower size limit of 1000 light-seconds from the black hole corresponding to 100 R_g for a black hole mass of $M \sim 2 \times 10^6\,M_\odot$. In Miller's model, this region has decreasing opacity with increasing energy and has scattering or reflection present in all X-ray bands. The issues with these models are next reviewed.

1.4.3 Problems with Previous Models

Shortly after the discovery of soft lags in H707 by Fabian et al. (2009), Zoghbi et al. (2010) stated that Malzac & Jourdain's (2000) model of having the whole spectrum originate in the corona was inconsistent with the spectral variability properties between the bands above and below 1 keV. Zoghbi et al. (2010) state that the abrupt change in variability above and below 1 keV in their time bins of 10-ks implies two separate energy components that arise from different sources. As evidence of this, Zoghbi et al. (2010) demonstrate plots that provide evidence that the flux of the soft energy band below 1 keV is steady regardless of the change in overall count rate, whereas the flux of the hard energy band above 1 keV correlates with the overall flux changes of the source. However, this does not accurately rule out Comptonization as the cause of the time lags as will be discussed in the discussion and conclusions.

Zoghbi's reverberation model has had multiple journal articles dispute its validity. Miller et al. (2010) reviewed lags in an additional larger energy band and proposed that by doing so, Zoghbi's reflection model predictions are ruled out at confidence > 99.9 per cent. As another detriment to Zoghbi's model, Miller et al. (2010) add that Zoghbi's model is overly complicated and that it requires separate mechanisms to reproduce the hard and soft lags where the soft lags are produced by reverberation. Gardner & Done (2014) investigated soft lags for a different NLS1 AGN and investigated the validity of the reflection model. They theorize that reflection alone is unable to produce soft lags alone without an additional combination of emission from the accretion flow and reprocessed emission, which provides a majority of the soft X-ray excess. They propose that much of the source radiation that is directed toward the disc is actually thermalized and reprocessed in the disc. They state that reflection alone generates high coherence and nearly identical hard and soft band power spectra in disagreement with observations, which shows a drop in coherence between the energy bands at high frequencies as well as much less high-frequency power in the soft band as compared to the hard band. Gardner & Done (2014) state that the cause of this is due to the power law (source photons) and reflection components both contributing to the hard and soft energy bands in a reflection model combined with the small-size scales for a reflection model. Additional evidence that contradicts the reverberation model is from Emmanoulopoulos et al. (2016), in which they presented a study of the PSD of H707 based on a proposed method by Papadakis et al. (2016) to find evidence supporting the reverberation model. In this research, they noted that the X-ray reflection component should be a "filtered echo" of the primary X-ray source and so the PSD of the reflection component should be equal to the convolution of the primary emission with the response function of the disc. They looked for these "reflection features" in the 5-7 keV and 0.5-1 keV bands, where the X-ray reflection component is expected to dominate. However, the study found no evidence of the reverberation model in the PSD results.

Miller's model has also been contested. Zoghbi et al. (2011) contest Miller's model by stating that it does not also look at the energy spectrum and so is not fully consistent. Zoghbi et al. (2011) also point out that Miller's model also requires different mechanisms and so is equally complicated. Additionally, Miller's model requires obscuring clouds close to the line of sight thereby putting specific geometry constraints on the observer.

In this dissertation, I propose an alternative theory for the creation of the soft lags. My model does not suffer from the boot-strapping and kludging of additional physical concepts to established black hole models in order to fit the data. My model instead replicates the observational data with well established physical processes in a straightforward manner using established accretion theory. As will be shown, I obtain the exact solution to a transport equation governing the Fourier transform of a radiation distribution function and then successfully model my results to observational data. The hard lags and the soft lags are a natural outcome of the physics encompassed within my model.

Chapter 2: An Alternative X-ray Fourier Time Lag Model

2.1 Introduction

2.1.1 Overview

The ongoing discussion, analysis, and interpretation of the soft time lags has motivated a new model for the production of the observed hard and soft time lags from AGN. My dissertation explores the possibility that the observed time lags may be the result of thermal and bulk Comptonization occurring in the freely-falling, quasi-spherical coronal region of the accretion flow onto the supermassive black hole. In this scenario, the time-dependent part of the signal (that produces the observed time lags) is the result of episodic emission of ~ 1 keV photons produced near the black hole, which are then Comptonized by the quasi-spherical optically thin coronal cloud, whereas the steady-state X-ray spectrum represents persistent thermal emission produced continuously in the optically thick, thin accretion disk. The episodic emission of the photons may reflect the "clumpy" nature of the accretion flow (e.g., Merloni et al. 2006; Gutierrez et al. 2021).

The theoretical approach is based on obtaining the exact solution to the transport equation governing the Fourier transform of the radiation distribution function. This method is convenient since it allows the direct computation of Fourier-based time lags, which can then be compared with observational data. The time-dependent transport equation includes terms describing bulk and thermal Comptonization, spatial diffusion, advection, and photon injection and escape.

The results obtained for the time lags as a function of Fourier frequency agree well with the observations for H707, without requiring reflection off the accretion disk or specific observer geometry constraints while still allowing for the observed steady-state spectrum to be produced naturally from the accretion disk. The universality of the mass scaling law discovered by De Marco et al. (2013) and Mallick et al. (2021) suggests that the model explored here may be operative in all AGN displaying soft time lags.

My alternative model, for the production of the observed soft time lags from accreting black holes, is based on the radiative transfer occurring in the quasi-spherical region of the coronal accretion flow surrounding the black hole. The model involves the analytical solution of a time-dependent transport equation describing the scattering of seed photons injected into an isothermal, spherically symmetric, accreting plasma cloud, which approximates the quasi-spherical region of the flow onto the central black hole. The seed photons are assumed to be injected as an instantaneous flash of energy. The accretion rate is assumed to be near or above the Eddington limit.

2.1.2 Relation to Previous Work

This transport model builds off of a large body of previous work conducted over the last 35 years. The three investigations that are nearest to this model were studied by Colpi, Titarchuk, and Kroon in 1988, 1997, and 2016 respectively. In 1988, Colpi assumed a spherical geometry and included the effects of both bulk and thermal Comptonization, as well as the spatial transport of radiation via diffusion and advection. However, she solved only the quiescent (steady-state) case for a constant photonic source and most importantly assumed different boundary conditions using a radial boundary condition at the origin and at infinity (Colpi 1988). Titarchuk further studied this model in 1997 and included inner and outer boundaries, but utilized a non-adjustable free-fall velocity profile and again only studied the quiescent equation (Titarchuk et al. 1997). Kroon & Becker (2016) conducted further investigations, but did not account for "bulk" Comptonization in a sub-free-fall advecting cloud and utilized a different density profile. My model builds on all of these previous works by investigating time-dependent solutions using a Fourier transform technique and imposing free-streaming boundary conditions at finite values for the inner and outer radii of the spherical region.

2.2 Time-Dependent Transport Equation

2.2.1 Introduction

I begin by writing down the general time-dependent radiation transport equation describing the evolution of the photon distribution function, $f(\vec{r}, \epsilon, t)$, which is given by (Becker 2003)

$$\frac{\partial f}{\partial t} = -\vec{v} \cdot \vec{\nabla} f + \vec{\nabla} \cdot \left(\kappa \vec{\nabla} f\right) + \left(\vec{\nabla} \cdot \vec{v}\right) \frac{\epsilon}{3} \frac{\partial f}{\partial \epsilon} + \frac{n_e \sigma_{\mathrm{T}} c}{m_e c^2} \frac{1}{\epsilon^2} \frac{\partial}{\partial \epsilon} \left[\epsilon^4 \left(f + k T_e \frac{\partial f}{\partial \epsilon}\right)\right] + Q \ , \quad (2.1)$$

where ϵ is the photon energy, σ_{T} denotes the Thomson cross section, $\vec{v}$ represents the accretion velocity, κ is the spatial diffusion coefficient, k is the Boltzmann constant, T_e denotes the electron temperature, m_e is the electron mass, c is the speed of light, and Q denotes the photon source term. The third and fourth terms on the right-hand side represent the effects of bulk and thermal Comptonization, respectively.

The radiation distribution function, f, is normalized so that the photon number and energy densities, n_r and U_r, respectively, are computed using

$$n_r(\vec{r}, t) = \int_0^\infty \epsilon^2 f(\vec{r}, \epsilon, t) \, d\epsilon \quad \propto \ \mathrm{cm}^{-3} \ , \quad (2.2)$$

and

$$U_r(\vec{r}, t) = \int_0^\infty \epsilon^3 f(\vec{r}, \epsilon, t) \, d\epsilon \quad \propto \ \mathrm{erg\ cm}^{-3} \ . \quad (2.3)$$

The equivalent transport equation in terms of n_r, the photon number density, is shown in Equation 2.4. It is found by applying the integral operator $\int_0^\infty \epsilon^2 d\epsilon$. As a method of validation of the solution of f, I solve for n_r at the end of this chapter.

$$\frac{\partial n_r}{\partial t} = -\vec{v} \cdot \vec{\nabla} n_r + \vec{\nabla} \cdot \left(\kappa \vec{\nabla} n_r\right) - \left(\vec{\nabla} \cdot \vec{v}\right) n_r + \int_0^\infty Q \epsilon^2 d\epsilon, \quad (2.4)$$

As reviewed in Chapter 1, accreting black holes are expected to have spherical coronal regions that may have varying physical parameters depending on the accretion rate. The formation of the coronal region may be due to passage through a shock (Chakrabarti 1989; Das et al. 2009; Becker et al. 2011; Chattopadhyay & Kumar 2016), or due to the accretion of a separate population of matter that is supplied with low angular momentum (Proga & Begelman 2003; Moscibrodzka et al. 2007), or possibly due the removal of a substantial fraction of the angular momentum via a mildly relativistic wind (e.g., Dauser et al. 2012; Done & Jin, 2016). Although coronal descriptions do not necessarily correlate with a specific accretion model, the underlying physics does not change. For instance, based on Figure 1.6, it appears highly plausible that a highly accreting region with optical depth on order of unity will form into a spherical shape. Therefore, for this transport equation I assume a spherically-symmetric cloud and utilize the spherical coordinates $\vec{\nabla} = \left(\frac{\partial}{\partial z}\hat{z} + \frac{1}{r}\frac{\partial}{\partial r}r\hat{r} + \frac{1}{r}\frac{\partial}{\partial \phi}\hat{\phi}\right)$. In a spherically-symmetric region, there is polar and azimuthal symmetry of $\vec{v}$ and $f_{\rm G}$ and so the $\frac{\partial}{\partial \phi}$ and $\frac{\partial}{\partial \theta}$ terms in Equation 2.1 equal zero leaving only radial terms. Since I am considering accretion the radial velocity is negative ($v_r < 0$) for inward flow. Hence, the transport equation can now be rewritten as

$$\frac{\partial f_{\rm G}}{\partial t} = -v_r \frac{\partial f_{\rm G}}{\partial r} + \frac{1}{r^2}\frac{\partial}{\partial r}\left(r^2 \kappa \frac{\partial f_{\rm G}}{\partial r}\right) + \frac{1}{r^2}\frac{\partial}{\partial r}\left(r^2 v_r\right)\frac{\epsilon}{3}\frac{\partial f_{\rm G}}{\partial \epsilon} + \frac{n_e \sigma_{\rm T} c}{m_e c^2}\frac{1}{\epsilon^2}\frac{\partial}{\partial \epsilon}\left[\epsilon^4\left(f_{\rm G} + kT_e \frac{\partial f_{\rm G}}{\partial \epsilon}\right)\right] + \frac{N_0 \delta(r - r_0)\delta(\epsilon - \epsilon_0)\delta(t - t_0)}{4\pi r_0^2 \epsilon_0^2} , \tag{2.5}$$

where $f_{\rm G}(r, r_0, \epsilon, \epsilon_0, t)$ denotes the Green's function, which is the response to the instantaneous injection of N_0 photons of energy ϵ_0, at time t_0, from a source at radius r_0.

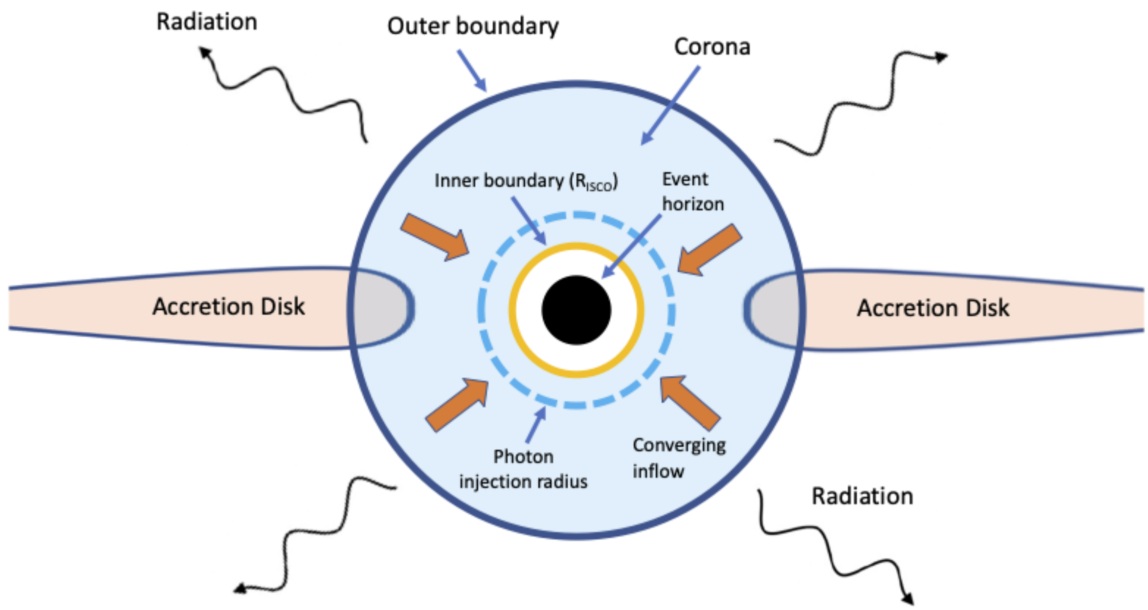

Figure 2.1: Geometry of the physical model.

2.2.2 Model Assumptions

As stated above, the model assumes a spherical coronal cloud that surrounds a black hole. The coronal cloud has both inner and outer boundaries and is accreting. A simplified schematic representation of the model is provided in Figure 2.1. The gas is assumed to be comprised of fully ionized hydrogen and electrons surrounding a black hole. As stated in the introduction, BHBs and AGN spectra have large thermal components which implies large areas of isothermal equilibrium and hence in this model the electrons are assumed to comprise a Maxwellian distribution with a constant temperature T_e. Additionally, due to Comptonization dominating the cooling process (leading to temperatures around 10^8 K), the so-called "thermostat" effect occurs ensuring that the temperature remains constant (e.g., Shapiro et al. 1975). The gas in the spherical region has already passed through the outer critical point, and is therefore necessarily supersonic. The radial velocity, v_r, and the electron number density, n_e, are assumed to follow the free-fall profiles $v_r \propto r^{-1/2}$ and $n_e(r) \propto r^{-3/2}$, respectively. These profiles ensure separability in the partial differential equation. The radial velocity, $v_r(r)$, profile can be written as

$$v_r(r) = \ell \, v_{\rm ff}(r) = -\ell \sqrt{\frac{2GM}{r}} \ , \tag{2.6}$$

where $v_{\rm ff}(r)$ denotes the local free-fall velocity, and the constant ℓ lies in the range $0 \le \ell \le 1$, with $\ell = 1$ corresponding to exact free-fall (Colpi 1988).

Since the accreting gas is assumed to be composed of pure, fully-ionized hydrogen, the spatial diffusion coefficient, κ, shown in Equation (2.5), is related to the electron number density, n_e, via

$$\kappa(r) = \frac{c}{3 n_e(r) \sigma_{\rm T}} \ . \tag{2.7}$$

The electron number density, n_e, is related to the mass accretion rate, $\dot{M}$, via

$$\dot{M} = 4\pi r^2 m_p n_e |v_r| = \text{constant} \ , \tag{2.8}$$

where m_p denotes the proton mass.

2.2.3 Non-dimensionalizing

It is useful to non-dimensionalize the transport equation. Combining Equations (2.6), (2.7), and (2.8), the radial velocity, v_r, the electron number density, n_e, and the spatial diffusion coefficient, κ, can be written as

$$v_r(\tilde{r}) = -\hat{v} c \, \tilde{r}^{-1/2} \ , \ n_e(\tilde{r}) = \frac{\tilde{r}^{-3/2}}{3 \, \sigma_{\rm T} R_g \hat{\kappa}} \ , \ \kappa(\tilde{r}) = \hat{\kappa} R_g c \, \tilde{r}^{3/2} \ , \tag{2.9}$$

where $R_g = GM/c^2$, the dimensionless constants $\hat{v}$ and $\hat{\kappa}$, and the dimensionless radius

$$\tilde{r} \equiv \frac{r}{R_g} \ . \tag{2.10}$$

have been introduced. The constant $\hat{v}$ introduced in Equation (2.9) is related to Colpi's constant ℓ via $\hat{v} = \sqrt{2}\,\ell$. Hence setting $\hat{v} = \sqrt{2}$ yields the exact free-fall case with $v_r(r) = v_{\rm ff}(r)$ (see Equation (2.6)). Furthermore, Equations (2.8) and (2.9) can now be combined to relate $\hat{v}$ and $\hat{\kappa}$ to the accretion rate $\dot{M}$ via

$$\dot{M} = \frac{4\pi R_g m_p \hat{v} c}{3\hat{\kappa}\sigma_{\rm T}} \ . \tag{2.11}$$

It is also of interest to compute the electron scattering optical depth, $\tau(r)$, between radius r and the outer radius of the spherical coronal region, located at $r = r_{\rm out}$. The result obtained is

$$\tau(\tilde{r}) = \int_r^{r_{\rm out}} n_e(r')\sigma_{\rm T}\, dr' = \frac{2\,\dot{m}}{\hat{v}}\left(\tilde{r}^{-1/2} - \tilde{r}_{\rm out}^{-1/2}\right) \ , \tag{2.12}$$

where $\tilde{r} = r/R_g$, $\tilde{r}_{\rm out} = r_{\rm out}/R_g$, and I have utilized Equation (2.9) to substitute for $n_e(r)$. Transforming the spatial coordinate from r to $\tilde{r}$ in the transport equation and substituting for v_r, n_e, and κ using Equation (2.9) yields the result:

$$\begin{aligned}\frac{\partial f_{\rm G}}{\partial t} = {} & \frac{\hat{v}c\tilde{r}^{-1/2}}{R_g}\frac{\partial f_{\rm G}}{\partial \tilde{r}} + \frac{\hat{\kappa}c\tilde{r}^{-2}}{R_g}\frac{\partial}{\partial \tilde{r}}\left(\tilde{r}^{7/2}\frac{\partial f_{\rm G}}{\partial \tilde{r}}\right) - \frac{\hat{v}c\tilde{r}^{-3/2}}{2R_g}\chi\frac{\partial f_{\rm G}}{\partial \chi} \\ & + \frac{c\Theta\tilde{r}^{-3/2}}{3\hat{\kappa}R_g}\frac{1}{\chi^2}\frac{\partial}{\partial \chi}\left[\chi^4\left(f_{\rm G} + \frac{\partial f_{\rm G}}{\partial \chi}\right)\right] + \frac{N_0\delta(\tilde{r}-\tilde{r}_0)\delta(\chi-\chi_0)\delta(t-t_0)}{4\pi r_0^2\epsilon_0^2 kT_e R_g} \ ,\end{aligned} \tag{2.13}$$

where I have introduced the dimensionless photon energy, χ, and the dimensionless temperature, Θ, using

$$\chi \equiv \frac{\epsilon}{kT_e} \ , \quad \Theta \equiv \frac{kT_e}{m_e c^2} \ . \tag{2.14}$$

2.2.4 The Trapping Radius

In spherically-symmetric accretion flows, a significant radial location exists where spatial transport is dominated by advection because background flow exceeds diffusion velocity. Hence, the spatial transport of the radiation is dominated by inward-bound advection for $r < r_t$, and by outward-bound diffusion for $r > r_t$, where r_t is the "trapping radius," defined by (Payne & Blandford 1981; Colpi 1988)

$$r_t \equiv \frac{3\dot{M}\sigma_{\rm T}}{4\pi m_p c} \ . \tag{2.15}$$

In order to derive this relationship, first note that the mean free path for photons scattering in a gas composed of fully-ionized hydrogen is given by

$$\ell = \frac{1}{n_e \sigma_{\rm T}} \ . \tag{2.16}$$

Next, for a homogeneous spherical corona, the radial diffusion velocity and optical depth can be approximated by writing

$$v_{\rm diff} = \frac{1}{3}\frac{c}{\tau} \ , \quad \tau = \frac{r}{\ell} \ . \tag{2.17}$$

Combining Equations (2.16) and (2.17) yields

$$v_{\rm diff} = \frac{1}{3}\frac{c\,\ell}{r} = \frac{1}{3}\frac{c}{n_e \sigma_{\rm T} r} \ . \tag{2.18}$$

Next, combining the mass accretion rate equation (Equation (2.8)) with Equation (2.18) gives

$$v_{\rm diff} = \frac{1}{3}\frac{c}{\sigma_{\rm T} r}\frac{4\pi r^2 m_p |v_r|}{\dot{M}} = \frac{4\pi r\, m_p\, c\,|v_r|}{3\,\sigma_{\rm T}\dot{M}} \ . \tag{2.19}$$

As noted earlier, at the trapping radius, r_t, the diffusion and flow velocities are equal (but opposite), so $v_{\rm diff} = |v_r|$, which yields the given equation for the trapping radius in Equation (2.15),

$$r_t = \frac{3\dot{M}\sigma_{\rm T}}{4\pi\, c\, m_p} \ . \tag{2.20}$$

In terms of the non-dimensional substitutions, using Equation (2.11), the trapping radius can be expressed in the form

$$\frac{r_t}{R_g} = \frac{\hat{v}}{\hat{\kappa}} = 3\dot{m} \ , \tag{2.21}$$

where the dimensionless accretion rate, $\dot{m}$, is defined by

$$\dot{m} \equiv \frac{\dot{M}}{\dot{M}_{\rm E}} \ , \tag{2.22}$$

and the Eddington accretion rate, $\dot{M}_{\rm E}$, is defined by

$$\dot{M}_{\rm E} \equiv \frac{4\pi G M m_p}{c\sigma_{\rm T}} \ . \tag{2.23}$$

2.2.5 Eddington Luminosity and Accretion Rate

As noted in Chapter 1, the Eddington accretion rate is related to the Eddington luminosity by Equation (1.1). The first half of that equation is shown again here,

$$L_{\mathrm{E}} = \dot{M}_{\mathrm{E}}\, c^2 \ . \tag{2.24}$$

This relationship provides the maximum energy per unit time released by a gas that is bound by a central mass such as a black hole. It is found by equating the competing forces of gravity, F_g, and radiation, F_{rad} of the gas surrounding the massive body. Assuming a gas of fully-ionized pure hydrogen,

$$F_g = F_{\mathrm{rad}} \quad \rightarrow \quad \frac{GMm_p}{r^2} = \frac{L_E \sigma_T}{4\pi r^2 c} \ , \tag{2.25}$$

Rearranging terms and solving for L_E gives,

$$L_{\mathrm{E}} = \frac{4\pi G m_p c}{\sigma_{\mathrm{T}}} M = 1.26 \times 10^{38} \ \mathrm{erg\ s^{-1}} \left(\frac{M}{M_\odot} \right) \ . \tag{2.26}$$

If the radiation pressure is greater than the gravitational pressure, then the equality will be broken and the gas will be blown away. Hence, this luminosity limit necessarily implies a maximum mass and a maximum accretion limit. Combining Equations (2.24) and (5.8), the original Equation (1.1) is found,

$$L_{\mathrm{E}} = \dot{M}_{\mathrm{E}}\, c^2 = \frac{4\pi G M m_p c}{\sigma_{\mathrm{T}}} \ . \tag{2.27}$$

2.2.6 Final Non-dimensional Transport Equation

As noted by Payne & Blandford (1981) and Colpi (1988), the physical significance of the trapping radius motivates a transformation of the spatial variable $\tilde{r}$ in the transport equation to the new spatial variable y, defined by

$$y \equiv \frac{r_t}{r} = \frac{\hat{v}}{\hat{\kappa}\tilde{r}} \ , \tag{2.28}$$

so that the trapping radius corresponds to $y = 1$, and the radiation is trapped in the region with $y > 1$ ($r < r_t$). Finishing transforming the non-dimensionalized transport equation by making the change of variables from $\tilde{r}$ to y yields

$$\begin{aligned}\frac{\partial f_{\rm G}}{\partial q} = \frac{\Theta}{3\hat{\kappa}\hat{v}}\frac{y^{3/2}}{\chi^2}\frac{\partial}{\partial\chi}\left[\chi^4\left(f_{\rm G} + \frac{\partial f_{\rm G}}{\partial\chi}\right)\right] + y^4\frac{\partial}{\partial y}\left(y^{-3/2}\frac{\partial f_{\rm G}}{\partial y}\right) - y^{5/2}\frac{\partial f_{\rm G}}{\partial y} \\ - \frac{y^{3/2}\chi}{2}\frac{\partial f_{\rm G}}{\partial\chi} - \frac{N_0 y_0^2\hat{\kappa}^3 y^2\delta(y-y_0)\delta(\chi-\chi_0)\delta(q-q_0)}{4\pi x_0^2 R_g^3(kT_e)^3\hat{v}^3}\ ,\end{aligned} \tag{2.29}$$

where the dimensionless time, q, is related to the time t, via

$$q \equiv \frac{\hat{\kappa}^{3/2}}{\hat{v}^{1/2}}\frac{t\,c}{R_g}\ . \tag{2.30}$$

and q_0, y_0, and χ_0 are the dimensionless injection time, radius, and energy.

2.3 Fourier Transform Method

2.3.1 Overview

In order to compute theoretical time lags using Equation (1.20), the transport equation formalism must be used to evaluate the Fourier transforms of the light curves observed at the soft and hard channel energies, ϵ_s and ϵ_h, respectively. The required solution for the Fourier transform can be obtained by performing a Fourier transformation of the partial differential transport equation, Equation (2.29). This yields an ordinary differential equation satisfied by the Green's function Fourier transform, $F_{\rm G}$, which is related to the Green's function, $f_{\rm G}$, via the fundamental definition (cf. Equation (1.18))

$$F_{\rm G}(r,\epsilon,\omega) \equiv \int_{-\infty}^{+\infty} f_{\rm G}(r,\epsilon,t)\,e^{i\omega t}\,dt\ . \tag{2.31}$$

The Fourier transform can also be expressed in terms of the dimensionless time, q, by writing

$$F_{\rm G}(r,\epsilon,\tilde{\omega}) = \frac{\hat{v}^{1/2}}{\hat{\kappa}^{3/2}}\frac{R_g}{c}\int_{-\infty}^{+\infty} f_{\rm G}(r,\epsilon,q)\, e^{i\tilde{\omega}q}\, dq \ , \tag{2.32}$$

where the dimensionless Fourier frequency, $\tilde{\omega}$, is related to ω via

$$\tilde{\omega} \equiv \frac{\hat{v}^{1/2}}{\hat{\kappa}^{3/2}}\frac{R_g}{c}\,\omega \ . \tag{2.33}$$

Performing the Fourier transformation of Equation (2.29) by applying the operator $\int_{-\infty}^{+\infty} e^{i\tilde{\omega}q} dq$ yields an ordinary differential equation for the Fourier transform Green's function, $F_{\rm G}$ given by

$$\begin{aligned} -i\tilde{\omega}F_{\rm G} =& - y^{5/2}\frac{\partial F_{\rm G}}{\partial y} - \frac{y^{3/2}\chi}{2}\frac{\partial F_{\rm G}}{\partial \chi} + y^4\frac{\partial}{\partial y}\left(y^{-3/2}\frac{\partial F_{\rm G}}{\partial y}\right) \\ &+ \frac{\Theta\, y^{3/2}}{3\hat{v}\hat{\kappa}\chi^2}\frac{\partial}{\partial \chi}\left[\chi^4\left(F_{\rm G} + \frac{\partial F_{\rm G}}{\partial \chi}\right)\right] + \frac{N_0 y_0^4 \hat{\kappa}^{3/2}\delta(y-y_0)\delta(\chi-\chi_0)e^{i\tilde{\omega}q_0}}{4\pi R_g^2 c(kT_e)^3\chi_0^2\hat{v}^{5/2}} . \end{aligned} \tag{2.34}$$

2.3.2 Separation of Functions

In order to solve Equation (2.34) to determine the solution for the Fourier transform Green's function, $F_{\rm G}$, I must separate the differential equation. Previously I noted that with the free-fall profile, all of the terms are separable with the exception of the source term. However, for $\chi \neq \chi_0$, the source term vanishes. Consequently Equation (2.34) can be separated using the function

$$F_\lambda(y,\chi) = G(y)\,H(\chi) \ , \tag{2.35}$$

where λ denotes the separation constant, and the functions $G(y)$ and $H(\chi)$ represent the spatial and energy separation functions, respectively. Substituting Equation (2.35) into

Equation (2.34) and rearranging terms, for $\chi \neq \chi_0$,

$$-i\tilde{\omega} y^{-3/2} + \frac{y}{G}\frac{dG}{dy} - \frac{y^{5/2}}{G}\frac{d}{dy}\left(y^{-3/2}\frac{dG}{dy}\right)$$
$$= \frac{\Theta}{3\hat{v}\hat{\kappa}}\frac{1}{\chi^2 H}\frac{d}{d\chi}\left[\chi^4\left(H + \frac{dH}{d\chi}\right)\right] - \frac{\chi}{2H}\frac{dH}{d\chi} = \frac{\lambda}{2} \ . \tag{2.36}$$

The separation constant λ is independent of the coordinates y and χ, and therefore one can obtain two distinct ordinary differential equations satisfied by the functions $G(y)$ and $H(\chi)$. The equations obtained are

$$y\frac{d^2G}{dy^2} - \left(\frac{3}{2} + y\right)\frac{dG}{dy} + \frac{\lambda}{2}G + i\tilde{\omega} y^{-3/2} G = 0 \ , \tag{2.37}$$

and

$$\frac{1}{\chi^2}\frac{d}{d\chi}\left[\chi^4\left(H + \frac{dH}{d\chi}\right)\right] - \delta\chi\frac{dH}{d\chi} - \delta\lambda H = 0 \ , \tag{2.38}$$

where

$$\delta \equiv \frac{3\hat{v}\hat{\kappa}}{2\Theta} \ . \tag{2.39}$$

2.3.3 Boundary Conditions

The spatial boundary conditions utilized in this model are based on the transition to free-streaming that must occur at the inner and outer surfaces of the spherical coronal region. The free-streaming or "absorbing" boundary condition was also discussed by Titarchuk et al. (1997). It is important to note that alternative boundary conditions such as those utilized by Colpi (1988) (adiabatic inner and diffusive outer), as well as all combinations thereof, have been derived, calculated, and compared with observational data (See the appendix for further derivations). In doing so, it was determined that the model's inner boundary is insensitive to either a free-streaming finite boundary or an adiabatic boundary at the origin. However, the diffusive outer boundary which equates to an infinite cloud was unable to successfully reproduce the observational data. The specific (spatial) radiation flux, $\mathfrak{F}$, also referred to as the "streaming function," is given by (Becker 1992)

$$\mathfrak{F}(\epsilon, r, t) = -\kappa \frac{\partial f_{\rm G}}{\partial r} - \frac{v_r \epsilon}{3} \frac{\partial f_{\rm G}}{\partial \epsilon} \ . \tag{2.40}$$

The inner and outer boundaries of the spherical coronal region are located at $r = r_{\rm in}$ and at $r = r_{\rm out}$, respectively, and the corresponding values of the dimensionless location parameter y are (see Equation (2.28))

$$\begin{aligned} y_{\rm in} &= \frac{R_g \hat{v}}{\hat{\kappa}\, r_{\rm in}} \ , \\ y_{\rm out} &= \frac{R_g \hat{v}}{\hat{\kappa}\, r_{\rm out}} \ . \end{aligned} \tag{2.41}$$

The free-streaming boundary condition operative at the inner and outer boundaries can be written as

$$\begin{aligned} -\kappa \frac{\partial f_{\rm G}}{\partial r} &= -c f_{\rm G} \ , \quad r = r_{\rm in} \ , \quad \text{(inner boundary)} \ , \\ -\kappa \frac{\partial f_{\rm G}}{\partial r} &= c f_{\rm G} \ , \quad r = r_{\rm out} \ , \quad \text{(outer boundary)} \ . \end{aligned} \tag{2.42}$$

Transforming the free-streaming boundary conditions from r to y yields

$$\begin{aligned} (\hat{v}\hat{\kappa}y)^{1/2} \frac{\partial f_{\rm G}}{\partial y} &= -\, f_{\rm G} \ , \quad y = y_{\rm in} \ , \quad \text{(inner boundary)} \ , \\ (\hat{v}\hat{\kappa}y)^{1/2} \frac{\partial f_{\rm G}}{\partial y} &= \ f_{\rm G} \ , \quad y = y_{\rm out} \ , \quad \text{(outer boundary)} \ . \end{aligned} \tag{2.43}$$

Fourier transformation of Equations (2.43) demonstrates that the spatial boundary conditions satisfied by the Green's function Fourier transform, $F_{\rm G}$, are given by

$$
\begin{aligned}
(\hat{v}\hat{\kappa}y)^{1/2}\frac{\partial F_{\rm G}}{\partial y} &= -\,F_{\rm G} \ , \quad y = y_{\rm in} \ , \quad \text{(inner boundary)} \ , \\
(\hat{v}\hat{\kappa}y)^{1/2}\frac{\partial F_{\rm G}}{\partial y} &= \ F_{\rm G} \ , \quad y = y_{\rm out} \ , \quad \text{(outer boundary)} \ .
\end{aligned}
\tag{2.44}
$$

By combining Equations (2.35) and (2.44), it is found that the spatial separation function $G(y)$ satisfies the free-streaming boundary conditions

$$
(\hat{v}\hat{\kappa}y)^{1/2}G' + G = 0 \ , \qquad y = y_{\rm in} \ , \tag{2.45}
$$

$$
(\hat{v}\hat{\kappa}y)^{1/2}G' - G = 0 \ , \qquad y = y_{\rm out} \ , \tag{2.46}
$$

where primes denote differentiation with respect to y. The eigenfunctions, $G_n(y)$, represent the discrete set of solutions to Equation (2.37) that simultaneously satisfy both the inner and outer boundary conditions given by Equations (2.45) and (2.46), respectively. The corresponding eigenvalues for the separation constant λ are denoted by λ_n.

2.3.4 Eigenfunctions

Spatial Eigenfunctions

The global solutions for the spatial eigenfunctions $G_n(y)$ are obtained using a three-step process. The first step is to numerically solve the ordinary differential equation, Equation (2.37), starting with the inner boundary condition (Equation (2.45)), imposed at $y = y_{\rm in}$. This yields the inner solution, denoted by $G_{\rm in}(y)$. The second step is to carry out the numerical integration again, this time starting with the outer boundary condition (Equation (2.46)), imposed at $y = y_{\rm out}$, which yields the outer solution, $G_{\rm out}(y)$.

For general, arbitrary values of the separation constant, λ, the inner and outer solutions are linearly independent functions. However, for certain special values of λ, the Wronskian of the inner and outer solutions vanishes, i.e.,

$$\mathfrak{W}(y_*) = 0 \ , \tag{2.47}$$

where

$$\mathfrak{W}(y_*) \equiv G_{\rm in}(y_*)\, G'_{\rm out}(y_*) - G_{\rm out}(y_*)\, G'_{\rm in}(y_*) \ , \tag{2.48}$$

and y_* is located anywhere in the computational domain, so that $y_{\rm in} \le y_* \le y_{\rm out}$. The eigenvalues λ_n are the roots of Equation (2.47). Note that the Fourier frequency, $\tilde{\omega}$, appears in Equation (2.37), and therefore it follows that a unique set of eigenvalues λ_n is obtained for each value of $\tilde{\omega}$.

Energy Eigenfunctions

The energy separation functions, $H(\chi)$, satisfy the second-order ordinary differential equation given by Equation (2.38). In addition, in order to obtain convergent results for the photon number and energy densities using Equations (2.2) and (2.3), H must not increase faster than ϵ^{-3} as $\epsilon \to 0$. Likewise, H must decrease faster than ϵ^{-4} as $\epsilon \to \infty$. Additionally, H must be continuous at the injection energy $\chi = \chi_0$ in order to avoid an infinite diffusive flux in the energy space. Becker & Wolff (2007) obtained the exact solution to Equation (2.38) satisfying the required boundary and continuity conditions (Becker & Wolff 2007, Equation (48)), which can be written as

$$H_n(\chi, \chi_0) = \chi^{\kappa-4} e^{-\chi/2} M_{\kappa,\mu}(\chi_{\rm min}) W_{\kappa,\mu}(\chi_{\rm max}) \ , \tag{2.49}$$

where $M_{\kappa,\mu}$, and $W_{\kappa,\mu}$ denote the Whittaker functions,

$$\chi_{\rm min} \equiv \min(\chi, \chi_0) \ , \qquad \chi_{\rm max} \equiv \max(\chi, \chi_0) \ , \tag{2.50}$$

and the parameters κ and μ are given by

$$\kappa \equiv \frac{1}{2}\,(\delta + 4) \ , \qquad \mu \equiv \frac{1}{2}\left[(3-\delta)^2 + 4\,\delta\lambda_n\right]^{1/2} \ . \tag{2.51}$$

2.3.5 Orthogonality

The final closed-form solution for the Fourier transform $F_{\rm G}$ can be expressed as an infinite series if I can demonstrate that the spatial eigenfunctions, $G_n(y)$, form an orthogonal set. Orthogonality of the spatial eigenfunctions can be established as follows. First, I rewrite the separated spatial equation, Equation (2.28) which is shown below,

$$y\frac{d^2G}{dy^2} - \left(\frac{3}{2} + y\right)\frac{dG}{dy} + \frac{\lambda}{2}\,G + i\tilde{\omega}y^{-3/2}G = 0 \ , \tag{2.52}$$

in the Sturm-Liouville form

$$\frac{d}{dy}\left[S(y)\frac{dG_n}{dy}\right] + Q(y)G_n + \frac{\lambda_n}{2}\Omega(y)G_n = 0 \ , \tag{2.53}$$

where the weight function, $\Omega(y)$, is defined by

$$\Omega(y) = y^{-5/2}e^{-y} \ , \tag{2.54}$$

and the functions $S(y)$ and $Q(y)$ are defined by

$$\begin{aligned} S(y) &= y^{-3/2}e^{-y} \ , \\ Q(y) &= i\tilde{\omega}y^{-4}e^{-y} \ . \end{aligned} \tag{2.55}$$

Next, I assume that λ_n and λ_m represent distinct eigenvalues associated with the spatial eigenfunctions G_n and G_m, respectively. Equation (2.53) is then multiplied by G_m and the result is subtracted from the same equation with the indices n and m interchanged. After some algebra, the result obtained is

$$G_m \frac{d}{dy}\left[S(y)\frac{dG_n}{dy}\right] - G_n \frac{d}{dy}\left[S(y)\frac{dG_m}{dy}\right] = (\lambda_m - \lambda_n)\Omega(x)G_n G_m \ . \tag{2.56}$$

Integration by parts between the inner and outer radii y_{in} and y_{out} yields

$$S(y)\left[G_m \frac{dG_n}{dy} - G_n \frac{dG_m}{dy}\right]\Bigg|_{y_{\text{in}}}^{y_{\text{out}}} = (\lambda_m - \lambda_n)\int_{y_{\text{in}}}^{y_{\text{out}}} \Omega(y)G_n(y)G_m(y)\, dy \ . \tag{2.57}$$

Utilizing the spatial free-streaming boundary conditions at the inner and outer radii (Equations (2.36) and (2.37)), the left-hand side of Equation (2.57) vanishes giving,

$$\int_{y_{\text{in}}}^{y_{\text{out}}} \Omega(y)G_n(y)G_m(y)\, dy = 0 \ , \quad \lambda_n \neq \lambda_m \ . \tag{2.58}$$

This establishes that the spatial eigenfunctions G_n and G_m are orthogonal with respect to the weight function $\Omega(y)$ in the computational domain located between the inner and outer free-streaming boundaries located at $y = y_{\text{in}}$ and $y = y_{\text{out}}$, respectively. Similarly, note that this same procedure is used for the alternate boundary conditions in Appendix A giving the same result.

2.3.6 Final Closed-Form Solution

Since the spatial eigenfunctions have been shown to form a complete orthogonal set, it is possible to express the Fourier transform Green's function, F_{G}, using the infinite series

$$F_{\text{G}}(y_0, y, \chi_0, \chi, \tilde{\omega}) = \sum_{n=1}^{N_{\max}} C_n G_n(y, y_0) H_n(\chi, \chi_0) \ , \tag{2.59}$$

where y_0 indicates the injection location, and $N_{\rm max}$ denotes the maximum index included in the sum, which must be large enough to ensure convergence of the numerical results for the time lags. The expansion coefficients, C_n, can be determined by exploiting the orthogonality of the spatial eigenfunctions and applying the derivative jump condition

$$\lim_{\varepsilon \to 0} \Delta \left[\chi^4 \frac{\partial F_{\rm G}}{\partial \chi} \right] \Bigg|_{\chi=\chi_0-\varepsilon}^{\chi=\chi_0+\varepsilon} = \frac{-\delta N_0 \hat{\kappa}^{3/2} \delta(y-y_0) e^{i\tilde{\omega} q_0} y^{5/2}}{2\pi \hat{v}^{5/2} R_g^2 c (m_e c^2)^3 \Theta^3} \ , \tag{2.60}$$

which is obtained by integrating Equation (2.34) over a small region in energy space around $\chi = \chi_0$. Equation (2.59) is now substituted into Equation (2.60) to obtain

$$\sum_{n=1}^{N_{\rm max}} C_n G_n(y) \chi_0^{\kappa-4} e^{-\chi_0/2} \mathcal{W}(\chi_0) = \frac{-\delta N_0 \hat{\kappa}^{3/2} \delta(y-y_0) e^{i\tilde{\omega} q_0} y^{5/2}}{2\pi \hat{v}^{5/2} R_g^2 c (m_e c^2)^3 \Theta^3 \chi_0^4} \ , \tag{2.61}$$

where the Wronskian, $\mathcal{W}(\chi_0)$, is defined by (Becker & Wolff 2007)

$$\mathcal{W}(\chi_0) \equiv M_{\kappa,\mu}(\chi_0) W'_{\kappa,\mu}(\chi_0) - W_{\kappa,\mu}(\chi_0) M'_{\kappa,\mu}(\chi_0) = \frac{-\Gamma(1+2\mu)}{\Gamma(\mu-\kappa+1/2)} \ , \tag{2.62}$$

and primes denote differentiation with respect to χ. The final result in Equation (2.62) is obtained using Equation (55) from Becker & Wolff (2007).

The solution for the expansion coefficients, C_n, is obtained by multiplying Equation (2.61) by $G_m(y)\Omega(y)$ where $\Omega(y)$ is the weight function derived above, and then integrating with respect to y from $y_{\rm in}$ to $y_{\rm out}$. Utilizing the orthogonality of the spatial eigenfunctions after some algebra, the final expression obtained for C_n is

$$C_n = \frac{\delta N_0 \hat{\kappa}^{3/2} G_n(y_0) \Omega(y_0) e^{\chi_0/2} e^{i\tilde{\omega} q_0} {y_0}^{5/2} \Gamma(\mu - \kappa + \frac{1}{2})}{2\pi \hat{v}^{5/2} R_g^2 c (m_e c^2)^3 \Theta^3 \chi_0^{\kappa} \mathfrak{I}_n \Gamma(1+2\mu)} \ , \tag{2.63}$$

where the quadratic normalization integrals, $\mathfrak{I}_n$, are defined by

$$\mathfrak{I}_n \equiv \int_{y_{\rm in}}^{y_{\rm out}} \Omega(y)\, G_n^2(y)\, dy \ . \tag{2.64}$$

Combining Equations (2.59) and (2.63), the final closed-form solution for the Fourier transform Green's function, $F_{\rm G}$, can be written as

$$\begin{aligned} F_{\rm G}(y_0, y, \chi_0, \chi, \tilde{\omega}) = & \frac{\delta N_0 \hat{\kappa}^{3/2} \chi^{\kappa-4} \Omega(y_0) e^{(\chi_0-\chi)/2} e^{i\tilde{\omega} q_0} {y_0}^{5/2}}{2\pi \hat{v}^{5/2} R_g^2 c (m_e c^2)^3 \Theta^3 \chi_0^\kappa} \\ & \times \sum_{n=1}^{N_{\rm max}} \frac{\Gamma(\mu-\kappa+\frac{1}{2})}{\mathfrak{I}_n \Gamma(1+2\mu)} G_n(y_0) G_n(y) \times M_{\kappa,\mu}(\chi_{\rm min}) W_{\kappa,\mu}(\chi_{\rm max}) \ , \end{aligned} \tag{2.65}$$

where $\chi_{\rm min}$, $\chi_{\rm max}$, κ, and μ are computed using Equations (2.50) and (2.51). Equation (2.65) gives the final solution for the Fourier transform, $F_{\rm G}$, of the radiation Green's function, $f_{\rm G}$, evaluated at energy χ, location y, and Fourier frequency $\tilde{\omega}$. The solution describes the response to the injection of N_0 photons at location y_0 and time q_0, with energy χ_0.

2.4 Time Lag Computation

Although Equation (2.65) represents the fundamental solution for the Fourier transform of the radiation field *inside* the spherically symmetric accretion flow, it remains necessary to compute the Fourier transform of the *escaping* radiation field in order to compute the observed time lags. The time-dependent X-ray photon count-rate spectrum observed at the detector, $\mathscr{F}_\epsilon(\epsilon)$, is directly related to the radiation distribution escaping from the outer edge of the spherical region, located at radius $r = r_{\rm out}$. Since the boundary condition at the outer radius is free-streaming (Equation (2.42)), the computation of the escaping radiation spectrum is self-consistent and the time-dependent X-ray photon count-rate spectrum observed at the detector is simply given by

$$\mathscr{F}_\epsilon(\epsilon, t) = c \left(\frac{r_{\rm out}}{D}\right)^2 \epsilon^2 f_{\rm G}(r_{\rm out}, \epsilon, t) \quad \propto \ {\rm cm}^{-2} \ {\rm s}^{-1} \ {\rm erg}^{-1} \ , \tag{2.66}$$

where D is the distance to the source. Further discussion of this derivation is given in Section 4.6.

In order to utilize the formalism developed here to compute the observed time lags, the Fourier transform of the observed count-rate spectrum, denoted by $\tilde{\mathscr{F}}_\epsilon(\epsilon, \omega)$ and given by

$$\tilde{\mathscr{F}}_\epsilon(\epsilon, \omega) = \int_{-\infty}^{+\infty} \mathscr{F}_\epsilon(\epsilon, t) \, e^{i\omega t} \, dt \ , \tag{2.67}$$

or, equivalently (cf. Equation (2.32)),

$$\tilde{\mathscr{F}}_\epsilon(\epsilon, \tilde{\omega}) = \frac{\hat{\upsilon}^{1/2}}{\hat{\kappa}^{3/2}} \frac{R_g}{c} \int_{-\infty}^{+\infty} \mathscr{F}_\epsilon(\epsilon, q) \, e^{i\tilde{\omega} q} \, dq \ . \tag{2.68}$$

must be evaluated. Applying a Fourier transformation to both sides of Equation (2.66) by applying the operator $\int_{-\infty}^{+\infty} e^{i\tilde{\omega} q} dq$ yields

$$\tilde{\mathscr{F}}_\epsilon(\epsilon, \tilde{\omega}) = c \left(\frac{r_{\rm out}}{D}\right)^2 \epsilon^2 F_{\rm G}(r_{\rm out}, \epsilon, \tilde{\omega}) \ , \tag{2.69}$$

where $F_{\rm G}$ is evaluated using Equation (2.65).

The theoretical soft and hard energy light curves, $s(t)$ and $h(t)$, respectively, required to compute the time lags using Equation (1.20) are related to the photon count-rate spectrum, $\mathscr{F}_\epsilon(\epsilon, t)$, via Equations (1.19). Applying a Fourier transformation to Equations (1.19) yields the corresponding expressions

$$S(\tilde{\omega}) = \tilde{\mathscr{F}}_\epsilon(\epsilon_s, \tilde{\omega}) \ ,$$
$$H(\tilde{\omega}) = \tilde{\mathscr{F}}_\epsilon(\epsilon_h, \tilde{\omega}) \ , \tag{2.70}$$

where S and H denote the soft- and hard-energy light curve Fourier transforms, respectively, and the function $\tilde{\mathscr{F}}_\epsilon$ is evaluated using Equation (2.69). Finally now, the Fourier time lag, δt, is evaluated using Equation (1.20) where the phase lag is calculated using Equation (1.21).

In order to compute X-ray time lags using this theoretical model, initially five parameters must be specified, namely: (1) the black hole mass, M; (2) the dimensionless accretion rate, $\dot{m} = \dot{M}/\dot{M}_{\rm E}$; (3) the dimensionless velocity parameter, $\hat{v}$; (4) the dimensionless inner radius, $\tilde{r}_{\rm in} = r_{\rm in}/R_g$; and (5) the dimensionless outer radius, $\tilde{r}_{\rm out} = r_{\rm out}/R_g$. With these values inputted, the value of $\hat{\kappa}$ is calculated using Equation (2.21) which is given by $\hat{\kappa} = \hat{v}/(3\dot{m})$. Next, a corresponding vector of values for the dimensionless Fourier frequency, $\tilde{\omega}$, using Equation (2.33) is generated. Utilizing these values, the set of eigenvalues and spatial eigenfunctions are determined following the method outlined in Section 2.3.4.

After determining the set of eigenvalues and spatial eigenfunctions for each selected value of the dimensionless Fourier frequency, $\tilde{\omega}$, the remaining theory parameters are varied in order to obtain an acceptable fit to the observed time lags. The remaining four theory parameters comprise (1) the energy of the injected seed photons, ϵ_0; (2) the dimensionless electron temperature $\Theta = kT_e/(m_e c^2)$; (3) the hard photon channel energy, ϵ_h; and (4) the soft photon channel energy, ϵ_s.

2.5 Model Validation

Model validation is a key issue in a complex calculation such as the one being performed. One effective way to validate the model is to compute and compare the Fourier transform of the photon number density distribution using two methods.

2.5.1 Method 1: Integration of the Green's Function

First, utilizing software such as Mathematica, I can numerically integrate the Fourier transformed transport equation, Equation (2.49), in order to perform the first half of my model validation:

$$N_{\mathrm{G}} = \int_0^\infty \epsilon^2 F_{\mathrm{G}} d\epsilon \ . \tag{2.71}$$

This method is relatively straightforward and simple to implement and the results can then be compared to the results with the solution for N_{G} found in the next section.

2.5.2 Method 2: Integration of the Differential Equation

The second method I can use to compute the Fourier transform of the photon number density distribution is to analytically determine N_{G}. One can transform Equation (2.5) to n_{G}, the photon number density, and after non-dimensionalizing, directly solve for the dimensionless Fourier transform of this, $N_{\mathrm{G}}(\tilde{\omega})$, defined as:

$$N_{\mathrm{G}}(\tilde{\omega}) = \frac{\hat{\upsilon}^{1/2}}{\hat{\kappa}^{3/2}} \frac{R_g}{c} \int_{-\infty}^{+\infty} n_{\mathrm{G}}(q)\, e^{i\tilde{\omega}q}\, dq \ , \tag{2.72}$$

where the dimensionless Fourier frequency, $\tilde{\omega}$, is related to ω via

$$\tilde{\omega} \equiv \frac{\hat{\upsilon}^{1/2}}{\hat{\kappa}^{3/2}} \frac{R_g}{c}\, \omega \ . \tag{2.73}$$

The solution of this is then numerically compared with the results of Equation (2.71). This comparison allows for a computational validation of the solution of F_{G} by conducting a numerical cross-check.

Spherical transformation to $n_{\mathrm{G}}(t)$ and Fourier transform to $N_{\mathrm{G}}(w)$

Beginning with Equation (2.5) and shown below,

$$\frac{\partial f_{\mathrm{G}}}{\partial t} = -v_r \frac{\partial f_{\mathrm{G}}}{\partial r} + \frac{1}{r^2}\frac{\partial}{\partial r}\left(r^2 \kappa \frac{\partial f_{\mathrm{G}}}{\partial r}\right) + \frac{1}{r^2}\frac{\partial}{\partial r}\left(r^2 v_r\right)\frac{\epsilon}{3}\frac{\partial f_{\mathrm{G}}}{\partial \epsilon}$$
$$+ \frac{n_e \sigma_{\mathrm{T}} c}{m_e c^2}\frac{1}{\epsilon^2}\frac{\partial}{\partial \epsilon}\left[\epsilon^4\left(f_{\mathrm{G}} + kT_e \frac{\partial f_{\mathrm{G}}}{\partial \epsilon}\right)\right] + \frac{N_0 \delta(r-r_0)\delta(\epsilon-\epsilon_0)\delta(t-t_0)}{4\pi r_0^2 \epsilon_0^2} , \tag{2.74}$$

I transform f_{G} to n_{G} by applying the integral operator $\int_0^\infty \epsilon^2 d\epsilon$ to Equation (2.74) giving,

$$\frac{\partial n_{\mathrm{G}}}{\partial t} = -\frac{1}{r^2}\frac{\partial}{\partial r}\left[r^2\left(v_r n_{\mathrm{G}} - \kappa \frac{\partial n_{\mathrm{G}}}{\partial r}\right)\right] + \frac{N_0 \delta\left(r-r_0\right)\delta\left(t-t_0\right)}{4\pi r_0^2} . \tag{2.75}$$

Now, I non-dimensionalize this equation by utilizing the same substitutions as shown earlier, which are given by,

$$v_r(\tilde{r}) = -\hat{v} c\, \tilde{r}^{-1/2} , \quad n_e(\tilde{r}) = \frac{\tilde{r}^{-3/2}}{3\,\sigma_{\mathrm{T}} R_g \hat{\kappa}} , \quad \kappa(\tilde{r}) = \hat{\kappa} R_g c\, \tilde{r}^{3/2} ,$$
$$y \equiv \frac{r_t}{r} = \frac{\hat{v}}{\hat{\kappa}\tilde{r}} , \quad \chi \equiv \frac{\epsilon}{kT_e} , \quad \Theta \equiv \frac{kT_e}{m_e c^2} , \quad q \equiv \frac{\hat{\kappa}^{3/2}}{\hat{v}^{1/2}}\frac{t\, c}{R_g} . \tag{2.76}$$

Performing these substitutions and algebra the dimensionless photon number density distribution is given by:

$$\frac{\partial n_{\mathrm{G}}}{\partial q} = y^4 \frac{\partial}{\partial y}\left[\frac{1}{y^{3/2}}(-n_{\mathrm{G}} + \frac{\partial n_{\mathrm{G}}}{\partial y})\right] - \frac{N_0 \hat{\kappa}^3 y_0^2 y^2 \delta\left(y-y_0\right)\delta\left(q-q_0\right)}{4\pi \hat{v}^3 R_{\mathrm{g}}^3} . \tag{2.77}$$

In order take the Fourier transform of this equation, the integral of the Fourier transform on the left hand side can be found by integrating by parts as shown:

$$\frac{\hat{v}^{1/2}}{\hat{\kappa}^{3/2}}\frac{R_g}{c}\int_{-\infty}^{+\infty}\frac{\partial n_{\rm G}}{\partial q}e^{i\tilde{\omega}q}dq = \frac{\hat{v}^{1/2}}{\hat{\kappa}^{3/2}}\frac{R_g}{c}\left[n_{\rm G}e^{i\tilde{\omega}q}|_{-\infty}^{\infty} - i\tilde{\omega}\int_{-\infty}^{+\infty}n_{\rm G}e^{i\tilde{\omega}q}dq\right] = -i\tilde{\omega}N_{\rm G}\ . \quad (2.78)$$

The right hand side has terms $n_{\rm G}$, $\delta\,(q-q_0)$, and the multiplied $e^{i\tilde{\omega}q}$ with a q dependence. All other terms and operators move out of the integrals. Completing the Fourier transform gives:

$$-i\tilde{\omega}N_{\rm G} = y^4\frac{\partial}{\partial y}\left[\frac{1}{y^{3/2}}(-N_{\rm G}+\frac{\partial N_{\rm G}}{\partial y})\right] - \frac{N_0\hat{\kappa}^{3/2}y_0^2y^2\delta\,(y-y_0)\,e^{i\tilde{\omega}q_0}}{4\pi\hat{v}^{5/2}R_{\rm g}^2c}\ . \quad (2.79)$$

Boundary Conditions for N_G

Given appropriate boundary conditions, $N_{\rm G}$ will have two separate solutions, one for the region inside the source term, and one for the region outside the source term. The boundary conditions utilized here are given by the photon number flux of n, $\mathfrak{F}_n$, as a function of diffusion and advection (Becker 1992):

$$\mathfrak{F}_n = \int_0^\infty \epsilon^2\mathfrak{F}_f d\epsilon = -\kappa\frac{dn}{dr} + v_r n \quad \propto \quad {\rm sec}^{-1}\ {\rm cm}^{-2} \quad (2.80)$$

.

As stated before with the $f_{\rm G}$ boundary conditions, in this model I assume that at the inner edge of the cloud, as well as the outer edge, the photon diffusion term transitions to a free-streaming condition given by,

$$-\kappa\frac{dn}{dr} = -cn \quad \text{(inner edge)}, \qquad -\kappa\frac{dn}{dr} = cn \quad \text{(outer edge)}\ . \quad (2.81)$$

Non-dimensionalizing and performing the Fourier transform gives the boundary conditions as:

$$-(\hat{v}\hat{\kappa}y)^{1/2}N'_{\text{in}} = N_{\text{in}} \;\; \text{and} \;\; N\left(y_{\text{in}}\right) = 1 \;\; \text{at} \;\; y = y_{\text{in}} \ , \tag{2.82}$$

$$(\hat{v}\hat{\kappa}y)^{1/2}N'_{\text{out}} = N_{\text{out}} \;\; \text{and} \;\; N\left(y_{\text{out}}\right) = 1 \;\; \text{at} \;\; y = y_{\text{out}} \ . \tag{2.83}$$

Global Solution of $N_{\text{G}}(\tilde{\omega})$

The global solution of N_{G} is given by:

$$N_{\text{G}} = \begin{cases} A_{\text{in}}N_{\text{in}}, & \text{for} \;\; y_{\text{in}} < y < y_0 \\ A_{\text{out}}N_{\text{out}}, & \text{for} \;\; y_0 < y < y_{\text{out}} \end{cases} \ . \tag{2.84}$$

One can solve for the constants A_{in} and A_{out} by integrating Equation (2.79) around y_0 and taking the limit,

$$\lim_{\epsilon\to 0} \int_{y_0-\epsilon}^{y_0+\epsilon} \left[0 = i\tilde{\omega}N_{\text{G}} + y^4 \frac{\partial}{\partial y}\left[\frac{1}{y^{3/2}}(-N_{\text{G}} + \frac{\partial N_{\text{G}}}{\partial y})\right] - \frac{N_0 \hat{\kappa}^{3/2} y_0^2 y^2 \delta\left(y - y_0\right) e^{i\tilde{\omega}q_0}}{4\pi\hat{v}^{5/2}R_{\text{g}}^2 c} \right] dy \ . \tag{2.85}$$

After performing the integration and algebra, the following condition is found,

$$\lim_{\epsilon\to 0} \left[\left.\frac{\partial N_{\text{G}}}{\partial y}\right|_{y=y_0+\epsilon} - \left.\frac{\partial N_{\text{G}}}{\partial y}\right|_{y=y_0-\epsilon} \right] = \frac{N_0(\hat{\kappa}y_0)^{3/2}e^{i\tilde{\omega}q_0}}{4\pi\hat{v}^{5/2}R_g^2 c} \ . \tag{2.86}$$

Utilizing this result along with the knowledge that at $y = y_0$, $A_{\text{out}}N_{\text{out}} = A_{\text{in}}N_{\text{in}}$, the resulting global solution has for its constants:

$$A_{\text{in}} = \frac{N_0(\hat{\kappa}y_0)^{3/2}e^{i\tilde{\omega}q_0}}{4\pi\hat{v}^{5/2}R_g^2 c} \left(\frac{N\left(y_0\right)_{\text{out}}}{N\left(y_0\right)_{\text{in}} N\left(y_0\right)'_{\text{out}} - N\left(y_0\right)_{\text{out}} N\left(y_0\right)'_{\text{in}}} \right) \ , \tag{2.87}$$

$$A_{\mathrm{out}} = \frac{N_0(\hat{\kappa} y_0)^{3/2} e^{i\tilde{\omega} q_0}}{4\pi \hat{v}^{5/2} R_g^2 c} \left(\frac{N\left(y_0\right)_{\mathrm{in}}}{N\left(y_0\right)_{\mathrm{in}} N\left(y_0\right)_{\mathrm{out}}' - N\left(y_0\right)_{\mathrm{out}} N\left(y_0\right)_{\mathrm{in}}'} \right) \ . \tag{2.88}$$

Computational Validation

The global solution for N_{G} can now be evaluated using Method 1 and Method 2. If the results match, then there is a high probability that the correct solution is achieved. Although this comparison cannot be done analytically, it can be solved numerically with the given boundary conditions. This has been done with high success via the Mathematica software thus providing high confidence in the solutions.

Chapter 3: Model Application to AGN 1H0707-495

3.1 Observations of AGN 1H0707-495

3.1.1 General Observations

H707 is a narrow-line Seyfert 1 (NLS1) galaxy that since 2000, has had multiple observational campaigns. It demonstrates steady UV/optical emission (Pawar et al. 2017) and has a redshift of $z = 0.04057$ (Jones et al. 2009). The black hole is expected to have a mass somewhere between $2 \times 10^6\, M_\odot$ (Zhou & Wang 2005) and $1 \times 10^8\, M_\odot$ (Leighly 2004) with an accretion rate that is at or above the Eddington limit (Tanaka et al. 2004). Its X-ray spectrum has been well-fitted in XSPEC using continuum models that commonly consist of a thermal accretion disk component such as blackbody or Comptonization, a power law, and ionized reflector components (See Figure 3.1 panel a)). The X-ray flux of the accretion disk potentially is produced up to 100s of gravitational radii away from the black hole (see for example Wilkins & Fabian 2011) which implies that the accretion disk itself is potentially as large as 1000 gravitational radii. Due to the observable excess iron Lα and iron Kα lines in observations, H707 is expected to have its iron abundance be several times the Solar composition (See Figure 3.1 panel b)). The iron lines show relativistic broadening and imply that the black hole has a very high spin parameter $a > 0.97$, where $a = J/(McR_g)$ for a black hole with mass M and angular momentum J (Fabian et al. 2009).

a)

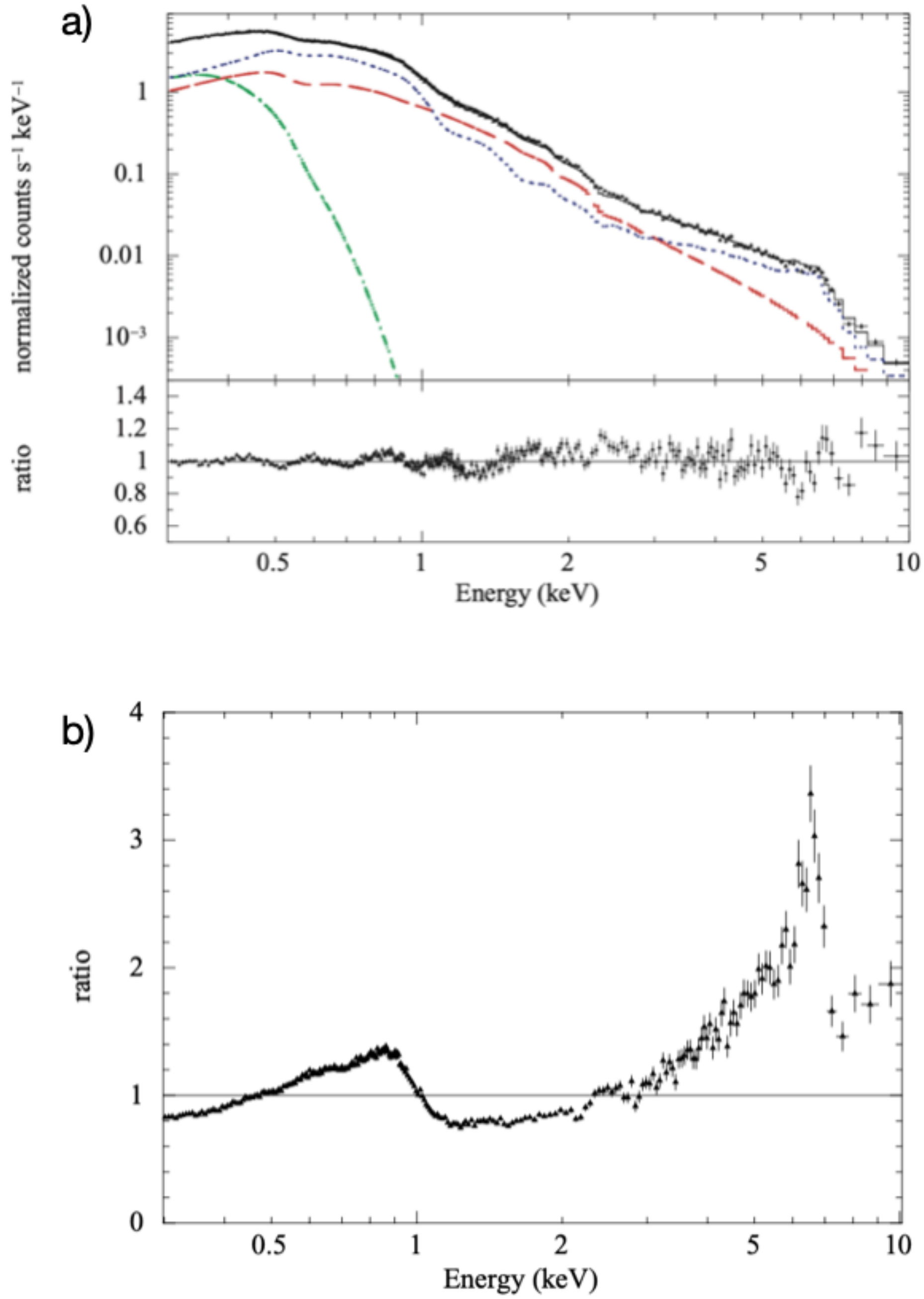

Figure 3.1: a) H707 spectral model that includes a power law (dashed red line), a blackbody (dot-dashed green), and a blurred reflection component (dotted blue). b) Ratio of H707 spectrum to a simple power law. Note the broad excesses which are theorized to correspond to Fe Kα and Lα lines. Credit: Zoghbi et al. (2010).

H707 is well known for its large, sharp drop in X-ray flux at ~ 7 keV discovered by Boller et al. (2002). It is also well known as one of the most highly variable NLS1 galaxies, varying by factors of tens within hours (Kosec et al. 2018), with higher variability seen in the power law spectrum above 1 keV (Fabian et al. 2009). Figure 3.2 shows the bright and faint states in panel a) and the corresponding highly variable light curves in panel b), and the PSD plot in four different energy bands in panel c).

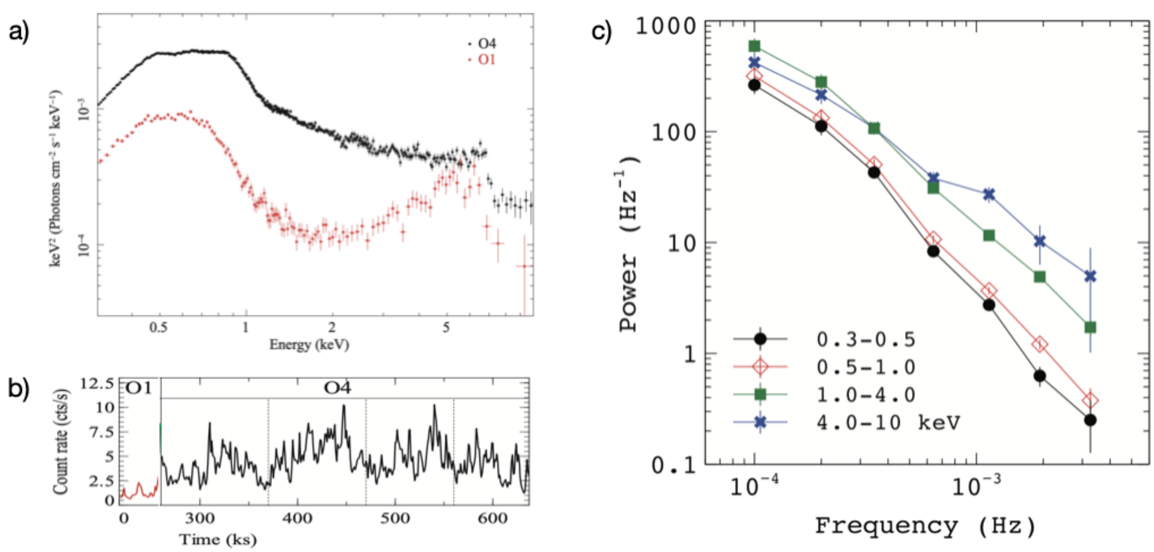

Figure 3.2: a) Unfolded spectrum of H707 in two different 2008 XMM observations; O1 is faint and O4 is bright. b) Variable light curves of H707 in two different observations. Credit: Zoghbi et al. (2010). c) PSD in different energy bands. Credit: Zoghbi et al. (2011).

3.1.2 Time Lags

As previously noted in Section 1.4.2, H707's variability data displays both hard and soft time lags as a function of Fourier frequency (See Figure 3.3 panel a)) when analyzed between the $0.3-1$ keV and the $1-4$ keV energy bands. The time lags comprise an interesting patten, with the source displaying hard lags of magnitude ~ 100 s for Fourier frequencies $\nu_F \lesssim 10^{-3}$ Hz and soft lags on the order of ~ -10 s for Fourier frequencies $\nu_F \gtrsim 10^{-3}$ Hz. When the lags are analyzed as a function of energy with respect to two different Fourier frequency groupings (lower frequency / hard lags and higher frequency / soft lags; see Figure 3.3 panel b)), the lower / hard lag frequencies within the $0.3-0.9$ keV energy range show a nearly constant zero lag between all of the energies.

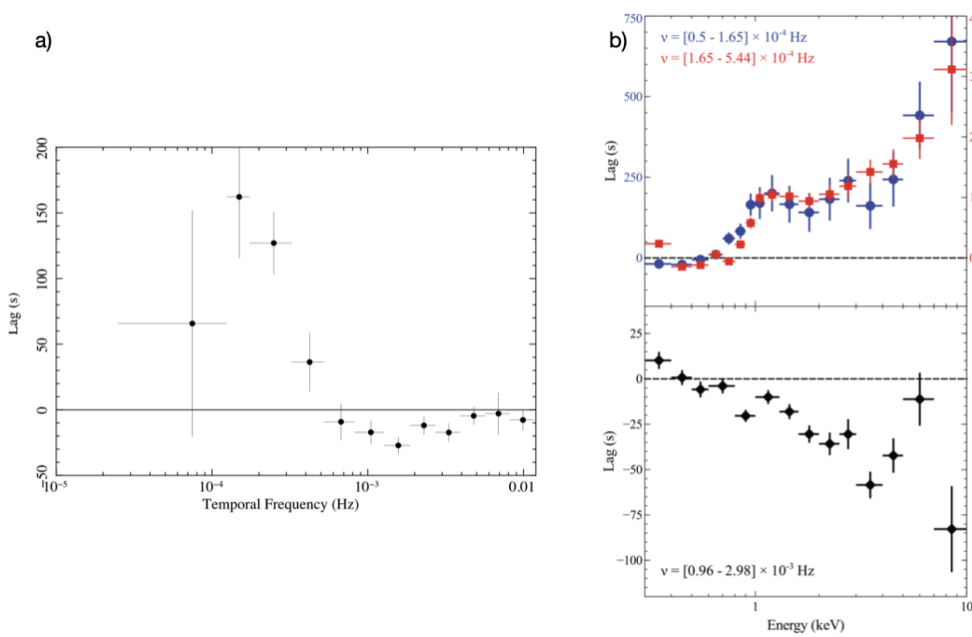

Figure 3.3: a) H707 time lags vs. Fourier frequency as determined between the 0.3-1 keV and 1-4 keV energy bands. Credit: Fabian et al. (2009). b) H707 time lags vs. energy spectrum computed for energy band bins referenced to the 0.3-0.8 keV bin. Credit: Kara et al. (2013).

However, at an energy of $\sim$ 0.9-1 keV, the hard lags increase rapidly to 100s of second. The lags then mostly level off and then increase rapidly again around 6 keV until the last values at 10 keV. In the higher, soft lag frequencies, $\nu_F \gtrsim 10^{-3} Hz$, the lags appear to increase monotonically with energy, but in the opposite direction of the lower hard lag frequencies (from hard to soft), with the exception of precipitous drops at ~ 1 keV and 6 keV, that then rebound quickly as the energies increase (Kara et al. 2013). It is important to note that 1 keV and 6 keV are at the energy of the iron $L\alpha$ and $K\alpha$ lines.

3.2 Model Parameters

As stated in section 2.4, in order to compute X-ray time lags I initially specify five parameters: (1) the black hole mass, M; (2) the dimensionless accretion rate, $\dot{m} = \dot{M}/\dot{M}_{\rm E}$; (3) the dimensionless inner radius, $\tilde{r}_{\rm in} = r_{\rm in}/R_g$; (4) the dimensionless outer radius, $\tilde{r}_{\rm out} = r_{\rm out}/R_g$; and (5) the dimensionless velocity parameter, $\hat{v}$.

3.2.1 Mass and Accretion Rate

Parameters (1) and (2) are quickly established based on previous research. For the mass value, I utilize the lower limit provided by Zhou & Wang (2005) of $M = 2 \times 10^6 \, M_\odot$. For the accretion rate I use a value just slightly above the Eddington limit of $\dot{m} = 1.1$ in line with Tanaka et al (2004)'s estimate which was also based on the same mass value.

3.2.2 Inner Radius

For the third parameter, the inner radius, based on the inner boundary condition being a free-streaming boundary, I define the inner edge of the spherical region, at radius $r = r_{\rm in}$, as the radius of the innermost stable prograde circular orbit, $r_{\rm ISCO}$, so that

$$r_{\rm in} = r_{\rm ISCO} \ . \tag{3.1}$$

The value of $r_{\rm ISCO}$ is computed using (Shapiro & Teukolsky 1983)

$$
\begin{aligned}
r_{\mathrm{ISCO}} &= R_g \left[3 + Z_2 - \sqrt{(3 - Z_1)(3 + Z_1 + 2Z_2)}\right] \ , \\
Z_1 &\equiv 1 + \left(1 - a^2\right)^{1/3} \left[(1 + a)^{1/3} + (1 - a)^{1/3}\right] \ , \\
Z_2 &\equiv \left(3a^2 + Z_1^2\right)^{1/2} \ .
\end{aligned}
\tag{3.2}
$$

In the case of a non-rotating black hole, $a \to 0$, and Equation (3.2) reduces to the Schwarzschild result, $r_{\mathrm{ISCO}} = 6R_g$. Note that the radius of the event horizon for prograde orbits, r_H, is given by

$$
r_H = R_g \left(1 + \sqrt{1 - a^2}\right) \ , \tag{3.3}
$$

which reduces to $r_H = 2R_g$ in the Schwarzschild limit. In accordance with Fabian et al. (2009), I set the spin parameter for the black hole at $a = 0.98$, which gives the inner edge of the spherical region to be located at radius $r_{\mathrm{in}} = r_{\mathrm{ISCO}} = 1.61\,R_g$ (Equation (3.2)), and the event horizon at $r_H = 1.20\,R_g$ (Equation (3.3)).

3.2.3 Outer Boundary

For the fourth parameter, the outer edge of the spherical region, I model a relatively extended coronal region with a boundary at $r_{\mathrm{out}} = 120\,R_g$. Although this is larger than the $\sim 35\,R_g$ extended coronal region discussed by Fabian et al. (2012) and their research group, it is noted as expected in the same class of models as they used to replicate and model the observed time lags, which was taken from Arevalo & Uttley (2006). Additionally, this outer boundary range is in line with Miller et al. (2010), who cite a radius of 100 R_g for their corona. Further discussion on this is found in Section 3.4.1.

3.2.4 Radial Velocity

Finally, to set the fifth parameter, the dimensionless velocity parameter, $\hat{v}$, as discussed in Section 2.2.2 within the quasi-spherical coronal region the radial velocity, v_r follows the free-fall profile $v_r \propto r^{-1/2}$. As shown in Equation (2.6), my model allows for a varying of the velocity parameter between free-fall and any value below free-fall. In this example, since I am assuming an extended coronal region with low optical depth all the way down to the inner regions near the black hole, there is very limited material to counteract gravity and so I set the dimensionless velocity parameter to $\hat{v} = \sqrt{2}$, which corresponds to exact free-fall.

3.2.5 Additional Calculated Parameters

With the five parameters now set, solving Equation (2.21) yields for the dimensionless diffusion parameter $\hat{\kappa} = 0.429$. The values of the inner and outer dimensionless location parameters, $y_{\rm in}$ and $y_{\rm out}$, can be computed using Equation (2.41), which yield $y_{\rm in} = 2.045$ and $y_{\rm out} = 0.028$. Note that according to Equation (2.21), the trapping radius is located at $r_t = 3.3R_g$ for $\dot{m} = 1.1$.

The electron scattering optical depth measured inward from the outer edge of the spherical region, $\tau(\tilde{r})$, is computed using Equation (2.12), and plotted in Figure 3.4. The optical depth at radius $r = 1.86\,R_g$ is unity, which is in agreement with the relativistically blurred iron line emission from the inner parts of the accretion disk being able to be resolved spectroscopically (e.g., Wilkins et al. 2014). The optical depth at the inner boundary, $r = r_{\rm ISCO} = 1.61R_g$, is $\tau = 1.082$ and decreases monotonically out to $\tau = 0$ at $r = 120\,R_g$.

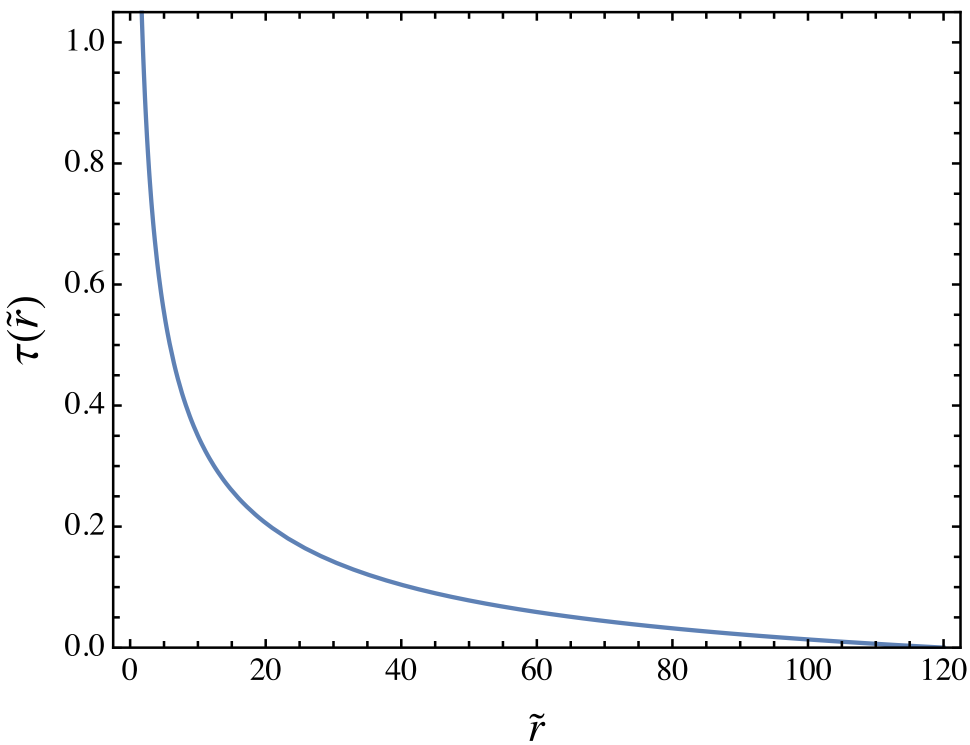

Figure 3.4: The electron scattering optical depth, $\tau(\tilde{r})$, measured inward from the outer edge of the spherical region, plotted as a function of the dimensionless radius $\tilde{r}$, computed using Equation (2.12).

For completeness, although not needed for the time lag calculations, the luminosity of H707 is also calculated utilizing values attained from previous research. Assuming isotropic emission at the source, the X-ray luminosity, L_X, is computed using

$$L_X = 4\pi D^2 F_X \ , \tag{3.4}$$

where $F_X = 1.44 \times 10^{-10}$ erg cm^{-2} s^{-1} is the observed X-ray flux in the energy range 0.3-4 keV, calculated using data from Zoghbi et al. (2010) and $D = 181$ Mpc is the luminosity distance (Sani et al. 2010). The X-ray luminosity obtained using Equation (3.4) is therefore $L_X = 5.63 \times 10^{44}$ erg s^{-1} which corresponds with other estimates.

3.3 Simulated Time Lags

3.3.1 Eigenvalue Computation

Since the eigenvalues, λ_n, in my calculation are functions of the Fourier frequency, ν_F, a sample of discrete Fourier frequencies must be selected and the time lags evaluated at those frequencies. Note that a continuous range of Fourier frequencies is not required in this model, since I do not need to perform the inverse Fourier transformation. Instead, the required time lags are computed directly from knowledge of the Fourier transform itself.

In applying the model to H707, I select values for the vector of Fourier frequencies, ν_F (in Hz), that are comparable to the values shown by Fabian et al. (2009) and Zoghbi et al. (2010) in their plots of the time lags. The values adopted here are: $\nu_F = 7.94 \times 10^{-5}, 1.58 \times 10^{-4}, 2.51 \times 10^{-4}, 3.98 \times 10^{-4}, 6.31 \times 10^{-4}, 1.00 \times 10^{-3}, 1.58 \times 10^{-3}, 2.24 \times 10^{-3}, 3.31 \times 10^{-3}, 5.01 \times 10^{-3}, 7.08 \times 10^{-3}, 1.00 \times 10^{-2}$. The corresponding dimensionless Fourier frequency values, $\tilde{\omega}$, computed using Equation (2.33) are: $\tilde{\omega} = 0.02$, 0.04, 0.06, 0.10, 0.16, 0.26, 0.42, 0.59, 0.87, 1.32, 1.86, 2.62. Note that the value of the photon injection number N_0 has no affect on the time lags and also that the injection time can be set to $t_0 = q_0 = 0$ without loss of generality.

The sequences of complex eigenvalues, λ_n, obtained for each discrete value of the Fourier frequency $\tilde{\omega}$ adopted here are plotted in Figure 3.5, with the value of $\tilde{\omega}$ increasing from bottom to top. The eigenvalues are indicated by the points, and the lines are added to clarify the eigenvalue sequence for each frequency. It should be noted that in the limit $\tilde{\omega} \to 0$, the eigenvalues approach the quiescent case and are no longer imaginary. Using alternate boundary conditions, such as that explored by Colpi (1988) and Titarchuk et al (1997) (See Section 2.3.3), the eigenvalues are given by $\lambda_n = 2n + 5; n = 0, 1, 2, ...$ The quiescent case is further explored in Chapter 4.

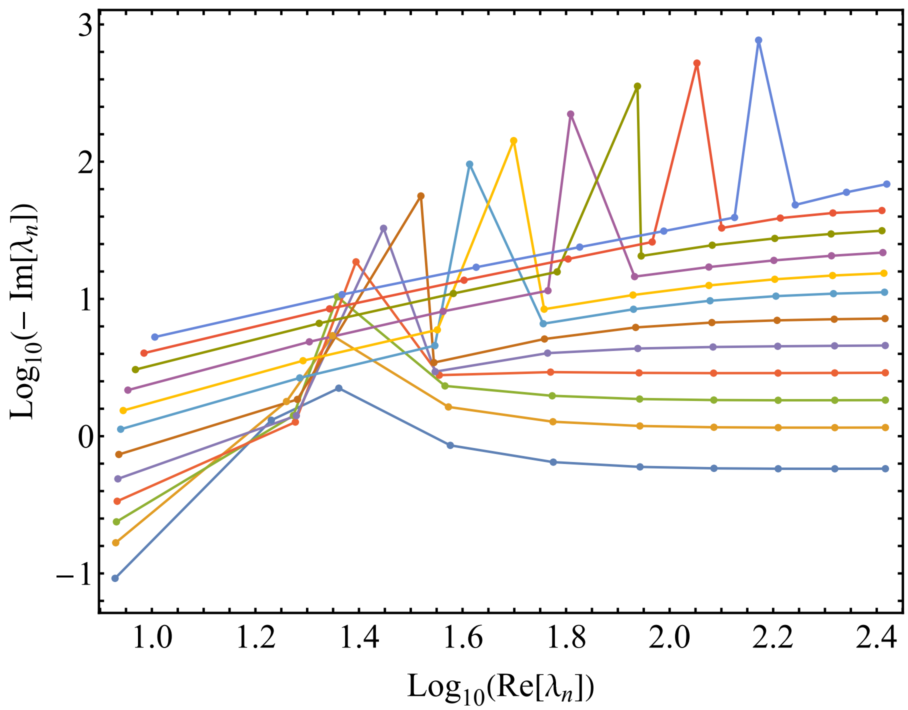

Figure 3.5: Plot of the first 10 complex eigenvalues, λ_n, for each Fourier frequency $\tilde{\omega}$, with the log of the real part on the horizontal axis and the log of the negative of the imaginary part on the vertical axis. Each color sequence corresponds to a different Fourier frequency. The eigenvalues are indicated by the points, and the lines are added for clarity. The eigenvalue index n increases from left to right, and the dimensionless Fourier frequency $\tilde{\omega}$ increases from bottom to top, through the vector of 12 values for $\tilde{\omega}$.

3.3.2 Fit Parameters

As noted in Section 2.4, after determining the eigenvalues, the computation of the simulated time lags, δt, using my theoretical model, requires specification of three more parameter sets: (1) the electron temperature $\Theta = kT_e/(m_e c^2)$, (2) the hard and soft channel energies, ϵ_h and ϵ_s, respectively, and (3) the source parameters, which includes the photon injection energy ϵ_0; and the the injection radius r_0.

3.3.3 Electron Temperature

For the first parameter, Θ, to achieve the best fit, the value adopted for the dimensionless electron temperature is $\Theta = 0.05$, so that $kT_e \approx 25\,\mathrm{keV}$. This value is in line with expected coronal temperatures which are expected to be much hotter ($kT_e > 10$ keV) than the underlying accretion disk expected values of tens to hundreds of eV.

3.3.4 Time Lag Energy Bands

The second parameter set must be approximated since the observational time lags provided by Fabian et al. (2009) and others use entire energy bands for the two channels. In this example, the bands are given by $\epsilon_s = 0.3 - 1\,\mathrm{keV}$ for the soft energy band and $\epsilon_h = 1 - 4\,\mathrm{keV}$ for the hard energy band. My model is not able to accommodate an energy range for the soft and hard bands, and instead exact values are needed for ϵ_s and ϵ_h. Qualitatively, one notes that the Fourier frequency generation of the lags utilizes the composite Fourier signal of all of the energy signals in each respective band. If the variability throughout the band is approximately equal or if the variability is dominated by a certain discrete energy value, the variability of each signal can then be approximated by a single energy value within the band. As noted by Figure 3.3 panel b), this is the case for the bands in question where the variability in the soft band is dominated at the lower edge of the band and the variability in the hard band is on average . To achieve the best fit, I set the hard and soft channel energies to the values $\epsilon_s = 0.33\,\mathrm{keV}$ and $\epsilon_h = 1.76\,\mathrm{keV}$.

3.3.5 Injection Parameters

For the third and final source parameter set, the best fit values are found using $\epsilon_0 = 0.89\,\mathrm{keV}$ for the injection energy and $r_0 = 16R_g$ for the injection radius. This value is noted to be a value in the vicinity that dissects where the energy lags are not appearing and then begin to rapidly occur (See Figure 3.3) as well as the peak of the broadened and skewed energy of the iron L-line that Fabian et al. (2009) reported for H707 (See Figure 3.1). The value of the injection radius is toward the inner regions of the black hole and in line with estimates that predict most of the X-ray production occurs near the black hole.

3.3.6 Converging Model Fit

The convergence of the results obtained for the time lags as a function of the value of the maximum index, $N_{\max}$, appearing in the sum in Equation (2.65), has been analyzed to ensure accuracy in the model. I find that setting $N_{\max} = 5$ is sufficient to ensure convergence to a relative error of $\sim 1\%$. To guarantee confidence in the results, I use the first 10 eigenvalues and eigenfunctions in computing the time lags for each value of the Fourier frequency ω to ensure convergence of my results. The resulting time lag distribution, δt, computed using Equation (1.20), is plotted as a function of the Fourier frequency $\nu_F = \omega/(2\pi)$ using the green solid curve in Figure 3.6, and compared with the observational data for H707 reported by Fabian et al. (2009) and Zoghbi et al. (2010). The hard lags (positive values), where the hard signal is detected after the soft signal for the same Fourier frequency, occur in the lower Fourier frequency components of the varying energy signals. These lags peak at a relatively large value of approximately 150 seconds and then rapidly descend toward a transition frequency. Conversely, the soft lags (negative values), which steadily appear at values on the order of 10s of seconds, occur in the higher Fourier frequency components of the varying energy signals. Note the good agreement between the theoretical model and the time-lag data from Fabian et al. (2009) and Zoghbi et al. (2010), including the change in sign of δt from positive below Fourier frequency $\sim 5 \times 10^{-4}\,\mathrm{Hz}$ to negative at higher frequencies.

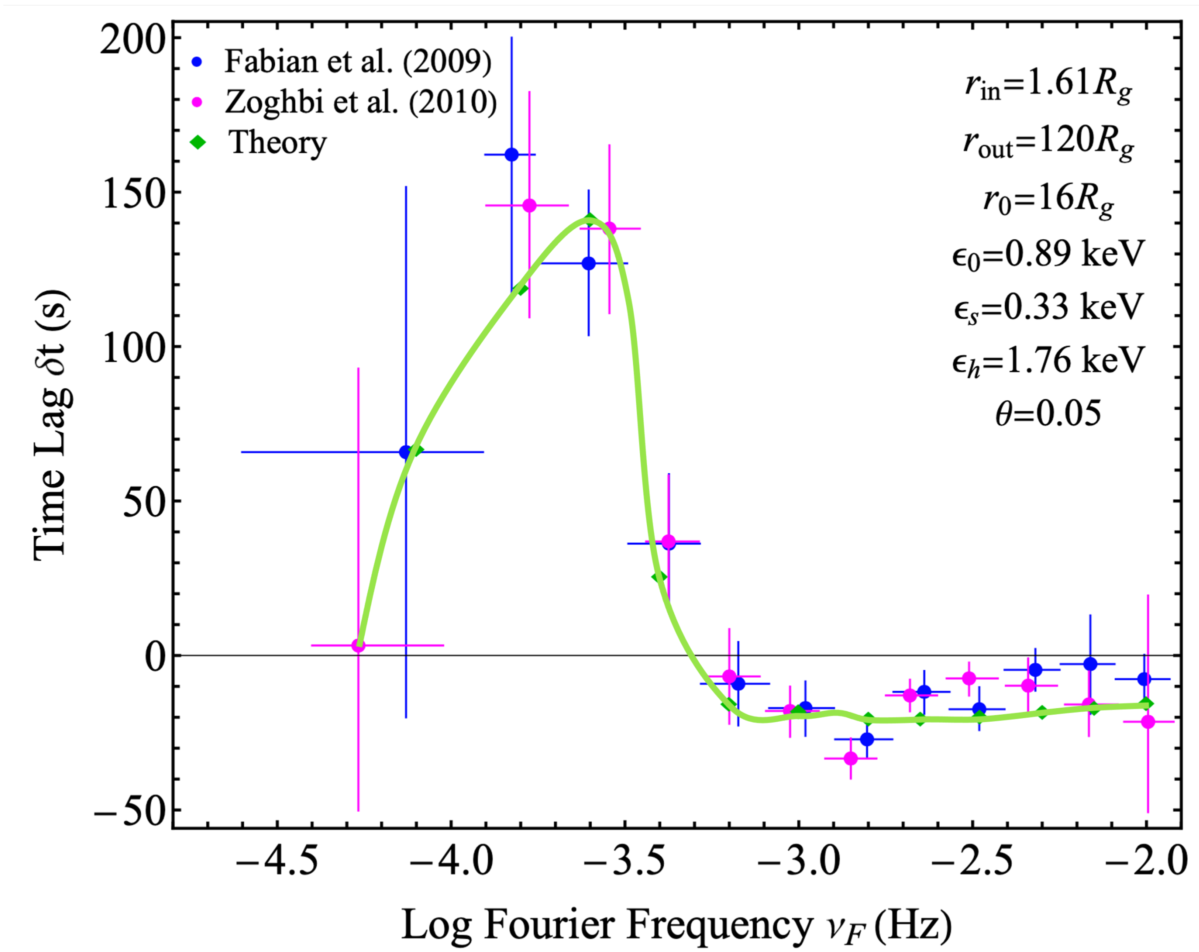

Figure 3.6: Time lag distribution δt plotted as a function of the Fourier frequency, $\nu_F = \omega/(2\pi)$ (green diamonds and line). A positive value for δt indicates a hard lag and a negative value indicates a soft lag. Observational data are taken from Fabian et al. (2009; blue dots) and Zoghbi et al. (2010; purple dots).

One can also explore the PSD of the two energy bands. Recall in Chapter 1, that the PSD is given by,

$$\text{PSD} = |\tilde{\mathscr{F}}_{\epsilon}(\epsilon, \omega)|^2 \ . \tag{3.5}$$

The results that Zoghbi et al. (2011) obtained for the PSD for H707 are shown in Figure 3.2 panel b). It is interesting to compare the PSD predicted by my theory with the observational data reported by Zoghbi et al. (2011). This comparison is carried out in Figure 3.7 using two specific values for the photon energy, $\epsilon = 0.4$ keV and $\epsilon = 2$ keV. The good agreement between the theory and the observations adds further credence to the validity of my theory.

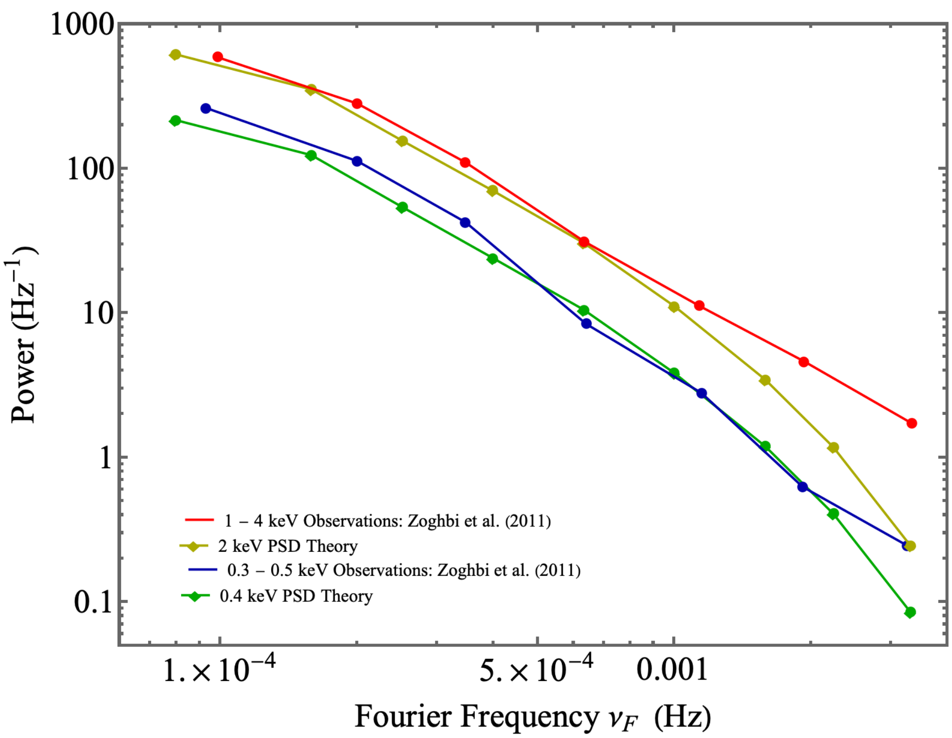

Figure 3.7: Comparison of H707 PSD plot for observation and theory for two energy bands

3.4 Discussion

3.4.1 The Critical Frequency

The behavior of H707's time lags δt as a function of the Fourier frequency, $\nu_F = \omega/(2\pi)$, display unusual behavior, especially if viewed in relation to the lags noted in Chapter 1 for the BHB Cyg X-1 and shown in Figure 1.17. The most peculiar aspect of the lags is the existence of the aforementioned transition point and the fact that the lags contain both hard and soft lags. In order to clearly analyze and discuss this behavior, the transition point implies the need to define a new variable, the critical frequency, ν_c, which for this source is located at $\sim 5 \times 10^{-4}$ Hz.

The critical frequency has been shown to exist in many other AGN as shown by De Marco et al. (2013) and Mallick et al. (2021). Mallick's plot of similar "low-mass" AGN to H707 is shown in Figure 3.8 panel a). In panel b) I have created a table and plot with a best linear fit line of the 7 AGN showing their estimated mass versus critical frequency. Note that H707 would basically follow the trend where more massive AGN have lower critical frequencies. Mallick et al. (2021) identified with a black arrow a similar value to the critical frequency using the lowest soft lag frequency instead of the transition point (See Figure 3.8 panel a)). They also separately overlaid DeMarco's data, which covered a much broader range of masses. In the Mallick plot the trend showed a relation between mass and frequency whereby with increasing mass one finds decreasing values of the soft lag frequency similar to DeMarco's research. Both of these plotted results provide observational evidence that in general, the soft lags lowest frequency are not necessarily dependent on a certain specific value of Fourier frequency, but instead occur due to a scaling relationship that is dependent on the mass of the black hole. This aspect of the shifting of the critical frequency naturally occurs in my model as one notes the relationship of my dimensionless frequency given by Equation (2.33), and given again here,

$$\tilde{\omega} \equiv \frac{\hat{v}^{1/2}}{\hat{\kappa}^{3/2}} \frac{R_g}{c} \, \omega \ . \tag{3.6}$$

As can be seen, remembering that $R_g = GM/c^2$, for a given dimensionless frequency, if the mass of the black hole is increased, the frequency decreases in agreement with observations.

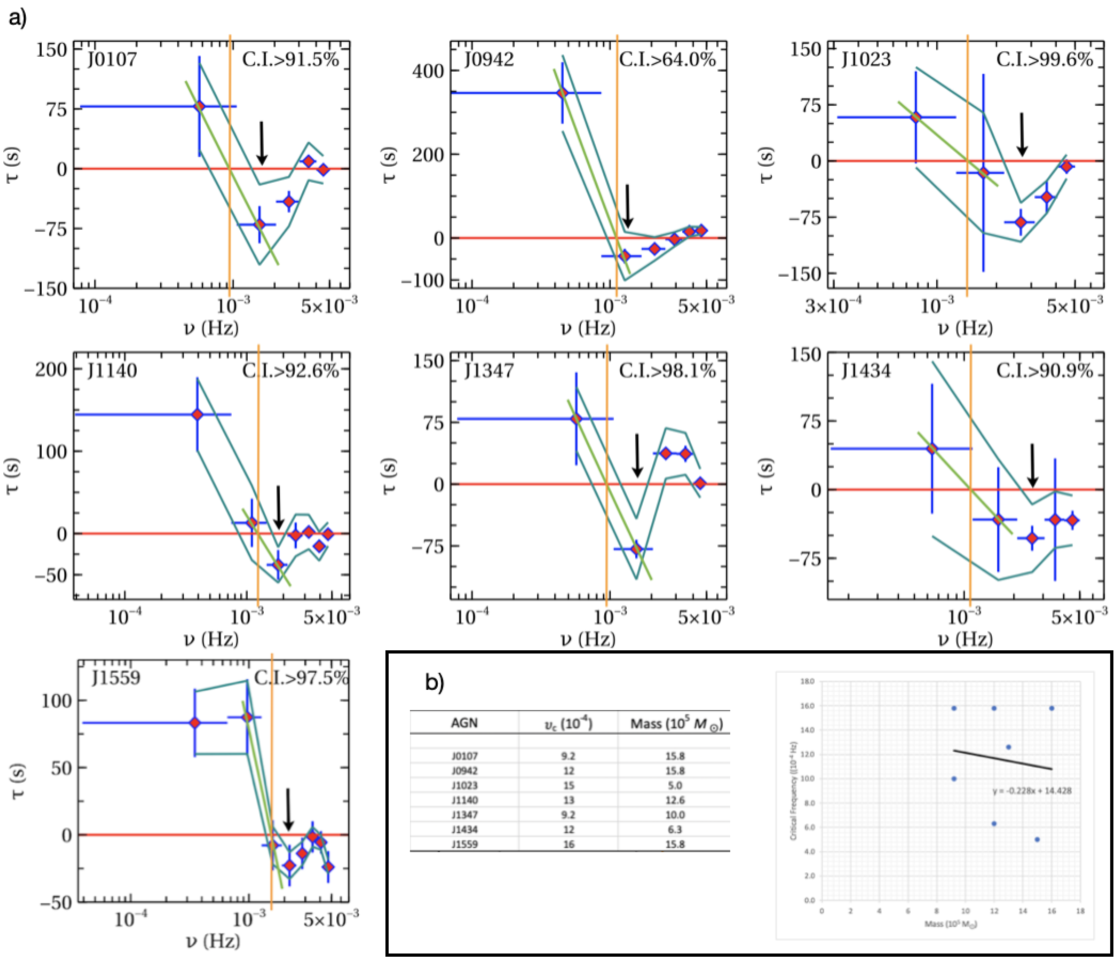

AGN	υ_c (10^{-4})	Mass (10^5 $M_\odot$)
J0107	9.2	15.8
J0942	12	15.8
J1023	15	5.0
J1140	13	12.6
J1347	9.2	10.0
J1434	12	6.3
J1559	16	15.8

Figure 3.8: a) Plots of seven "low-mass" AGN time lag plots. The yellow and green lines have been added to show the critical frequency value. Credit: Mallick et al. (2021). b) A table showing the critical frequency versus mass for each of the seven plots as well as a plot of the data that shows the best-fit linear trend line.

3.4.2 Physical Interpretation

The complex behavior of the time lags, δt, as a function of Fourier frequency stems from the fact that the energy of the injected iron L-line emission, $\epsilon_0 = 0.89\,\mathrm{keV}$, lies between the soft and hard detector band energy ranges used to compute the time lags. The existence of the critical frequency implies that there are competing physical processes occurring where one dominates or only occurs at lower Fourier frequencies and one dominates or only occurs at higher Fourier frequencies. In an attempt to better understand the cause of the time lags, Miller et al. (2010) reviewed different energy bands (See Figure 3.9). They noted that the same critical frequency occurs between their defined hard band (4-7.5 keV) and soft band (0.3-1 keV) and their defined medium band (1-4 keV; which aligns with my and Fabian's hard band) and soft band. Their hard/soft plot in the center panel of Figure 3.9 shows larger hard lags at lower frequencies than the medium/soft plot in the left panel. Their plot of lags between their hard/medium bands in the right panel of Figure 3.9 does not demonstrate any defined lags above 3×10^{-4}, but does show hard lags in the lower Fourier frequencies below that value. These results appear to correlate with Figure 3.3 panel b) and demonstrate that there are no lags in Fourier frequency variability in their hard band as compared to their medium band at Fourier frequencies above the critical frequency (i.e. the high frequency variability occurs at the same time in energies above 1 keV) and that below the critical frequency, the variability in each Fourier frequency takes time to propagate to higher energies above 1 keV. These results help to shed light on the cause of the time lags as well as the change in sign at the critical frequency.

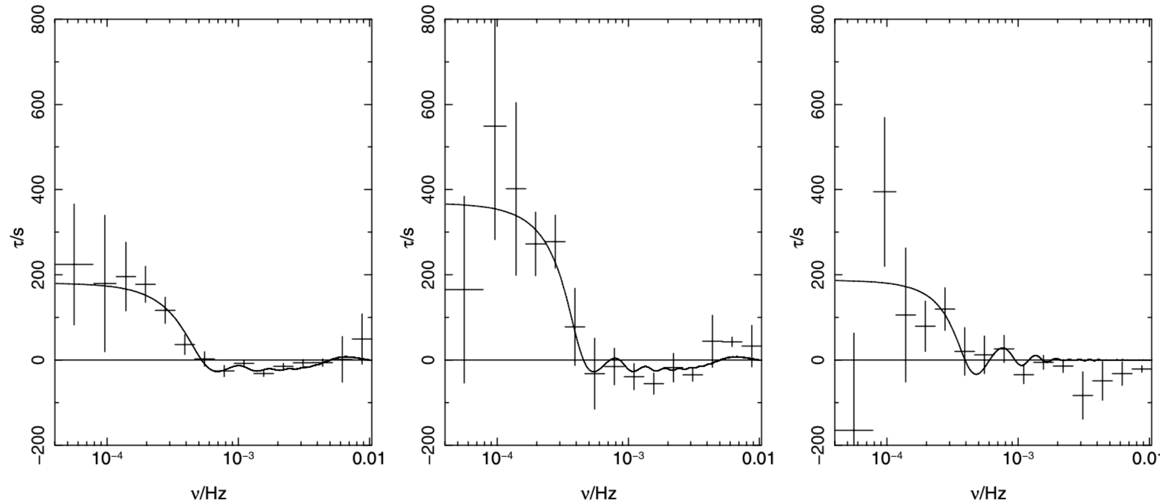

Figure 3.9: Three plots of time lags versus Fourier frequency for H707. Left panel: 0.3-1 keV versus 1-4 keV. Center panel: 0.3 keV versus 4-7.5 keV. Right panel: 1-4 keV versus 4-7.5 keV. Credit: Miller et al. (2010)

The cause of time lags differing in sign above and below the critical frequency has to do with the time scale of processes that occur due to Comptonization (see Figure 3.10). Soft time lags, which occur at high Fourier frequency, for $\nu \gtrsim \nu_c$, are due to First-order energy gain (shifting) which occurs at short time scales. There is no change in the soft lags time scale as the energy increases with respect to the soft band due to the nature of this rapid energization. Hard time lags, for $\nu \lesssim \nu_c$, occur at low Fourier frequency due to second-order energy gain (broadening) which takes longer. The continued increase in hard lag time scale with increased energy noted by Miller in Figure 3.9 is expected in accordance with Comptonization that occurs since for increasing photon energy, it takes longer for the same Fourier frequencies that occur below the critical frequency.

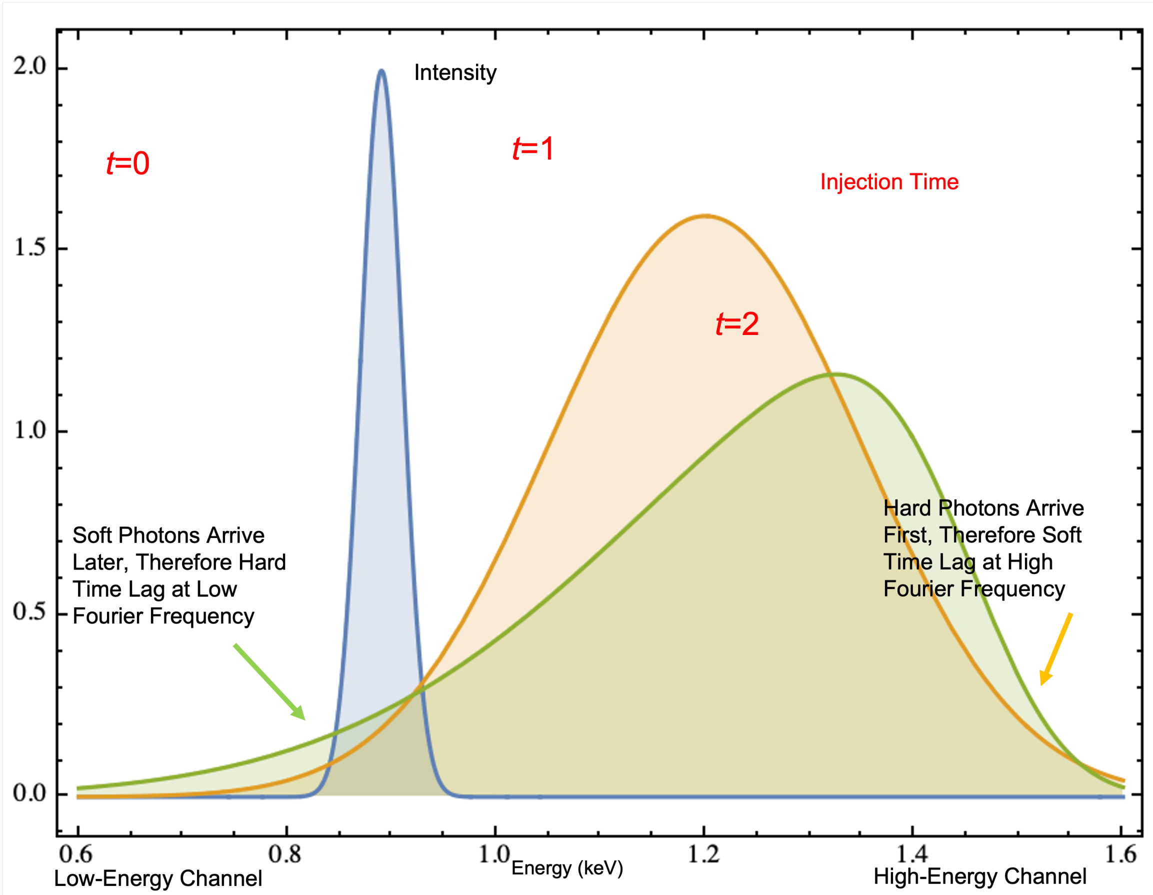

Figure 3.10: Pictorial representation of the physical interpretation for the hard and soft lags. Credit: Becker (2021).

Chapter 4: Quiescent Model

4.1 Overview

As noted in Chapter 1, there are many aspects to studying and adequately understanding the underlying physics surrounding black holes. A key aspect of this is not only investigating the observed timing behavior, but also the observed spectrum. In this chapter, I develop the steady-state, or quiescent, transport equation using the same model equation and terms in order to demonstrate that components of the observed spectrum can be generated by this same coronal model. It is important to emphasize that the quiescent spectrum does not contribute to the time lags, since as discussed in Section 1.4, "An Introduction to X-ray Fourier Time Lags", steady-state light curves do not generate phase lags and therefore do not generate time lags. Further to this point, as discussed in that section, the emission from a given source can be viewed as a superposition of continual steady-state emission, combined with episodic bursts or flashes, which produce the time-dependent phenomenon. Whereas in Chapter 2 and 3 the focus was on the episodic portion of the emission, in the next two chapters the focus is on the steady-state portion of the emission. As noted in Chapters 1 and 3, the black hole spectra are most likely formed (i.e. comprised) by numerous radiative processes to include both thermal and non-thermal. This is evidenced by model fits that are able to recreate the observed spectra. In my model, after I demonstrate the development of the quiescent solution, I will demonstrate that components of the observed spectrum can be generated by the same model. This spectra is generated by the injection of seed (or source) photons from the cooler accretion disk near the central black hole into the relatively hot, quasi-spherical surrounding coronal region where they undergo thermal and bulk Comptonization.

4.2 Transport Equation

The transport equation of the steady-state model is very similar to the time-dependent one with two key exceptions. First, there is no time dependency and second, the instantaneous source injection term N_0 is modified now to $\dot{N}_0$ to account for the continuous injection of photons per unit time in the steady-state model. Hence, the source term is now given by,

$$\frac{\dot{N}_0 \delta(r - r_0) \delta(\epsilon - \epsilon_0)}{4\pi r_0^2 \epsilon_0^2} \tag{4.1}$$

Beginning with Equation 2.5 and noting that f_G is now the steady-state Greens function, the transport equation for the quiescent case is now given by:

$$\begin{aligned}\frac{\partial f_\mathrm{G}}{\partial t} = 0 = -v_r \frac{\partial f_\mathrm{G}}{\partial r} + \frac{1}{r^2}\frac{\partial}{\partial r}\left(r^2 \kappa \frac{\partial f_\mathrm{G}}{\partial r}\right) + \frac{1}{r^2}\frac{\partial}{\partial r}\left(r^2 v_r\right)\frac{\epsilon}{3}\frac{\partial f_\mathrm{G}}{\partial \epsilon} \\ + \frac{n_e \sigma_\mathrm{T} c}{m_e c^2}\frac{1}{\epsilon^2}\frac{\partial}{\partial \epsilon}\left[\epsilon^4 \left(f_\mathrm{G} + kT_e \frac{\partial f_\mathrm{G}}{\partial \epsilon}\right)\right] + \frac{\dot{N}_0 \delta(r - r_0)\delta(\epsilon - \epsilon_0)}{4\pi r_0^2 \epsilon_0^2} \ ,\end{aligned} \tag{4.2}$$

I can now non-dimensionalize this equation by utilizing the same substitutions as made in the time-dependent case (see Section 2.2) which are given by,

$$\begin{aligned} v_r(\tilde{r}) = -\hat{v} c\, \tilde{r}^{-1/2} \ , \quad n_e(\tilde{r}) = \frac{\tilde{r}^{-3/2}}{3\, \sigma_\mathrm{T} R_g \hat{\kappa}} \ , \quad \kappa(\tilde{r}) = \hat{\kappa} R_g c\, \tilde{r}^{3/2} \ , \\ y \equiv \frac{r_t}{r} = \frac{\hat{v}}{\hat{\kappa}\tilde{r}} \ , \quad \chi \equiv \frac{\epsilon}{kT_e} \ , \quad \Theta \equiv \frac{kT_e}{m_e c^2} \ , \end{aligned} \tag{4.3}$$

where $R_g = GM/c^2$, $\tilde{r} \equiv r/R_g$, and $r_t \equiv (3\dot{M}\sigma_\mathrm{T})/(4\pi m_p c)$. Making these substitutions and performing algebra, the non-dimensional quiescent transport equation is now given by,

$$0 = \frac{\Theta}{3\hat{\kappa}\hat{v}} \frac{y^{\frac{3}{2}}}{\chi^2} \frac{\partial}{\partial \chi} \left[\chi^4 \left(f_{\rm G} + \frac{\partial f_{\rm G}}{\partial \chi} \right) \right] + y^4 \frac{\partial}{\partial y} \left(y^{-3/2} \frac{\partial f_{\rm G}}{\partial y} \right) - y^{5/2} \frac{\partial f_{\rm G}}{\partial y}$$

$$- \frac{y^{3/2}\chi}{2} \frac{\partial f_{\rm G}}{\partial \chi} - \frac{\dot{N}_0 y_0^2 \hat{\kappa}^3 y^2 \delta(y - y_0) \delta(\chi - \chi_0)}{4\pi \chi_0^2 R_g^3 (kT_e)^3 \hat{v}^3} , \tag{4.4}$$

where $f_{\rm G}(y, y_0, \chi, \chi_0)$ denotes the steady-state Green's function, which is the response to the continual injection of $\dot{N}_0$ photons of dimensionless energy χ_0 per rate of time from a source at dimensionless radius y_0.

4.3 Separation of Functions

Similar to the time-dependent case, the next step in solving for $f_{\rm G}$ is to note that for certain values, Equation (4.4) can be separated. As in the time-dependent case, due to the delta functions in the source term, when $\chi \neq \chi_0$ the source term vanishes and the transport equation can be solved by writing

$$f_\lambda(y, \chi) = g(y)\, h(\chi) \tag{4.5}$$

where λ denotes the separation constant and $g(y)$ and $h(\chi)$ denote the spatial and energy separation functions respectively. For $\chi \neq \chi_0$, substituting Equation (4.5) into Equation (4.4) and rearranging terms gives,

$$\frac{y}{g} \frac{dg}{dy} - \frac{y^{5/2}}{g} \frac{d}{dy} \left(y^{-3/2} \frac{dg}{dy} \right) = \frac{\Theta}{3\hat{v}\hat{\kappa}} \frac{1}{\chi^2 h} \frac{d}{d\chi} \left[\chi^4 \left(h + \frac{dh}{d\chi} \right) \right] - \frac{\chi}{2h} \frac{dh}{d\chi} = \frac{\lambda}{2} \tag{4.6}$$

Since the separation constant λ is independent of the coordinates y and χ, it follows that I can obtain two distinct ordinary differential equations satisfied by the functions $g(y)$ and $h(\chi)$, given respectively by

$$y\frac{d^2g}{dy^2} - \left(\frac{3}{2} + y\right)\frac{dg}{dy} + \frac{\lambda}{2}\,g = 0\ , \tag{4.7}$$

and

$$\frac{1}{\chi^2}\frac{d}{d\chi}\left[\chi^4\left(h + \frac{dh}{d\chi}\right)\right] - \delta\chi\frac{dh}{d\chi} - \delta\lambda h = 0\ . \tag{4.8}$$

where

$$\delta \equiv \frac{3\hat{v}\hat{\kappa}}{2\Theta}\ . \tag{4.9}$$

4.4 Solutions of Seperated Functions

Unlike the time-dependent case, both of the separated differential equations are solvable analytically. The solution to the spatial equation is shown below for the finite inner and outer free-streaming boundary conditions. As in the time-dependent case, alternative boundary conditions have also been solved for and are discussed in Appendix A. The energy equation and its boundary conditions are identical to the time-dependent case and the final solution is once again shown below for completeness.

4.4.1 Spatial Equation

The spatial equation is of the form of Kummer's equation and its complete global solution is given by,

$$g(y) = AM\Big(\frac{-\lambda}{2}, \frac{-3}{2}, y\Big) + BU\Big(\frac{-\lambda}{2}, \frac{-3}{2}, y\Big) \tag{4.10}$$

where $M(a, b, z)$ and $U(a, b, z)$ are confluent hypergeometric functions, A and B are arbitrary constants, and $b \neq -n$ with n being a positive integer (e.g., Abramowitz & Stegun 1964). The constants can be solved by utilizing the same boundary conditions as given in the time-dependent case. The free-streaming boundary conditions for the steady-state case are shown below while the diffusive-adiabatic solution is shownin the appendix.

As shown previously for the boundary conditions in the time-dependent solution, the spatial separation function g satisfies the free-streaming boundary conditions,

$$(\hat{v}\hat{\kappa}y)^{1/2}g'(y) + g(y) = 0 \ , \quad \text{at} \quad y = y_{\text{in}} \ , \tag{4.11}$$

$$(\hat{v}\hat{\kappa}y)^{1/2}g'(y) - g(y) = 0 \ , \quad \text{at} \quad y = y_{\text{out}} \ . \tag{4.12}$$

Additionally, I can normalize the solution so that

$$g(y_{\text{in}}) = 1 \ . \tag{4.13}$$

The constants A and B are then solved for by substituting Equation (4.10) into the boundary conditions and performing algebra. Note that the eigenvalues, λ_n, in this solution are the same as in the time-dependent case when $\tilde{\omega} = 0$ and therefore can be numerically solved for by the exact solution shown here or by the same method identified in Section 2.3.4, with the special case where $\tilde{\omega} = 0$.

4.4.2 Energy Equation

The separated energy equation and its associated boundary conditions are exactly the same as the time-dependent solution shown in Section 2.3.4 and therefore has the exact same solutions given by,

$$h_n(\chi, \chi_0) = \chi^{\kappa-4} e^{-\chi/2} M_{\kappa,\mu}(\chi_{\text{min}}) W_{\kappa,\mu}(\chi_{\text{max}}) \ , \tag{4.14}$$

where $M_{\kappa,\mu}$, and $W_{\kappa,\mu}$ denote the Whittaker functions,

$$\chi_{\text{min}} \equiv \min(\chi, \chi_0) \ , \qquad \chi_{\text{max}} \equiv \max(\chi, \chi_0) \ , \tag{4.15}$$

and where the parameters κ and μ are given by

$$\kappa \equiv \frac{1}{2}(\delta + 4) \ , \qquad \mu \equiv \frac{1}{2}\left[(3-\delta)^2 + 4\delta\lambda_n\right]^{1/2} \ . \tag{4.16}$$

4.4.3 Orthogonality

The quiescent proof of spatial function orthogonality follows the same procedure as the time-dependent one above. In this case, I rewrite Equation (4.7), which is shown below,

$$y\frac{d^2 g}{dy^2} - \left(\frac{3}{2} + y\right)\frac{dg}{dy} + \frac{\lambda}{2}g = 0 \ , \tag{4.17}$$

in the Sturm-Liouville form

$$\frac{d}{dy}\left[S(y)\frac{dg_n}{dy}\right] + Q(y)g_n + \frac{\lambda_n}{2}\Omega(y)g_n = 0 \ , \tag{4.18}$$

where the weight function, $\Omega(y)$, is defined by

$$\Omega(y) = y^{-5/2}e^{-y} \ , \tag{4.19}$$

and the functions $S(y)$ and $Q(y)$ are defined by

$$\begin{aligned} S(y) &= y^{-3/2}e^{-y} \ , \\ Q(y) &= 0 \ . \end{aligned} \tag{4.20}$$

Note that $S(y)$ and $\Omega(y)$ are the same values as in the time-dependent case. As before, assume that λ_n and λ_m represent distinct eigenvalues associated with the spatial eigenfunctions g_n and g_m, respectively. Equation (4.18) is then multiplied by g_m and the result is subtracted from the same equation with the indices n and m interchanged. After some algebra, the result obtained is,

$$g_m \frac{d}{dy}\left[S(y)\frac{dg_n}{dy}\right] - g_n \frac{d}{dy}\left[S(y)\frac{dg_m}{dy}\right] = (\lambda_m - \lambda_n)\Omega(x) g_n g_m \tag{4.21}$$

Integration by parts between the inner and outer radii $y_{\rm in}$ and $y_{\rm out}$ yields,

$$S(y)\left[g_m \frac{dg_n}{dy} - g_n \frac{dg_m}{dy}\right]\Bigg|_{y_{\rm in}}^{y_{\rm out}} = (\lambda_m - \lambda_n)\int_{y_{\rm in}}^{y_{\rm out}} \Omega(y) g_n(y) g_m(y)\, dy \tag{4.22}$$

This is the exact equation as shown in the time-dependent version's above with the same definition of S. Therefore as noted before, utilizing either the spatial free-streaming boundary conditions or the alternate boundary conditions at the inner and outer radii, the left-hand side of Equation (4.22) vanishes resulting in,

$$\int_{y_{\rm in}}^{y_{\rm out}} \Omega(y) g_n(y) g_m(y)\, dy = 0 \ , \quad \lambda_n \neq \lambda_m \ . \tag{4.23}$$

This establishes that the spatial eigenfunctions g_n and g_m are orthogonal with respect to the weight function $\Omega(y)$ in the computational domain located between the inner and outer boundaries at $y = y_{\rm in}$ and $y = y_{\rm out}$, respectively.

4.5 Final Closed-Form Solution

As in the time dependent case, since the spatial eigenfunctions have been shown to be orthogonal, it is possible to solve for the Green's function, $f_{\rm G}$, as an infinite series

$$f_{\rm G}(y_0, y, \chi_0, \chi) = \sum_{n=1}^{N_{\rm max}} b_n g_n(y, y_0) h_n(\chi, \chi_0) \ , \tag{4.24}$$

Performing the same calculations in the same vein as the time-dependent case, the derivative jump condition is as follows:

$$\lim_{\varepsilon\to 0}\Delta\left[\chi^4\frac{\partial f_{\rm G}}{\partial\chi}\right]\Bigg|_{\chi=\chi_0-\varepsilon}^{\chi=\chi_0+\varepsilon}=\frac{-\delta\dot{N}_0\hat{\kappa}^{3/2}\delta(y-y_0)y^{5/2}}{2\pi\hat{v}^{5/2}R_g^2c(m_ec^2)^3\Theta^3}\ , \tag{4.25}$$

The expansion coefficients, b_n, can be determined by exploiting the orthogonality of the spatial eigenfunctions, and applying the derivative jump condition. Substituting Equation (4.24) into Equation (4.25) gives,

$$\sum_{n=1}^{N_{\rm max}} b_n g_n(y)\chi_0^{\kappa-4}e^{-\chi_0/2}\mathfrak{W}_\chi(\chi_0)=\frac{-\delta\dot{N}_0\hat{\kappa}^{3/2}\delta(y-y_0)y^{5/2}}{2\pi\hat{v}^{5/2}R_g^2c(m_ec^2)^3\Theta^3\chi_0^4}\ , \tag{4.26}$$

where the Wronskian, $\mathfrak{W}_\chi(\chi_0)$, is defined by (Becker & Wolff 2007)

$$\mathfrak{W}_\chi(\chi_0)\equiv M_{\kappa,\mu}(\chi_0)W'_{\kappa,\mu}(\chi_0)-W_{\kappa,\mu}(\chi_0)M'_{\kappa,\mu}(\chi_0)=\frac{-\Gamma(1+2\mu)}{\Gamma(\mu-\kappa+1/2)}\ . \tag{4.27}$$

The expression for the expansion coefficient, b_n, can now be obtained by substituting Equation (4.27) into Equation (4.26), reorganizing, multiplying by the product $g_m(y)\Omega(y)$, where $\Omega(y)$ is the weight function as defined above, and integrating with respect to y from $y_{\rm in}$ to $y_{\rm out}$. Utilizing the orthogonality of the spatial eigenfunctions, I find after some algebra that the final expression for the expansion coefficient b_n can be written as

$$b_n=\frac{\delta\dot{N}_0\hat{\kappa}^{3/2}g_n(y_0)\Omega(y_0)e^{\chi_0/2}y^{5/2}\Gamma(\mu-\kappa+\frac{1}{2})}{2\pi\hat{v}^{5/2}R_g^2c(m_ec^2)^3\Theta^3\chi_0^\kappa\mathfrak{I}_n\Gamma(1+2\mu)}\ , \tag{4.28}$$

where the quadratic normalization integrals, $\mathfrak{I}_n$, are computed via numerical integration, using the definition

$$\mathfrak{I}_n\equiv\int_{y_{\rm in}}^{y_{\rm out}}\Omega(y)g_n^2(y)\,dy\ . \tag{4.29}$$

Combining Equations (4.24) and (4.28), I find that the final closed-form solution for $f_{\rm G}$ is given by

$$\begin{aligned} f_{\rm G}(y_0, y, \chi_0, \chi) = & \frac{\delta \dot{N}_0 \hat{\kappa}^{3/2} \chi^{\kappa-4} \Omega(y_0) e^{(\chi_0-\chi)/2} y_0^{5/2}}{2\pi \hat{v}^{5/2} R_g^2 c (m_e c^2)^3 \Theta^3 \chi_0^{\kappa}} \\ & \times \sum_{n=1}^{N_{\rm max}} \frac{\Gamma(\mu - \kappa + \frac{1}{2})}{\Im_n \Gamma(1+2\mu)} g_n(y_0) g_n(y) M_{\kappa,\mu}(\chi_{\rm min}) W_{\kappa,\mu}(\chi_{\rm max}) \ , \end{aligned} \tag{4.30}$$

where κ, μ, $\chi_{\rm min}$, and $\chi_{\rm max}$ are computed using Equations (4.16) and (4.15). Equation (4.30) gives the final solution of the radiation Green's function, $f_{\rm G}$, at energy x and radius y. The photons are injected at radius y_0 with energy x_0.

4.6 Injection Sources

In order to solve for the radiation spectrum, an injection photon source must be inputted that in turn creates the observed photons after interacting with the model. As noted in Chapter 1, there are many possible sources of radiation surrounding accreting black holes. One of the benefits of the method utilized in this dissertation is that the radiation Green's function solved for in both the time-dependent and time-independent cases can be convolved with any source photon distribution since the transport equation is a linear partial differential equation. The integral convolution for any steady-state source photon distribution $\dot{Q}$ is given by,

$$f_p(r, \epsilon) = \int_{r_{in}}^{r_{out}} \int_0^{\infty} 4\pi r_0^2 \epsilon_0^2 \dot{Q}(r_0, \epsilon_0) \frac{f_{\rm G}(r_0, r, \epsilon_0, \epsilon) dr_0 d\epsilon_0}{\dot{N}_0}, \tag{4.31}$$

where $4\pi r_0^2 \epsilon_0^2 \dot{Q}(r_0, \epsilon_0) dr_0 d\epsilon_0$ gives the number of photons injected in the energy range $d\epsilon_0$, radius range dr_0, around (ϵ_0, r_0).

Although Equation (4.31) represents the fundamental solution for the radiation field inside the spherically symmetric accretion flow, it still remains necessary to compute the *escaping* radiation field in order to plot the observed spectrum. The theoretical X-ray steady-state photon flux spectrum observed at the detector is directly related to the radiation distribution escaping from the outer edge of the spherical region, located at radius $r = r_{\rm out}$. Since the boundary condition at the outer radius is free-streaming (Equation (4.12)), the computation of the escaping radiation spectrum is self-consistent and the X-ray photon spectrum observed at the detector, that can now be compared to observational data, is given by

$$\mathscr{F}_\epsilon(\epsilon) = c \left(\frac{r_{\rm out}}{D}\right)^2 \epsilon^2 f_p(r_{\rm out}, \epsilon) \ . \tag{4.32}$$

where D is the distance from the source to the detector on the earth and f_p is given by Equation (4.31).

4.6.1 Monochromatic Source

A monochromatic source is not the most commonly anticipated radiation process occurring in the areas surrounding an accreting black hole. However, as noted in Chapter 3, there appear to be certain situation where monochromatic injection of radiation does make sense. The formulation of the Green's function solution given by Equation (4.30) was solved for using the monochromatic source distribution $\dot{Q} = (\dot{N}_0 \delta(r - r_0)\delta(\epsilon - \epsilon_0))/(4\pi r_0^2 \epsilon_0^2)$. Notice that convolving this with $f_{\rm G}$ in Equation (4.31) returns the original function $f_{\rm G}$. Therefore, the equation needed to plot the radiation spectrum is simply given by,

$$\mathscr{F}_\epsilon(\epsilon) = c \left(\frac{r_{\rm out}}{D}\right)^2 \epsilon^2 f_{\rm G}(r_{\rm out}, \epsilon) \tag{4.33}$$

where $f_{\rm G}$ is given by Equation (4.30).

4.6.2 Bremsstrahlung Source

As noted in Chapter 1, many radiative processes are broadband. A likely source of this is thermal bremsstrahlung radiation given by,

$$\varepsilon_\nu^{ff}(r_0,\nu_0) = 6.8\times10^{-38} Z^2 n_e^2(r_0) T_e^{-1/2} e^{-(h\nu_0)/(kT_e)} \bar{g}_{ff} \tag{4.34}$$

where ε_ν^{ff} is found in Rybicki and Lightman (1979) and $\bar{g}_{ff}$ is a velocity-averaged relativistic corrective Gaunt factor which here is set equal to unity. For pure, fully-ionized hydrogen, $Z = 1$. Convolving this source term with Equation (4.31) and changing variables from ϵ to ν, the bremsstrahlung radiation field inside the corona is given by,

$$f_B(r,\nu) = \int_{r_{in}}^{r_{out}} \int_0^\infty 4\pi r_0^2\, \varepsilon_\nu^{ff}(r_0,\nu_0) \frac{f_{\rm G}(r_0,r,\nu_0,\nu) dr_0 d\nu_0}{\dot{N}_0\, h\nu_0} \ . \tag{4.35}$$

Making use of Equation (4.3) and non-dimensionalizing, the radiation field is now given by,

$$f_B(y,\chi) = \int_{y_{\rm out}}^{y_{\rm in}} \int_0^\infty \Big(\frac{f_{\rm G}(y,y_0,\chi,\chi_0)}{\dot{N}_0}\Big) \varepsilon_\nu^{ff} \Big(\frac{\hat{v}R_g}{\hat{\kappa}}\Big)^3 \Big(\frac{4\pi}{y^4}\Big) \frac{dy_0 d\chi_0}{h\chi_0}, \tag{4.36}$$

Using Equation (4.34) and the relationship for n_e as shown in Equation (4.3), the final, non-dimensionalized bremsstrahlung radiation field inside the corona is given by,

$$f_B(y,\chi) = 6.8\times10^{-38} \int_{y_{\rm out}}^{y_{\rm in}} \int_0^\infty f_{\rm G}(y,y_0,\chi,\chi_0) \frac{4\pi R_g dy_0 d\chi_0}{(3\sigma_{\rm T}\hat{\kappa})^2 h \dot{N}_0 T_e^{1/2} \chi_0 e^{\chi_0} y_0} \ . \tag{4.37}$$

The computation of the escaping radiation spectrum produced by thermal bremsstrahlung radiation can now be compared to observational data and is given by

$$\mathscr{F}_\epsilon(\epsilon) = c\left(\frac{r_{\rm out}}{D}\right)^2 \epsilon^2 f_B(r_{\rm out},\epsilon) \ . \tag{4.38}$$

Chapter 5: Quiescent Application to AGN 1H0707-495

5.1 Observational Data

Similar to other NLS1 galaxies, H707 has a steep spectrum and shows a strong soft excess in the X-ray which is traditionally interpreted as blackbody radiation. As noted in Chapter 3, the steady-state spectrum of H707 appears to be comprised of multiple components. Figures 5.1 and 5.2 show two fits of the observed spectrum. In general, a majority of the spectrum is well fitted in each of these cases by simply combining a blackbody thermal component below 1 keV as well as a power law component that extends from below to above 1 keV.

Both Zoghbi et al. (2010) and Pawar et al. (2016) used observations attained by XMM-Newton in 2008 with the European Photon Imaging Camera-pn (EPIC-pn) in large window imaging mode with medium filter while the optical monitor was operated with UVW1 filter in fast imaging mode. The data was analyzed using Science Analysis System (SAS) and the spectral fits were performed using NASA's High Energy Astrophysics Science Archive Research Center (HEASARC) XPSEC software.

For the spectral fit, Zoghbi et al. (2010) used blackbody, power law, and blurred reflection components which included broad energy lines accounting for the iron-L and Kα lines. Pawar used a similar fit, but did not include a "reflection" fit. The assumed parameter values for Zohgbi's plot were inner radius of $r_{\text{in}} = 1.41R_g$, outer radius of $r_{\text{out}} = 400R_g$, and blackbody temperature of 50 eV. Pawar's assumed parameter values used a blackbody temperature of 108 eV and inner and outer radius of $r_{\text{in}} < 1.7R_g$ and $r_{\text{out}} < 400R_g$ respectively.

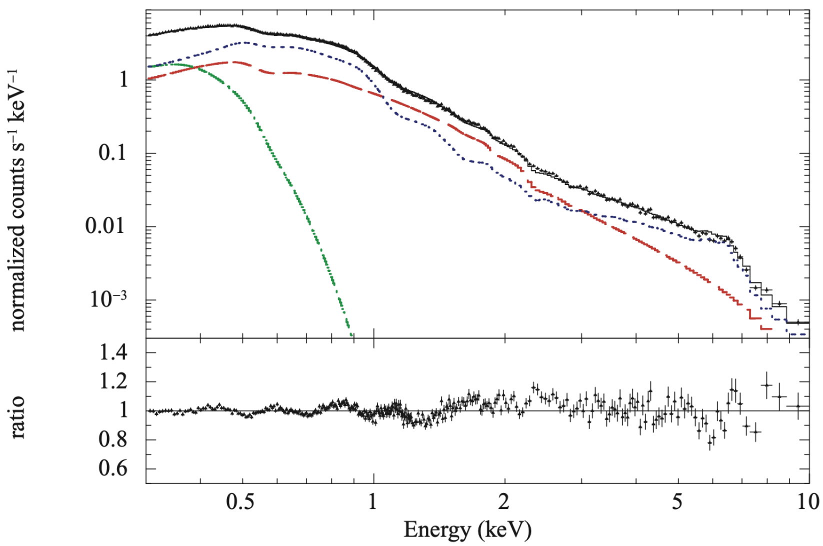

Figure 5.1: Plot of H707 spectrum. Long-dashed (red) line is the power law, dot-dashed (green) line is the blackbody, and dotted (blue) line is the blurred reflection component. The black line is the total. Credit: Zoghbi et al. (2010).

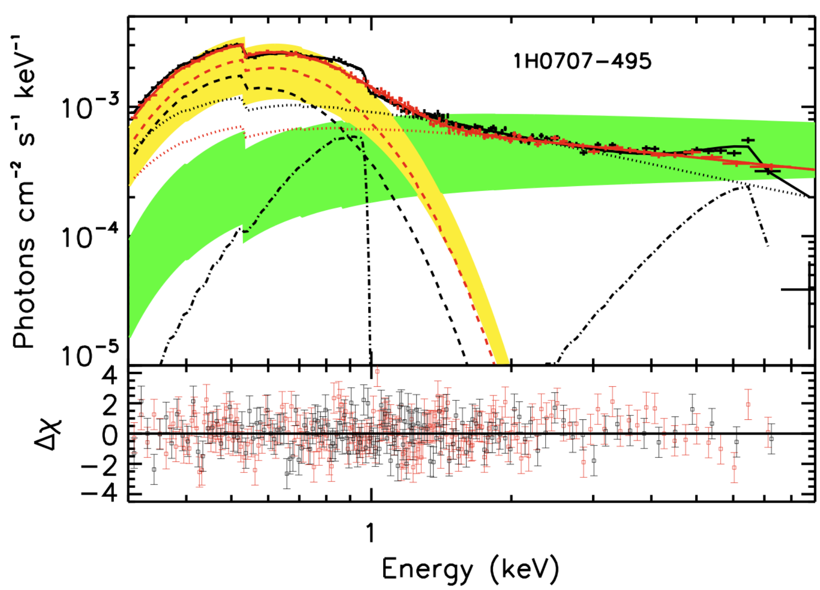

Figure 5.2: H707 time averaged (black) and simulated (red) spectrum with blackbody (dashed), plower law (dotted), and two Laor lines (dash-dotted lines). Shaded green (power law) and yellow (blackbody) displays area between lowest and highest flux values. Credit: Pawar et al. (2016).

5.2 Model Parameters and Calculations

In order to determine if the same coronal model that worked for the time-dependent transport equation works for the quiescent solution, where applicable the same model parameters are utilized. Hence, noting the calculation method in Chapter 4, in order to find the eigenvalues I need to first provide the values for the inner and outer radius, the radial velocity, and the accretion rate. Therefore, referencing Chapter 3, for the mass I use $M = 2 \times 10^6 M_\odot$ and for the spin parameter I use $a = 0.98$, which when combined to solve for the inner radius gives $r_{\rm in} = r_{\rm ISCO} = 1.61 R_g$. I set the outer radius to $r = 120 R_g$. I also set the dimensionless radial velocity to $\hat{v} = \sqrt{2}$ and the accretion rate to $\dot{M} = 1.1 \dot{M}_E$. With these values established, I am able to numerically solve for the eigenvalues that will be needed to calculate the radiation spectrum.

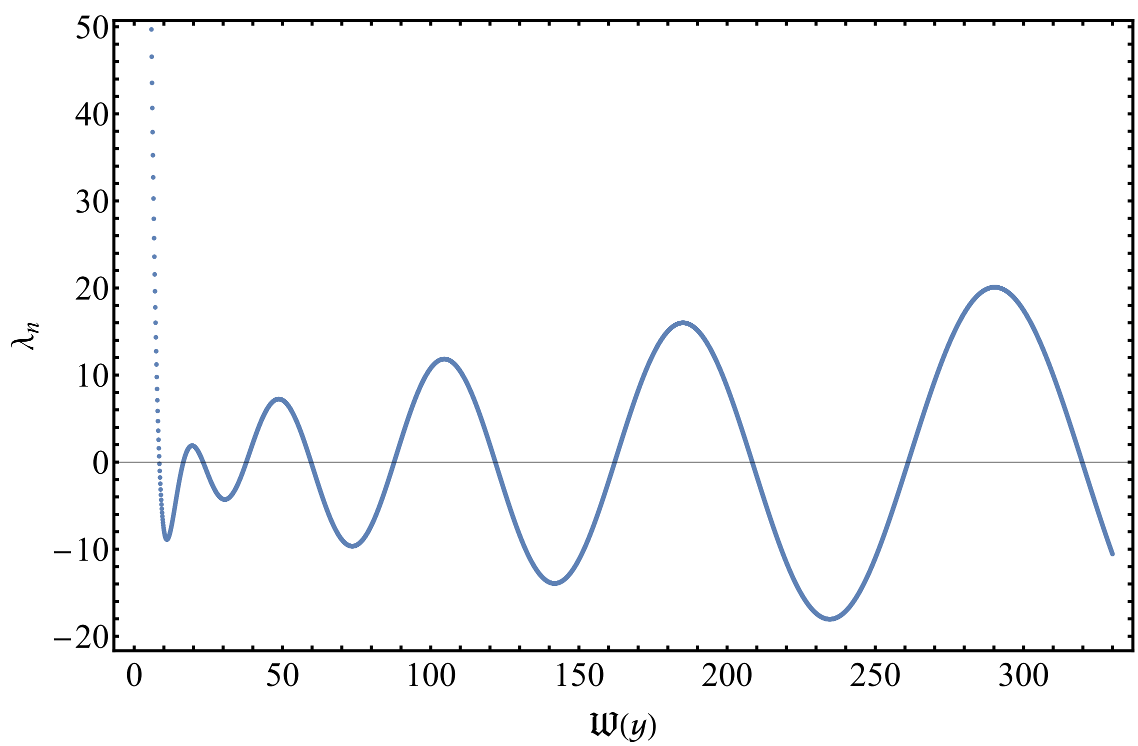

Figure 5.3: Plot of the numerically solved quiescent spatial Wronskian. The eigenvalues occur at the crossings, when $\lambda = 0$.

Similar to the quiescent model, I utilize the free-free streaming boundary conditions and solve the spatial equation at both the outer and inner boundaries going inward and outward respectively toward an undefined spatial point in the middle of the radius. I solve for the Wronskian following the method outlined in Section 2.3.4, by setting $\tilde{\omega} = 0$. Figure 5.3 shows a graphical representation of the solutions at the crossings.

Next, in order to solve for the radiation spectrum in accordance with Equation (4.30), I set the source photon rate to $\dot{N} = 10^{51}$ and in accordance with Chapter 3 values, I set the coronal temperature to $\Theta = 0.05$. Note that depending on the source used, changing the number of photons either will or will not change the value of the flux. Finally, in order to compare observational to theoretical X-ray steady-state photon flux spectrum observed at the detector, regardless of the injection source utilized, I must use Equation (4.38), which is restated here,

$$\mathscr{F}_\epsilon(\epsilon) = c \left(\frac{r_{\rm out}}{D} \right)^2 \epsilon^2 f_p(r_{\rm out}, \epsilon) \ . \tag{5.1}$$

Note that this equation requires the distance to H707, which in Chapter 3 was given as $D = 181$ Mpc (Sani et al. 2010).

5.3 Quiescent Spectrum

5.3.1 Monochromatic Injection Source

As a first effort to reproduce the observed spectrum using my transport equation, I utilize the same monochromatic injection energy source as was used for the time-dependent spectrum. In order to accomplish this, I numerically solve Equation (4.30) for a given set of eigenfunctions. I find that the energy solution converges to within 1% after five terms and so I utilize ten terms to ensure an accurate solution.

The final step to produce the theoretical spectrum is to utilize the eigenfunctions with

Equation (4.33). The resulting plot is shown in Figure 5.4. As can be seen, the monochromatic injection energy can neither produce the observed composite spectrum or the individual predicted components of a thermal broadband or power law spectrum noted in other author's XSPEC fittings in shape. However, almost all authors have concluded that monochromatic source energy still appears to be responsible for an aspect of the energy spectrum in the form of emission lines. Pawar et al. (2016), note an excess in the energy in spectrum near both the iron-L and Kα line energies and employ a broadened emission line from an accretion disk that includes general relativity effects (Laor in XSPEC) at these energies to improve their spectrum fits. I will discuss this further in Section 5.4.

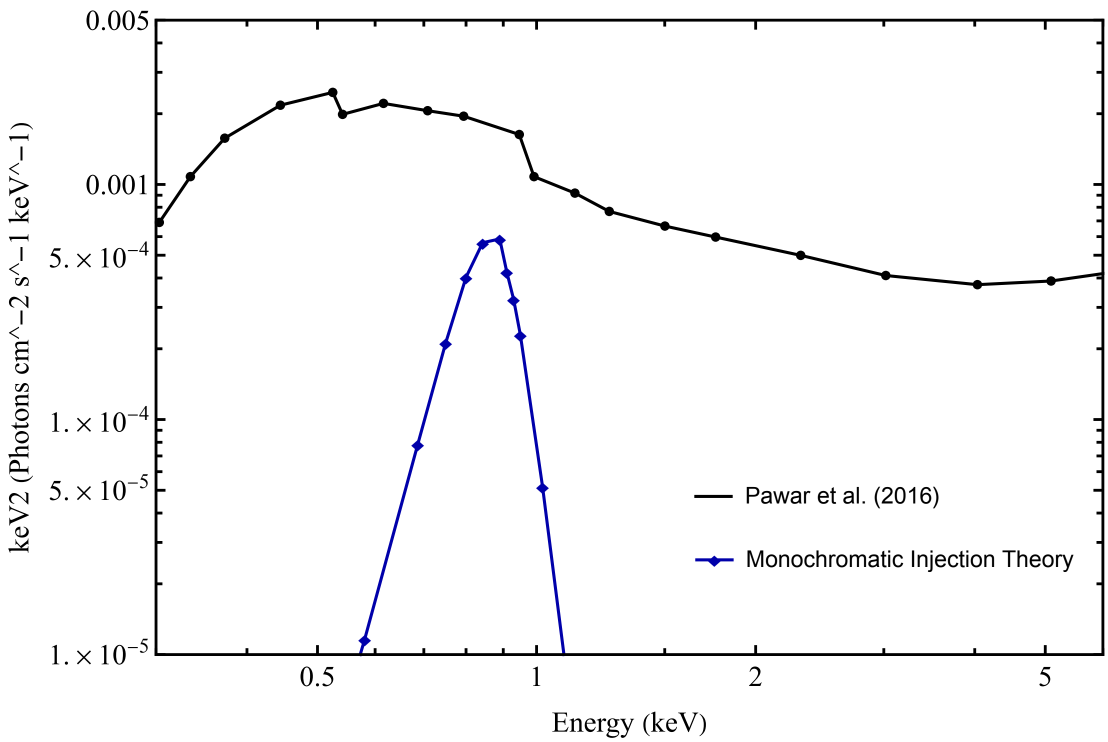

Figure 5.4: Plot of observed H707 spectrum as compared to theoretical monochromatic injection spectrum with an injection energy at $\epsilon_0 = 0.89$ keV. Although the injection energy cannot produce the broadband or power law spectrum components, it may still be responsible for the excess noted.

5.3.2 Bremsstrahlung Source

As stated in Chapter 4, another potential source of seed photons that helps generate the observed spectrum is a broadband source such as bremsstrahlung. Following the prescription in Chapter 4, the eigenvalues are the same as in the monochromatic solution, with the only difference occurring when convolving the source energy in order to achieve the radiation spectrum. For the bremsstrahlung solution, I must solve Equation (4.37), which requires me to integrate over both the entire radius and the entire broadband energy spectrum for each desired energy output. In order to achieve these results, as a practical matter, I reduce the double integral in Equation (4.37) to a single integral by noting that the spatial function and energy function are seperable and that additionally, the spatial function operates over a sum of values. Rewriting Equation (4.37) below I have,

$$f_B(y,\chi) = 6.8\times10^{-38}\int_{y_{\rm out}}^{y_{\rm in}}\int_0^\infty f_{\rm G}(y,y_0,\chi,\chi_0)\frac{4\pi R_g dy_0 d\chi_0}{(3\sigma_{\rm T}\hat{\kappa})^2 h\dot{N}_0 T_e^{1/2}\chi_0 e^{\chi_0} y_0}\ . \tag{5.2}$$

Including the complete Green's function, $f_{\rm G}$, Equation (5.2) becomes,

$$\begin{aligned} f_B(y,\chi) &= 6.8\times10^{-38}\int_{y_{\rm out}}^{y_{\rm in}}\int_0^\infty \frac{\delta\dot{N}_0\hat{\kappa}^{3/2}\chi^{\kappa-4}\Omega(y_0)e^{(\chi_0-\chi)/2}y_0^{5/2}}{2\pi\hat{v}^{5/2}R_g^2 c(m_e c^2)^3\Theta^3\chi_0^\kappa} \\ &\times\sum_{n=1}^{N_{\rm max}}\frac{\Gamma(\mu-\kappa+\frac{1}{2})}{\Im_n\Gamma(1+2\mu)}g_n(y_0)g_n(y)M_{\kappa,\mu}(\chi_{\rm min})W_{\kappa,\mu}(\chi_{\rm max})\frac{4\pi R_g dy_0 d\chi_0}{(3\sigma_{\rm T}\hat{\kappa})^2 h\dot{N}_0 T_e^{1/2}\chi_0 e^{\chi_0}y_0}\ , \end{aligned} \tag{5.3}$$

Now, only acting the spatial integral on those terms with a spatial dependence, this is rewritten as,

$$f_B(y,\chi) = 6.8\times10^{-38}\int_0^\infty \frac{\delta\dot{N}_0 4\pi R_g\hat{\kappa}^{3/2}\chi^{\kappa-4}e^{(\chi_0-\chi)/2}}{(3\sigma_{\rm T}\hat{\kappa})^2 h\dot{N}_0 T_e^{1/2}2\pi\hat{v}^{5/2}R_g^2 c(m_e c^2)^3\Theta^3\chi_0^\kappa\chi_0 e^{\chi_0}}$$
$$\times\sum_{n=1}^{N_{\rm max}}\frac{\Gamma(\mu-\kappa+\frac{1}{2})}{\Im_n\Gamma(1+2\mu)}\int_{y_{\rm out}}^{y_{\rm in}}\frac{y_0^{5/2}\Omega(y_0)}{y_0}g_n(y_0)dy_0 g_n(y)M_{\kappa,\mu}(\chi_{\rm min})W_{\kappa,\mu}(\chi_{\rm max})d\chi_0\ , \tag{5.4}$$

or equivalently,

$$f_B(y,\chi) = \frac{\delta\chi^{\kappa-4}1.51\times10^{-38}}{\sigma_{\rm T}^2 h(T_e\hat{\kappa})^{1/2}\hat{v}^{5/2}R_g c(m_e c^2)^3\Theta^3 e^{\chi/2}}\int_0^\infty\frac{1}{\chi_0^{\kappa+1}e^{\chi_0/2}}$$
$$\times\sum_{n=1}^{N_{\rm max}}\frac{\Gamma(\mu-\kappa+\frac{1}{2})}{\Im_n\Gamma(1+2\mu)}J_n g_n(y)M_{\kappa,\mu}(\chi_{\rm min})W_{\kappa,\mu}(\chi_{\rm max})d\chi_0\ , \tag{5.5}$$

where

$$J_n = \int_{y_{\rm out}}^{y_{\rm in}}\frac{y_0^{5/2}\Omega(y_0)}{y_0}g_n(y_0)dy_0 = \int_{y_{\rm out}}^{y_{\rm in}}\frac{e^{-y_0}}{y_0}g_n(y_0)dy_0\ . \tag{5.6}$$

I now utilize Mathematica to solve for the spectrum. I utilize these results with Equation (4.38) in order to produce the theoretical radiation spectrum. As shown in Chapter 1, bremsstrahlung radiation produces well defined spectra dictated by the temperature and density of the gas, which implies that even if it is unable to produce the composite spectrum, it may produce a component. The theoretical spectrum compared to observational data is shown in Figure 5.5.

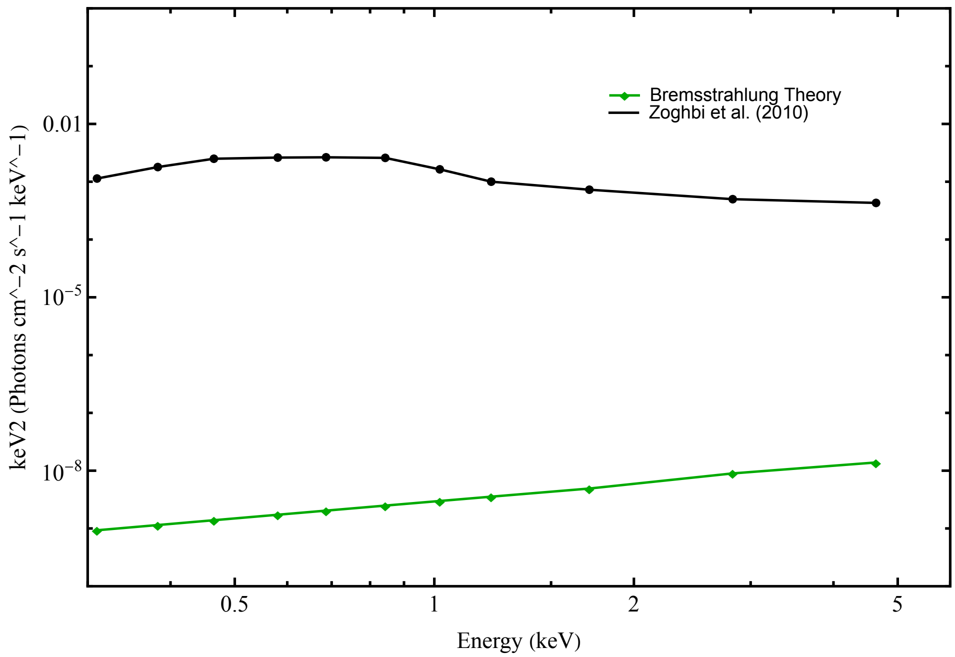

Figure 5.5: Plot of observed H707 spectrum as compared to theoretical bremsstrahlung spectrum.

Although, due to integrating the radiation function over the entire radius and all of the energy, the photon count is much closer to the observations than the monochromatic source energy was, it is still much smaller than either the observed composite spectrum or the individual predicted components. As can be seen by Figure 5.5, the bremsstrahlung plot does not achieve a plot similar to the overall observed composite spectrum or an individual component of the spectrum. In fact, as opposed to the predicted spectral components that would fit the spectrum which show a steady decrease in photon count around 0.5 keV, the theoretical bremsstrahlung spectrum plotted is still increasing at all of the observed energies. This combined with the low efficiency of bremsstrahlung in the spherical accretion flow suggests that the steady-state X-ray spectrum is the result of emission from a much cooler, radially larger, thin disk, that surrounds the spherical inner region. This discrepancy will be discussed in further detail in Section 5.4.

5.4 Discussion

In general, my transport model does not appear to be able to reproduce the spectrum of H707 when utilizing the same values as used to successfully replicate the time lags. The temperature in the coronal cloud appears to be much too high to generate the observed thermal radiation. However, the results do give evidence as to what may produce the thermal spectrum and the coronal cloud also may still potentially be responsible for at least part of the non-thermal spectrum.

5.4.1 Thermal Radiation

Bremsstrahlung

The calculated and plotted bremsstrahlung spectrum does not appear to be able to replicate portions of the spectrum with the utilized cloud temperature. However, the plotted theoretical bremsstrahlung spectrum does provide clues as to what is generating the observed spectrum. Noting that the bremsstrahlung spectrum in Figure 5.5 shows a rise throughout the observed energies, and recalling the standard predictable nature and spectra of bremsstrahlung radiation from Chapter 1, it appears that the temperature of the coronal cloud must be much too high. In order to validate this, I plot the theorized coronal temperature as well as two other bremsstrahlung plots for different temperatures in Figure 5.6.

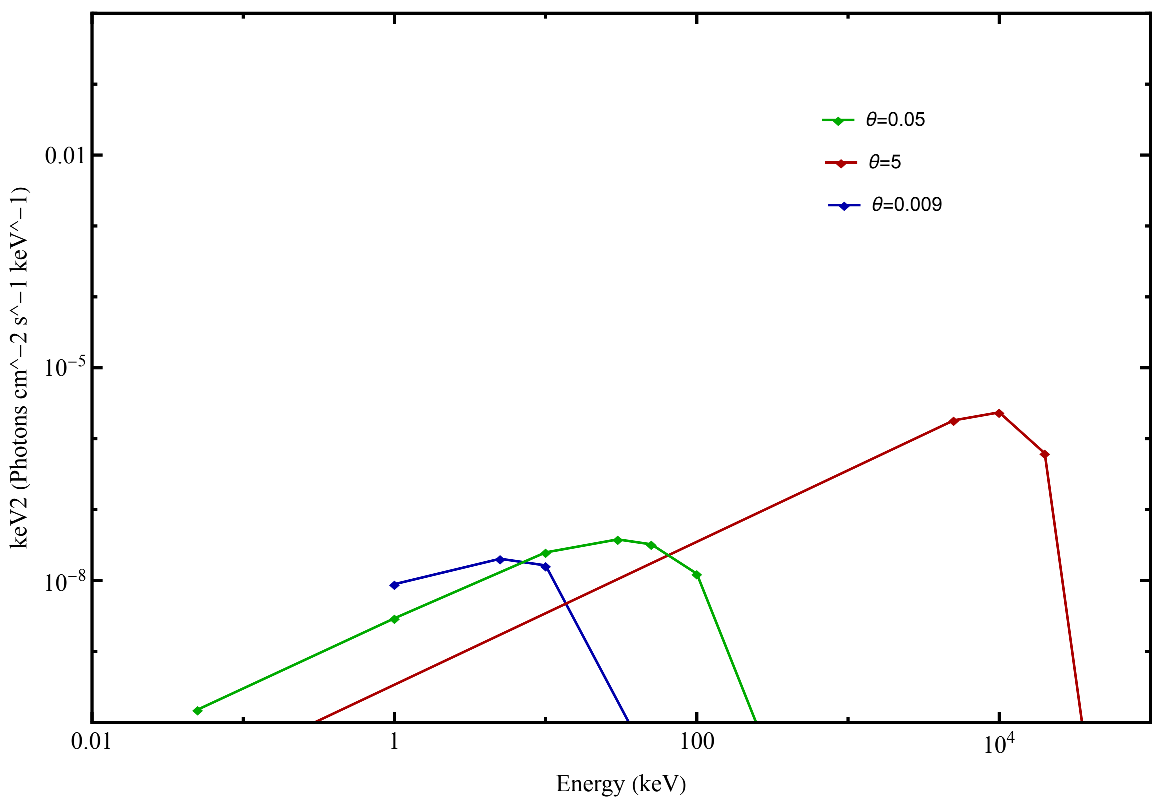

Figure 5.6: Plot of different theoretical bremsstrahlung spectrum's for varying temperatures.

As can be seen, a hotter temperature shifts the spectral shape of the bremsstrahlung spectrum to the right and a cooler temperature shifts the spectral shape to the left. The count rate peaks at energies further to the right as the temperature of the cloud increases. As the temperature rises, bremsstrahlung becomes much more prevalent of a potential radiation source and the number of photons increases. Additionally, note that the number of photons produced by the bremsstrahlung plot is much too low as compared to the observed count rate. Increasing the optical depth also will increase the count rate of the plot as noted from Chapter 1. These results suggest that the optically thin coronal cloud cannot produce enough seed photons to explain the observed thermal X-ray spectrum and is also much too hot to match the observed profile. Hence, in conjunction with our optically thin, hot corona, the results imply that the most likely explanation for generating the steady-state X-ray spectrum is a cooler, optically thick source such as an accretion disk that lies under the corona and extends much farther out radially.

Blackbody

A second potential source of thermal radiation from the coronal cloud is blackbody radiation. Reviewing the observational spectrum for thermal blackbody radiation and noting Wien's law in Equation (1.3), the temperature of the cloud required to create a spectral peak at around 0.2 keV as shown in the observed spectra of Figure's 5.1 and 5.2 is $\Theta \approx 0.0004$. However, my utilized cloud temperature is $\Theta = 0.05$. Therefore, it immediately appears that the coronal cloud is much too hot to produce the observed spectrum from blackbody radiation. One can further explore this potential radiation source and determine if blackbody emission from the hot coronal cloud is even a viable alternative by solving for the maximum blackbody temperature of an accreting gas orbiting a compact object. Similar to the previous derivation of the Eddington luminosity, the maximum temperature is determined by equating the gravitational force to the radiation force. In this case, one write's the radiation force using Stefan-Boltzmann's law, which describes the power radiated from a black body in terms of its temperature, which gives,

$$F_g = F_{\rm rad} \quad \rightarrow \quad \frac{GMm_p}{r^2} = \frac{\sigma_{SB} T^4 \sigma_T}{c} \ . \tag{5.7}$$

Noting that the smallest possible radius will achieve the highest possible temperature, I use one gravitational radius as the upper limit (although, the radius of the accreting gas will be much larger thereby reducing the temperature even further). Setting $r = R_G$, substituting, and solving for $T_{\rm max}$ gives,

$$T_{\rm max} = \left(\frac{c^5 m_p}{\sigma_T G M \sigma_{SB}} \right)^{1/4} = 5.32 \times 10^7 \text{ K} \left(\frac{M}{M_\odot} \right)^{-1/4} \ . \tag{5.8}$$

If the mass of H707 is used, where $M = 2 \times 10^6 M_\odot$, then the maximum temperature possible for blackbody radiation from H707 is $T_{\max} = 1.41 \times 10^6$ K, or in energy and dimensionless units, $kT_{\max} = 0.12$ keV and $\theta = 0.00024$ respectively. Noting that my theoretical coronal temperature is $\theta = 0.05$, it is obvious that my corona cannot produce the blackbody spectrum. Additionally, again using Wien's law to find the peak spectral energy density for this temperature, the spectrum for this temperature will peak at $E_{\text{peak}} = 0.344$ keV which is higher than the observed peak. This peak energy will decrease for lower temperatures which means the blackbody temperature must be even lower than the maximum possible temperature. Similar to the bremsstrahlung results, these results imply the existence of a much cooler accretion disk that exists under the corona and extends farther out radially

Thermal Comptonization in the Corona

Finally, one can analyze whether thermal Comptonization within the corona contributes to the observed thermal spectrum. Although, the corona does not appear to be responsible for generating the thermal spectrum, it is important to investigate whether the the spectrum produced by the accretion disk that passes through the corona will be altered. Recall from Chapter 1, the Compton y-parameter is given by,

$$y = \frac{4k_B T_e}{m_e c^2} \text{Max}(\tau_{es}, \tau_{es}^2) \ . \tag{5.9}$$

Utilizing $\Theta = k_B T_e / m_e c^2 = 0.05$, and the total optical depth at the inner radius, r_{ISCO}, of $\tau = 1.082$, the Compton y-parameter is, $y \sim 0.2$. Again, recall from Chapter 1 that Comptonization only affects radiative processes when $y \gtrsim 1$. Since $y \sim 0.2$, there will not be a large distortion of photons passing through and becoming up-scattered by the hot electrons in the corona. Therefore, it appears the corona in my model has very little impact on the thermal portion of the spectrum.

5.4.2 Non-thermal Radiation

The monochromatic theoretical spectrum, although not able to precisely fit either the complete or a portion of the spectrum, also helps provide a clearer picture of the underlying physics. There appears to be a potential synergy with my transport model and what has been noted as an observed excess of the spectral fits by Zoghbi and Pawar. At the approximate values of the iron L and Kα emission lines, there are observed excesses beyond the composite fit that utilizes the blackbody and power law spectra as shown in Figure 3.1 panel b). To account for this excess, it is common to use the XSPEC Laor emission line models. The spectrum that the XSPEC Laor model produces has a similar shape to my monochromatic injection spectrum. The Laor model includes general relativity effects.

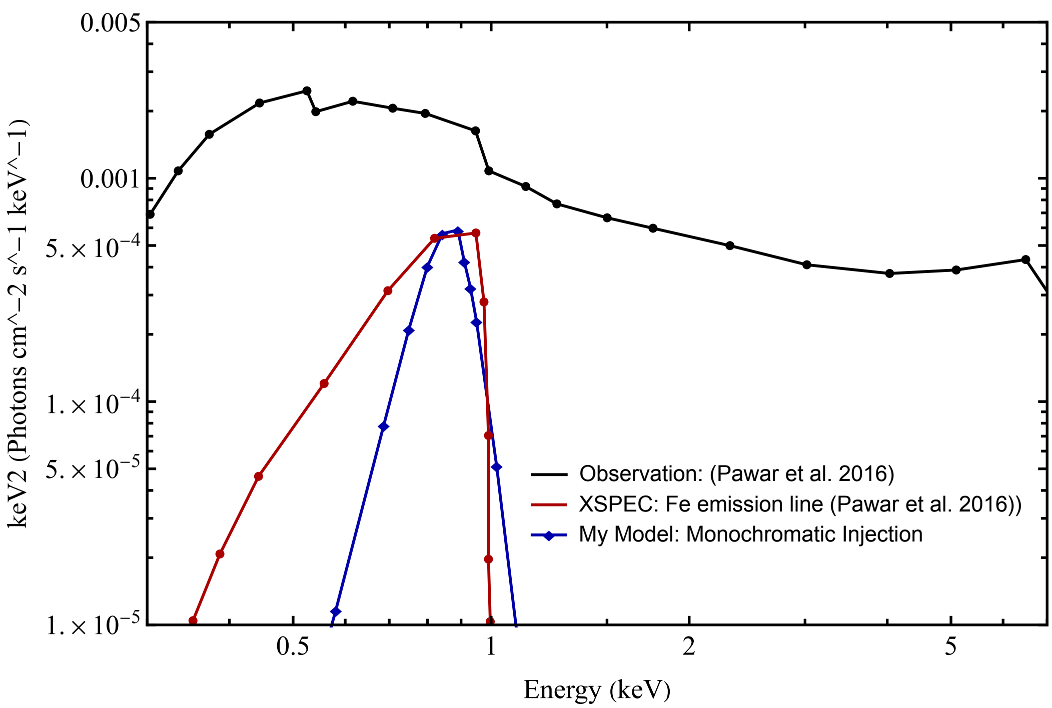

Figure 5.7: Plot of observed spectrum (Zoghbi et al. 2010), simulated iron Laor line spectrum (Pawar et al. 2016), and theoretical monochromatic spectrum with an injection energy at $\epsilon_0 = 0.89$ keV.

Specifically, the Laor emission line spectrum peaks at the emission line energy, which in this case is the same as my injection energy, and then falls off drastically at higher energies as can be seen by Figure 5.7. This correlation provides further qualitative evidence that the iron lines are in fact being produced in abundance and are responsible for generating both the newly observed soft lags as well as the additional soft excess.

Chapter 6: Conclusions

In my dissertation, I have developed and presented a new semi-analytical physical model that successfully replicates the thoroughly researched, yet intensely debated phenomenon identified as soft time lags from AGN by utilizing a simple astrophysical model. I have compared this model to the observational data and previous research thereby validating my work. The development of this semi-analytical model allows me to have complete control of my model parameters and even the ability to employ this model in the future using analysis software. My work represents a significant improvement in the current understanding of key processes being researched in modern high-energy astrophysics. In this final section I summarize my conclusions and present future work.

6.1 Comparison with Previous Models

It is interesting to examine in detail the similarities and differences of my model compared with previous models for the production of soft time lags in AGN. For example, the Fabian et al. (2012) model is taken from Arevalo & Uttley (2006) who note that their model is based on an optically thick, geometrically thin accretion disk which at the center is surrounded by an optically thin, geometrically thick corona (Churazov et al. 2001). Miller's model also has an optically thin corona surrounding the black hole. My corona is also optically thin with the X-ray optical density of my model becoming nearly transparent very quickly with a value of $\tau = 2/3$ at $r = 3.7\ R_g$ and $\tau = 1/3$ at $r = 10.7\ R_g$. Additionally, my modeled corona most likely exists in conjunction with an optically thick, geometrically thin accretion disk. My extended corona of 120 R_g, although larger than Fabian's estimate of 35 R_g, is similar in radius to the 100 R_g reverberation region modeled by Miller et al. (2010). Note that my model does not require the actual photon source to extend throughout the cloud for the creation of time lags, but in fact, as noted in Section 1.4.1, the emitting photons that generate the time lags must be from a variable source of photons located at a specific radius. The injection photons in my model are injected isotropically at a radius value of 16 R_g, which is similar to Fabian et al. (2012), who estimate that the X-ray source extends radially out to $20R_g$. Finally, the temperature of my corona of $kT_e \approx 25$ keV is also similar to Fabian group's coronal temperature estimates. Wilkins et al. (2014) estimates H707's corona temperature to be $kT_e \approx 60$ keV for an optical depth of $\tau = 1$ and Kara et al. (2017), in researching NLS1 Ark 564 which is similar to H707 and accreting at the Eddington limit, determined its corona to be ~ 15 keV. However, a key difference between my model and the other previous models is the physical basis for the time lags.

As discussed in Section 1.4.2, in the reflection model put forward by Fabian et al. (2009) and Zoghbi et al. (2010), the soft lags arise from photons traveling toward the black hole where they lose energy and then are reverberated or reflected out toward the observer. The hard lags are generated by the same direct emission variability photons, but are generated by the photons that travel directly toward the observer against inwardly propagating luminosity fluctuations through the corona. The reverberation explanation of these lags was initially qualitatively addressed. Shortly thereafter, Zoghbi et al. (2011), with partial success, demonstrated a model that correlated their proposed theory. They did this by following the modeling method outlined in Arevalo & Uttley (2006) which is based on fluctuations propagating inwards through an accretion flow modulating the emission of the inner regions as proposed by Lyubarskii (1997). In their model, they used two components (a hard lag emitting component and a simple uniform reflection transfer function for the soft lag emitting component (See Figure 6.1)) to generate their plot. Zoghbi et al. (2011) stated that several combinations of parameters can reproduce the data and so their model shows consistency with the data, but is not a fit. Note in Figure 6.1 the lack of solid correlation with observational data. For instance, how the turnover at low frequencies does not occur and the soft lags are nearly zero in their model.

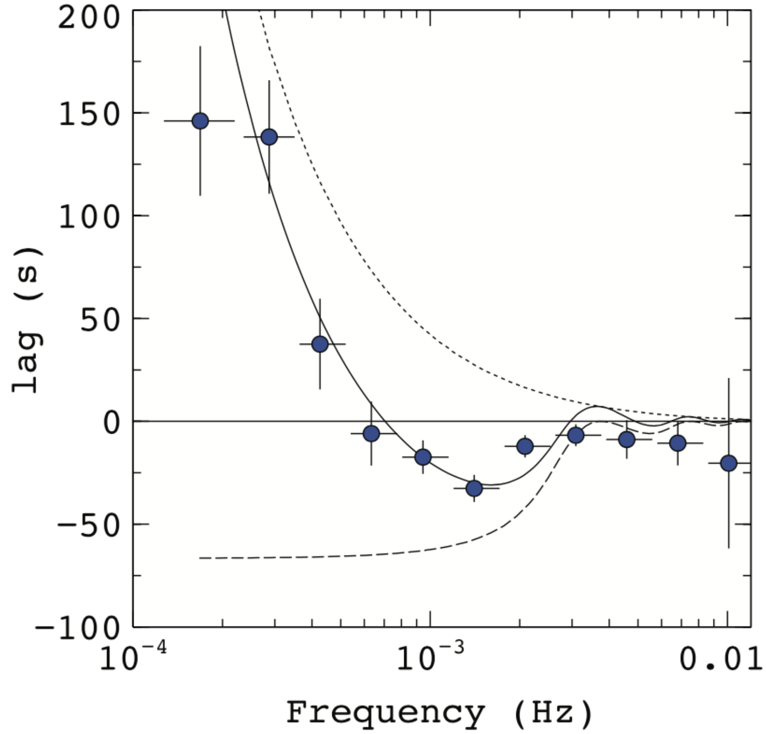

Figure 6.1: H707 lag spectrum with two component model. Dotted line is hard lag propagating fluctuations; dashed line is soft lag simple reflector with transfer function; Continuous line is the sum of components. Credit: Zoghbi et al. (2011).

Miller et al. (2010) alternatively proposed that the soft lags were created by a partially opaque reverberating/reflecting region with a lower size limit of 1000 light-seconds from the black hole corresponding to 100 R_g for a black hole mass of $M \sim 2 \times 10^6\, M_\odot$. Although this region generates both soft and hard lags in Miller's model, similar to Zoghbi et al. (2010), Miller et al. (2010)'s model also requires two transfer functions in order to create the soft and hard lags (e.g., Zoghbi et al. 2011). As also discussed in Section 1.4.2, additional research has been presented that casts doubt that either of these models are presenting the correct physics for the observed lag behavior.

Hence, an important distinction between my model and the other models is that they require different mechanisms to explain the production of the hard time lags at low Fourier frequencies and the soft time lags at large Fourier frequencies. Conversely, in my model, both the hard and soft lags are produced as a natural consequence of thermal and bulk Comptonization occurring in the given physical model parameters.

6.2 X-ray Time Lags and PSDs

I have applied my new model to the interpretation of the X-ray time lags found in observations of 1H0707-495, as reported by Fabian et al. (2009), Zoghbi et al. (2010), and others. My physical time-dependent model has been able to successfully replicate the soft time lags based on a rigorous theoretical framework describing the reprocessing of an instantaneous flash of iron L-line photons. The value for the injection energy adopted here, $\epsilon_0 = 0.89\,\mathrm{keV}$, is close to the peak value for the energy of the broad iron L-line reported by Fabian et al. (2009), and hence the injection of the photons may be due to fluorescence of the iron line.

The theoretical results for the time lags plotted in Figure 3.6 provide good qualitative agreement with the observed time lag data for 1H0707-495, demonstrating that the observed soft lags are produced via thermal and bulk Comptonization occurring within the quasi-spherical region of the accretion flow. Hence, in my model, the hard and soft time lags are both produced in a single region, via the action of a unified physical mechanism. This provides a much simpler and straightforward alternative to other models which rely on unusual geometrical configurations, or multiple thermal zones with different properties, in order to reproduce the observed time lags. For instance, Zoghbi et al. (2010) and Miller et al. (2010) invoke different physical mechanisms to explain the production of the hard time lags at small Fourier frequencies and the soft time lags at large Fourier frequencies. Conversely, in my model, both the hard and soft lags are produced as a natural consequence of the underlying physics that occur due to thermal and bulk Comptonization in the quasi-spherical inner region of the accretion flow. As noted in Chapter 3 (see Figure 3.7), further supporting my model is that the PSD plots appear to show good agreement with the observed PSD, in contrast to the PSD study conducted to validate the reverberation theory, which did not agree with their expected theory (Emmanoulopoulos et al. 2016).

6.3 Universality of Time-Lag Mass Scaling

The universality of the mass scaling law discovered by De Marco et al. (2013) suggests that the critical frequency varies inversely with the black hole mass (see Figure 6.2).

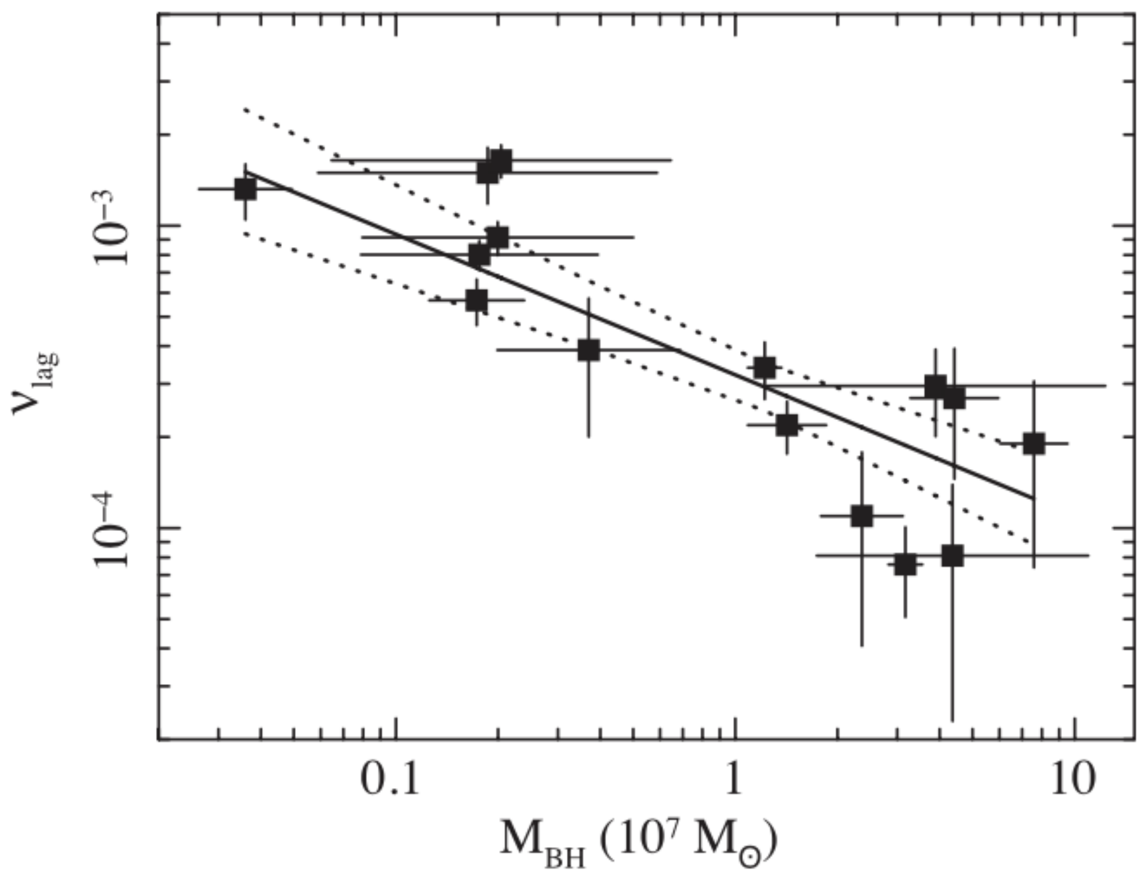

Figure 6.2: Negative lag frequency vs. $M_{\rm BH}$ for 15 AGN that display soft lags. The lag frequencies and amplitudes are redshift-corrected. The best-fitting linear models and the combined 1σ error on the slope and normalization are overplotted as continuous and dotted lines. Credit: De Marco et al. (2013).

Note that this behavior is a natural consequence of the bulk and thermal Comptonization model explored here, since, according to Equation (2.33),

$$\omega_c = \tilde{\omega}_c \left(\frac{\hat{\upsilon}^{1/2}}{\hat{\kappa}^{3/2}} \frac{R_g}{c} \right)^{-1} \quad , \tag{6.1}$$

where $\omega_c = 2\pi\nu_c$ denotes the dimensional critical frequency and $\tilde{\omega}_c = 5 \times 10^{-4}$ is the dimensionless critical frequency, which is a constant in my model. Hence Equation (6.1) implies that the critical frequency ω_c is inversely proportional to the mass of the black hole, in agreement with the results of De Marco et al. (2013), as depicted in Figure 6.2. This suggests that thermal and bulk Comptonization may be operative in all AGN displaying soft time lags. And if this is true, then it implies that my model should be applicable to many, if not all of these sources.

6.4 Discussion of GR Modifications and Causality

I now note two important technical points. First, although general relativity has not been fully incorporated, I expect that the same fundamental results would be obtained in an equivalent, fully relativistic model, because the fundamental physical process leading to the production of the time lags is electron scattering in the spherical region of the accretion flow, which is rigorously treated in my model. Second, due to the inherent geometry of my model, the flash of iron L-line photons is produced simultaneously at all points on a spherical shell with radius r_0. Since, relativity precludes any coherence in the emission process occurring on time-scales shorter than the light-crossing time for the region, one would obtain the same result for the Fourier transform solution obtained here even if the iron L-line photons where emitted at random locations on the spherical surface. This is because the time window for the Fourier transform "sweeps up" many such emission episodes. Hence, provided they are distributed in a spherically symmetric way, the total Fourier transform would remain in agreement with that computed here, and there would be no causality violation.

6.5 Quiescent Spectrum

In attempting to replicate the quiescent spectrum with my model, evidence points to the fact that a composite, two-component accretion scenario exists where, although the corona potentially contributes to the excess monochromatic emission lines noted in the spectrum, a cooler accretion disk is responsible for the vast majority of the broadband thermal contributions. The lack of the ability to fit the broadband thermal spectrum combined with evidence from the bremsstrahlung theoretical spectrum implies that the steady-state thermal emission, comprising the bulk of the X-ray signal, is produced in a surrounding, geometrically thin but optically thick, much cooler and radially larger, accretion disk. A cooler accretion disk corresponds with Fabian and others predicted physical configuration of a cooler accretion disk. As shown in Chapter 5, my optically thin, hot corona does not have a great deal of impact on any quiescent spectrum that might pass through it as demonstrated by the small Compton y-parameter. However, the flash of iron L-line photons within the corona that is responsible for the time lags, also appears to add to the spectral excess found in the composite spectrum. As shown in Chapter 5, the monochromatic injection source at an energy equaling the injection energy for the time lags, replicates the XSPEC Laor emission line that Pawar et al. (2016) and others use to model the composite spectrum. This further implies that the material accreting onto the black hole has two distinct aspects to it. The first material accretes spherically with low angular momentum, perhaps representing gas accreting from a spherical halo component in the galaxy. The second material has angular momentum, and forms the standard, cooler, canonical thin disk.

6.6 Future Work

There are key opportunities to continue research and expand on the work accomplished in this dissertation. First, a key next step is to apply this model to other black hole sources that generate soft lags such as shown in Figure 1.18 and Figure 3.8 panel a), but with expected different physical conditions. The generation of soft lags should be due to the same underlying physical processes and therefore my model should still be able to account for them by modifying my input parameters. A second and important next step is to attempt to achieve a fully holistic model. In order to do this, I propose to create a model that incorporates the aforementioned two-segment model. This more advanced model will include a cooler, optically thick, yet geometrically thick, radially extended, accretion disk in conjunction with a hot, optically thin, yet geometrically thick corona. This model will be able to investigate extending the accretion disk under the corona and employ it as the photon source for the Comptonizing corona above it. With this model I should be able to successfully generate both the spectral fits and the time lags.

Appendix A: Alternate Spatial Boundary Conditions

As stated previously, Colpi's (1988) investigation of an earlier version similar to this model assumed different spatial boundary conditions which included an adiabatic inner boundary at the origin and a diffusive boundary at infinity. Based on her work, for the time-dependent solutions, these alternate boundary conditions were also employed and studied in order to determine their validity in attaining models that might fit the observational data. The derivations and results for both the quiescent and time-dependent cases are presented below.

A.1 Time-Dependent Alternate Boundaries

Following Colpi's work, the inner and outer boundaries of the spherical coronal region are located at $r = 0$ and at $r = \infty$, respectively, and the corresponding values of the dimensionless location parameter y are,

$$y_{\rm in} = \infty, \quad y_{\rm out} = 0 \ . \tag{A.1}$$

The adiabatic and diffusive boundary conditions at the inner and outer boundaries can be written as

$$2yf'_{\rm G} = \lambda f_{\rm G} \ , \quad f_{\rm G}(y_{\rm in}) = 1, \qquad y = y_{\rm in} \ , \tag{A.2}$$

$$2yf'_{\rm G} = 5f_{\rm G} \ , \quad f_{\rm G}(y_{\rm out}) = 1, \qquad y = y_{\rm out} \ , \tag{A.3}$$

where primes denote differentiation with respect to y. Fourier transformation demonstrates that the spatial boundary conditions satisfied by the Green's function Fourier transform, $F_{\rm G}$, are given by,

$$2yF_{\mathrm{G}}' = \lambda F_{\mathrm{G}} \ , \quad y = y_{\mathrm{in}} \ , \quad \text{(inner boundary)} \ ,$$
$$2yF_{\mathrm{G}}' = 5F_{\mathrm{G}} \ , \quad y = y_{\mathrm{out}} \ , \quad \text{(outer boundary)} \ . \tag{A.4}$$

By combining Equations (2.35) and (A.4), it is found that the spatial separation function $G(y)$ satisfies the free-streaming boundary conditions

$$2yG' = \lambda G \ , \qquad y = y_{\mathrm{in}} \ , \tag{A.5}$$

$$2yG' = 5G \ , \qquad y = y_{\mathrm{out}} \ . \tag{A.6}$$

Similar to the main text, the eigenfunctions, $G_n(y)$, represent the discrete set of solutions to Equation (2.37) that simultaneously satisfy both the inner and outer boundary conditions given by Equations (A.5) and (A.6), respectively. The corresponding eigenvalues for the separation constant λ are denoted by λ_n.

The global solutions for the spatial eigenfunctions $G_n(y)$ are obtained using the same three-step process as discussed in the Chapter 2. For general, arbitrary values of the separation constant, λ, the inner and outer solutions are linearly independent functions. However, for certain special values of λ, the Wronskian of the inner and outer solutions vanishes, i.e.,

$$\mathfrak{W}(y_*) = 0 \ , \tag{A.7}$$

where

$$\mathfrak{W}(y_*) \equiv G_{\mathrm{in}}(y_*)\, G_{\mathrm{out}}'(y_*) - G_{\mathrm{out}}(y_*)\, G_{\mathrm{in}}'(y_*) \ , \tag{A.8}$$

and y_* is located anywhere in the computational domain, so that $y_{\mathrm{in}} \le y_* \le y_{\mathrm{out}}$. The eigenvalues λ_n are the roots of Equation (2.47). Note that the Fourier frequency, $\tilde{\omega}$, appears in Equation (2.37), and therefore it follows that a unique set of eigenvalues λ_n is obtained for each value of $\tilde{\omega}$.

Utilizing these solutions, one can solve for the eigenvalues as discussed in the main text and attempt to model the observed time lags. Additionally, one can also attempt to model the lags with a combination of the different boundary conditions. As can be seen by Table (A.1), the inner boundary condition produced similar results for both the inner adiabatic condition at the origin and the free-streaming inner boundary at r_{ISCO}. However, no lag fits were achievable using the infinite diffusive flux boundary.

Inner Boundary	Outer Boundary	Model Fit
Free-Streaming ($r = R_{\mathrm{ISCO}}$)	Free-Streaming ($r = 120R\_g$)	Yes
Adiabatic ($r = 0$)	Free-Streaming ($r = 120R\_g$)	Yes
Free-Streaming ($r = R_{\mathrm{ISCO}}$)	Diffusive ($r = \infty$)	No
Adiabatic ($r = 0$)	Diffusive ($r = \infty$)	No

Table A.1: Table of Attempted Boundary Condition Model Time Lag Fits to Observational Data.

A.2 Quiescent Alternate Boundaries

The quiescent alternate boundary conditions follow a similar derivation to the principal ones presented in the main text with the notable exception that I can utilize the fact that the function must be well behaved at the boundaries to simplify the solution.. The spatial equation is of the form of Kummer's equation and its complete solution is given by,

$$g(y) = AM\left(\frac{-\lambda}{2}, \frac{-3}{2}, y\right) + BU\left(\frac{-\lambda}{2}, \frac{-3}{2}, y\right) \tag{A.9}$$

Since the function must be well-behaved and go to zero at the boundaries, in the inner region, as $y \to \infty$, the M function blows up and so must not be part of the solution.

Likewise, in the outer region, as $y \to 0$, the U function blows up and so must not be part of the solution. Hence, the solutions in each of the regions is

$$g(y) = BU\Big(\frac{-\lambda}{2}, \frac{-3}{2}, y\Big), \qquad y_0 < y < y_{\text{in}} \ , \tag{A.10}$$

$$g(y) = AM\Big(\frac{-\lambda}{2}, \frac{-3}{2}, y\Big), \qquad y_0 < y < y_{\text{out}} \ . \tag{A.11}$$

For the diffusive-adiabatic case, the spatial separation function g satisfies the boundary conditions

$$2yg' = \lambda g \ , \quad g(y_{\text{in}}) = 1, \qquad y = y_{\text{in}} \ , \tag{A.12}$$

$$2yg' = 5g \ , \quad g(y_{\text{out}}) = 1, \qquad y = y_{\text{out}} \ . \tag{A.13}$$

Now, combining equations (A.10) and (A.12), for the inner region I have,

$$g(y_{\text{in}}) = 1 = B\ U\Big(\frac{-\lambda}{2}, \frac{-3}{2}, y\Big) \quad \to \quad B = \Big(U\Big(\frac{-\lambda}{2}, \frac{-3}{2}, y\Big)\Big)^{-1} \ . \tag{A.14}$$

Similarly, combining equations (A.11) and (A.13), for the outer region I have,

$$g(y_{\text{out}}) = 1 = A\ M\Big(\frac{-\lambda}{2}, \frac{-3}{2}, y\Big) \quad \to \quad A = \Big(M\Big(\frac{-\lambda}{2}, \frac{-3}{2}, y\Big)\Big)^{-1} \ . \tag{A.15}$$

Hence, the complete explicit spatial solutions in each of the regions for the adiabatic-diffusive case is

$$g(y) = \Big(U\Big(\frac{-\lambda}{2}, \frac{-3}{2}, y\Big)\Big)^{-1} U\Big(\frac{-\lambda}{2}, \frac{-3}{2}, y\Big), \qquad y_0 < y < y_{\text{in}} \ , \tag{A.16}$$

$$g(y) = \left(M\left(\frac{-\lambda}{2}, \frac{-3}{2}, y\right)\right)^{-1} M\left(\frac{-\lambda}{2}, \frac{-3}{2}, y\right). \qquad y_0 < y < y_{\text{out}} \ . \tag{A.17}$$

These solutions must create a smooth, continuous solution at y_0 and so the Wronskian must vanish at y_0 for these two regional solutions. Hence, the Wronskian of these must equal zero at y_0 and is given by (See Abramowitz and Stegun (1965)),

$$\mathfrak{W}(y_0) = -\Gamma(-3/2)y^{3/2}e^y/\Gamma(-\lambda/2) \ . \tag{A.18}$$

Utilizing these solutions to the spatial equation and the boundary conditions, one can solve for the eigenvalues using the same method as employed for the primary free-free boundary conditions in the main text. The eigenvalues for the quiescent solution are the same as given by Colpi (1988) and are the same as the adiabatic-diffusive boundary time-dependent case for $\tilde{\omega} = 0$.

References

Abramowicz, M. A. 2005, in Growing Black Holes: Accretion in a Cosmological Context, eds. A. Merloni, S. Nayakshin, & R. A. Sunyaev (Berlin: Springer), 257

Abramowicz, M. A., & Fragile, P. C. 2013, LRR, 16, 1

Abramowicz, M. A., Jaroszyński, M., Kato, S., et al. 2010, A&A, 521, A15

Abramowitz, M. & Stegun, I. A. 1964, Handbook fo Mathematical Functions (New York: Dover)

Alston, W., Fabian, A., Markevičiūtė, J., et al. 2016, AN, 337, 417

Arévalo, P., & Uttley, P. 2006, MNRAS, 367, 801

Arévalo, P., McHardy, I. M., & Summons, D. P. 2008, MNRAS, 388, 211

Arévalo, P., Uttley, P., & McHardy, I. 2006, X-ray variability of accreting black hole systems: propagating-fluctuation scenario. Proceedings of IAU Symposium, eds. V. Karas, & G. Matt (Prague, Czech Republic: IAU), 319

Balbus, S. A. 2005, ASPC 330, Numerical Simulations of the MRI in Real Disks. Astron. Soc. Pac., eds. J. M. Hameury, & J. P. Lasota (San Francisco, CA: ASP), 185

Becker, P. A. 1992, ApJ, 397, 88

Becker, P. A. 2003, MNRAS, 343, 215

Becker, P. A., Das, S., & Le, T. 2011, ApJ, 743, 47

Becker, P. A., & Wolff, M. T. 2007, ApJ, 654, 435

Boller, Th., Fabian, A. C., Sunyaev, R., et al. 2002, MNRAS, 329, L1

Böttcher, M., & Liang, E. P. 1999, ApJ, 511, L37

Cackett, E. M., Fabian, A. C., Zoghbi, A., et al. 2013, ApJ, 764, L9

Chakrabarti, S. K. 1989, PASJ, 41, 1145

Chattopadhyay, I., & Kumar, R. 2016, 459, 3792

Churazov, E., Gilfanov, M., & Revnivtsev, M. 2001, MNRAS, 321, 759

Colpi, M. 1988, ApJ, 326, 223

Crary, D.J., Finger, M. H., Kouveliotou, F., et al. 1998, ApJ, 493, L71

Das, S., Becker, P. A., & Le, T. 2009, ApJ, 702, 649

Dauser, T., Svoboda, J., Schartel, N., et al. 2012, MNRAS, 422, 1914

Davis, S. W., Done, C., Blaes, O. M. 2006, ApJ, 647, 525

De Marco, B., Ponti, G., Cappi, M., et al. 2013, MNRAS, 431, 2441

De Marco, B., Ponti, G., Muñoz-Darias, T., & Nandra, K. 2015, ApJ, 814, 50

Done, C., Gierliński, M., & Kubota, A. 2007, A&AR, 15, 1

Done, C., & Jin, C. 2016, MNRAS, 460, 1716

Emmanoulopoulos, D., McHardy, I. M., & Papadakis, I. E. 2011, MNRAS, 416, L94

Emmanoulopoulos, D., Papadakis, I. E., Epitropakis, A., et al. 2016, MNRAS,461,1642

Esin, A. A., McClintock, J. E., & Narayan, R. 1997, ApJ, 489, 865

Fabian, A. C., Rees, M. J., Stella, L., & White, N. E. 1989, MNRAS, 238, 729

Fabian, A. C., Zoghbi, A., Ross, R. R., et al. 2009, Nature, 459, 540

Fabian, A. C., Zoghbi, A., Wilkins, D., et al. 2012, MNRAS, 419, 116

Gardner, E., & Done, C. 2014, MNRAS, 442, 2456

Ghisellini, G. 2013, Radiative Processes in High Energy Astrophysics (Switzerland: Springer International Publishing)

Gutiérrez, E. M., Vieyro, F. L., & Romero, G. E. 2021, A&A, 649, A87

Iwasawa, K., Tanaka, Y., & Gallo, L. C. 2010, A&A, 514, A58

Jones, D. Heath, Read, Mike A., Saunders, Will, et al. 2009, MNRAS, 399, 683

Kara, E., Fabian, A. C., Cackett, E. M., et al. 2013, MNRAS, 428, 2795

Kara, E., García, J. A., Lohfink, A., et al. 2017, MNRAS, 468, 3489

Kosec, P., Buisson, D. J. K., Parker, M. L., et al. 2018, MNRAS, 481, 947

Kotov, O., Churazov, E., & Gilfanov, M. 2001, MNRAS, 327, 799

Kroon, J. J., & Becker, P. A. 2014, ApJ, 785, L34

Kroon, J. J., & Becker, P. A. 2016, ApJ, 821, 77

Leighly, K. M. 2004, ApJ, 611, 125

Lewis, T. R., Becker, P. A., & Finke, J. D. 2016, ApJ, 824, 108

Lyubarskii, Y. E. 1997, MNRAS, 292, 679

Mallick, L., Wilkins, D. R., Alston, W. N., et al. 2021, MNRAS, 503, 3775

Malzac, J., & Jourdain, E. 2000, A&A, 359, 843

Maraschi, L., & Molendi, S. 1990, ApJ, 353, 452

McClintock, J. E., & Remillard, R. A. 2006, in Compact Stellar X-ray Sources, eds. W. H. G. Lewin & M. van der Klis (New York: Cambridge University Press), 157

McHardy, I. M., Koerding, E., Knigge, C., et al. 2006, Nature, 444, 730

Merloni, A., Malzac, J., Fabian, A. C., & Ross, R. R. 2006, MNRAS, 370, 1699

Miller, L., Turner, T. J., Reeves, J. N., & Braito, V. 2010, MNRAS, 408, 1928

Misra, R. 2000, ApJ, 529, L95

Moscibrodzka, M., Proga, D., Czerny, B., & Siemiginowska, A. 2007, A&A, 474, 1

Narayan, R., Mahadevan, R., & Quataert, E. 1999, in Theory of Black Hole Accretion Discs, eds. M. A. Abramowicz, G. Björnsson, & J. E. Pringle (Cambridge, UK: Cambridge University Press), 148

Narayan, R., & McClintock, J. E. 2008, NewAR, 51, 733

Nowak, M. A., Vaughan, B. A., Wilms, J., Dove, J. B., & Begelman, M. C. 1999, ApJ, 510, 874

Paczyńsky, B., & Wiita, P. J. 1980, A&A, 88, 23

Papadakis I., Pecháček, T., Dovčiak, M., et al. 2016, A&A, 588, A13

Pawar P. K., Dewangan G. C., Papadakis I. E., Patil M. K., & Pal M., Kembhavi, A. K. 2017, MNRAS, 472, 2823

Pawar, P. K., Dewangan, G. D., Patil, M. K., Misra, R., & Jogadand, S. K. 2016, RAA, 16, Payne, D. G., & Blandford, R. D. 1981, MNRAS, 196, 781

Pica, A. J., & Smith, A. G. 1983, ApJ, 272, 11

Poutanen, J. 1999, in Theory of Black Hole Accretion Discs, eds. M. A. Abramowicz, G. Björnsson, & J. E. Pringle (Cambridge, UK: Cambridge University Press), 100

Proga, D., & Begelman, M. C. 2003, ApJ, 592, 767

Remillard, R. A., & McClintock, J. E. 2006, ARA&A, 44, 49

Rybicki, G. B., & Lightman, A. P. 1979, Radiative Processes in Astrophysics (Federal Republic of Germany: John Wiley & Sons, Inc.)

Sani, E., Lutz, D., Risaliti, G., et al. 2010, MNRAS, 403, 1246

Shakura, N. I., & Sunyaev, R. A. 1973, A&A, 24, 337

Shapiro, S. L., & Teukolsky, S. A. 1983, Black Holes, White Dwarfs, and Neutron Stars (Federal Republic of Germany: John Wiley & Sons, Inc.)

Shu, F. H. 2009, The Physics of Astrophysics, Vol. II (United States: University Science books)

Smith, K. L., Mushotzky, R. F., Boyd, P. T., et al. 2018, ApJ, 857, 141

Sobolewska, M. A., Siemiginowska, A., & Gierliński, M. 2011, MNRAS, 413, 2259

Straub, O., Vincent, F. H., Abramowicz, M. A., Gourgoulhon, E., & Paumard, T. 2012, A&A, 543, A83

Tanaka, Y., Boller, T., Gallo, L., Keil, R. 2004, PASJ, 56, L9

Titarchuk, L., Mastichiadis, A., & Kylafis, N. D. 1997, ApJ, 487, 834

van der Klis, M. 2006, in Compact Stellar X-ray Sources, eds. W. H. G. Lewin & M. van der Klis (New York: Cambridge University Press), 39

van der Klis, M., Hasinger, G., Stella, L., et al. 1987, ApJL, 319, L13

Voges, W., Aschenbach, B., Boller, Th., et al. 1999, A&A, 349, 389

Wang, J.-M., & Netzer, H. 2003, A&A, 398, 927

Wilkins, D. R., & Fabian, A. C. 2011, MNRAS, 414, 1269

Wilkins, D. R., Kara, E., Fabian, A. C., & Gallo, L. C. 2014, MNRAS, 443, 2746

Yuan, F., & Narayan, R. 2014, ARA&A, 52, 529

Zhou, X., & Wang, J. 2005, ApJ, 618, L83

Zoghbi, A., Fabian, A. C., Uttley, P., et al. 2010, MNRAS, 401, 2419

Zoghbi, A., Uttley, P., & Fabian, A. C. 2011, MNRAS, 412, 59

Curriculum Vitae

David C. Baughman received his Bachelor of Science degrees in Mathematics and Physics from the United States Naval Academy, Annapolis, MD, in 2000. He received his Master of Arts degree in National Security and Strategic Studies from the Naval War College in 2007. He received his Master of Science degrees in Physics and Space Systems Operations from the Naval Postgraduate School in 2011.